

Exciton-Induced Degradation of Interfaces in Organic Light-Emitting Devices

by

Qi Wang

A thesis
presented to the University of Waterloo
in fulfillment of the
thesis requirement for the degree of
Doctor of Philosophy
in
Electrical and Computer Engineering

Waterloo, Ontario, Canada, 2015

©Qi Wang 2015

AUTHOR'S DECLARATION

I hereby declare that I am the sole author of this thesis. This is a true copy of the thesis, including any required final revisions, as accepted by my examiners.

I understand that my thesis may be made electronically available to the public.

Abstract

A new revolution in electronics/optoelectronics has become possible in the past two decades due to the emergence of organic semiconductors. Among all the applications based on organic semiconductors, organic light-emitting devices (OLEDs) have so far been the most promising technology. OLEDs are rapidly gaining momentum as future candidates for displays and solid-state lighting, due to their unique advantages such as thin-film architecture, low manufacturing energy and temperature requirements, mechanical flexibility and the potential for large-scale fabrication. Despite the significant progress in realizing high-efficiency OLEDs, one of the biggest technical barriers for their wider commercial presence remains the rapid device luminance degradation, especially for the blue-emitting ones. Understanding the underlying degradation mechanism is therefore a prerequisite for the realization of devices with prolonged stability.

In this thesis, exciton-induced degradation of interfaces in OLEDs, including organic/electrode and organic/organic interfaces, is studied. The investigations uncover that excitons can affect and degrade device interfaces much more severely than they can affect bulk material. The results also reveal that excitons degrade both types of interfaces, resulting in a deterioration in charge conduction across them. In case of organic/electrode interfaces, the degradation is caused by the mere presence of excitons in their vicinity. Such degradation is found to be photo-chemical in nature, and is associated with a reduction in chemical bonds between metal atoms and organic molecules. Such interfacial degradation can occur during device normal operation by means of direct electron-hole (e-h) recombination near the interfaces, diffusion of excitons to the interfaces, or re-absorption of emitted photons. In case of organic/organic interfaces, on the other hand, the degradation arises from aggregation of both host and guest materials in the vicinity of the e-h recombination zone. Such aggregation process is induced by the co-existence of excitons and positive polarons on host or guest molecules. The extent of aggregation appears to correlate with the materials bandgap rather than with their glass-transition temperatures. The findings uncover a previously unknown degradation mechanism that appears to be responsible for the generally much lower stability of blue devices relative to their green and red counterparts, especially in case of phosphorescent emitters, and provide the first explanation for the generally lower stability of phosphorescent OLEDs relative to their fluorescent counterparts. The discovered phenomenon is also expected to be playing a role in the degradation of other organic optoelectronic devices such as organic photo-detectors and organic solar cells.

Acknowledgements

I would like to express my deepest thanks to my supervisor, Prof. Hany Aziz, for his outstanding doctoral supervision. I am grateful that Prof. Aziz had introduced me into the world of materials science and engineering, full of challenges and excitement, and inspired me to actively explore it. Over the past years, I have not only enlarged my scientific knowledge, but also obtained the ability to work independently and think critically. Without his continuous support, cultivation and encouragement on this journey, I would not be the person I am today.

I would also like to thank Dr. Michael Helander for taking the time to review chapters 1 and 2 of the thesis and for his valuable comments/suggestions.

Table of Contents

AUTHOR'S DECLARATION	ii
Abstract	iii
Acknowledgements	iv
Table of Contents	v
List of Figures	vii
List of Tables	xv
Chapter 1 Introduction.....	1
1.1 A Brief Introduction to OLEDs.....	1
1.2 Background Theory	3
1.2.1 Organic Semiconductors	3
1.2.2 Charge Injection and Transport.....	4
1.2.3 Exciton Formation and Dissipation	6
1.3 OLEDs Stability	10
1.4 Thesis Outline.....	11
Chapter 2 Degradation Mechanisms of OLEDs.....	12
2.1 Ambient Degradation	12
2.2 Intrinsic Degradation.....	13
2.2.1 Unstable Cationic Molecules Model	14
2.2.2 Space-Charge Accumulation Model.....	14
2.2.3 Chemical Degradation by Excitons Model.....	15
2.2.4 Exciton-Polaron Annihilation Model	16
2.3 Limitation with Existing Knowledge	16
2.4 Motivations and Objectives.....	18
Chapter 3 Experimental Methods.....	20
3.1 Materials.....	20
3.2 Test-Device Configurations.....	24
3.2.1 OLEDs.....	24
3.2.2 Single-Carrier Devices	25
3.2.3 Converting Single-Carrier Devices into Bipolar Devices	27
3.3 Device Fabrication and Characterization	28
3.4 EL Stability Measurement.....	28

3.5 Photo-Stability Measurement.....	29
3.6 Delayed EL Measurement.....	29
3.7 X-ray Photoelectron Spectroscopy.....	30
3.8 Interfacial Adhesion Test.....	30
Chapter 4 Exciton-Induced Degradation of Organic/Metal Interfaces	31
4.1 Investigation of Exciton-Induced Degradation of Organic/Metal Interfaces.....	31
4.2 Investigating the Correlation between Interfacial Degradation vs. Energy-Level Offset at Organic/Metal Interfaces.....	43
4.3 Identifying the Role of Interfacial Layers in Improving Device Stability	51
4.4 Summary	54
Chapter 5 Exciton-Induced Degradation of ITO/Organic Interfaces	56
5.1 Investigation of Exciton-Induced Degradation of ITO/Organic Interfaces	56
5.2 Summary	65
Chapter 6 Degradation of Organic/Organic Interfaces due to Exciton-Polaron Interactions.....	66
6.1 Degradation of Organic/organic Interfaces by Exciton-Polaron Interactions	66
6.2 Degradation of Host Materials	77
6.2.1 Exciton-Polaron-Induced Aggregation (EPIA).....	77
6.2.2 Different Influence of Singlet and Triplet Excitons in EPIA.....	93
6.3 Degradation of Guest Materials	104
6.4 Summary	117
Chapter 7 Summary and Future Work	118
7.1 Summary	118
7.2 Future Work.....	119
Appendix A List of Publications Derived from the Thesis Research	121
Bibliography	122

List of Figures

Figure 1.1: Different approaches to generate light.	2
Figure 1.2: Schematic energy diagram of an OLED and its working principle.	3
Figure 1.3: Energy level alignment at a semiconductor/metal interface.	4
Figure 1.4: Two models for charge carrier injection from a metal contact to an organic layer.	5
Figure 1.5: Jablonski diagram showing radiative and non-radiative dissipation pathways available to molecules.	8
Figure 1.6: Dissipation pathways of single and triplet excited states in fluorescent and phosphorescent OLEDs.	10
Figure 2.1: Formation of dark-spots in a corner of an OLED.	12
Figure 2.2: A schematic diagram showing OLED encapsulation.	13
Figure 2.3: EL (normalized to initial intensity) and driving voltage versus time, collected from an OLED driven by a constant current.	13
Figure 3.1: General structures of OLEDs used in this study.	25
Figure 3.2: Schematic structures of hole-only and electron-only single-carrier devices.	26
Figure 3.3: Energy diagrams of hole-only and electron-only devices.	26
Figure 3.4: Schematic structures of modified hole-only and electron-only devices.	27
Figure 3.5: Energy diagrams of modified hole-only and electron-only devices.	27
Figure 3.6: Process of converting a hole-only device into an OLED.	28
Figure 3.7: Schematic sequence for the acquisition of delayed EL.	30
Figure 4.1: (a) Normalized I_{ph} (at a reverse bias of 7 V) and normalized PL versus irradiation time in samples of structure ITO/NPB(20nm)/NPB:BAIq(50nm)/BAIq(30)/Al(100nm). A 365 nm illumination at a power density of $\sim 0.5 \text{ mW cm}^{-2}$ is used for irradiation. The control sample kept in dark is also shown. (b) Changes in I_{ph} at a reverse bias of 7 V vs. I_{dark} at a forward bias of 2.5 V, 3.5 V and 5 V, respectively, during irradiation.	32
Figure 4.2: Normalized I_{dark} versus irradiation time in samples of structure (a) ITO/Alq ₃ (60nm)/Al(100nm), (b) ITO/Alq ₃ (60nm)/Ag(100nm) and (c) ITO/Alq ₃ (60nm)/Mg(50nm)/Ag(50nm). Monochromatic illumination of various wavelengths at a power density of $\sim 0.35 \text{ mW cm}^{-2}$ is used for irradiation.	34
Figure 4.3: Absorption spectrum of neat Alq ₃ film and the % loss in I_{dark} in samples of structure (a) ITO/Alq ₃ (60nm)/Al(100nm), ITO/Alq ₃ (60nm)/Ag(100nm) and (b)	

ITO/Alq ₃ (60nm)/Mg(50nm)/Ag(50nm) after irradiation for a period of 5 minutes at different wavelengths.....	35
Figure 4.4: Absorption spectra of neat (a) TPBi film, (b) BAQ film and the % loss in I _{dark} after irradiation for a period of 5 minutes at different wavelengths.....	36
Figure 4.5: (a) Ag 3d electron binding energy spectra from samples of structure ITO/Ag(10nm)/Alq ₃ (10nm). A 365 nm illumination at a power density of ~0.5 mW cm ⁻² is used for irradiation for a period of 10 hours. (b) Ag 3d electron binding energy spectra from an Ag film that has been exposed to air prior to the XPS test.....	38
Figure 4.6: (a) Al 2p electron binding energy spectra from samples of structure ITO/Al(10nm)/Alq ₃ (10nm). (b) Al 2p electron binding energy spectra from samples of structure ITO/Alq ₃ (10nm)/Al(5nm). A 365 nm illumination at a power density of ~0.5 mW cm ⁻² is used for irradiation for a period of 10 hours.....	39
Figure 4.7: (a) Schematic of a four-point flexure specimen for adhesion measurement. (b) A typical load versus displacement characteristics.....	41
Figure 4.8: Energy release rate of (a) Alq ₃ /Ag and (b) Alq ₃ /Al contacts before and after 365 nm irradiation at a power density of ~0.5 mW cm ⁻² for a period of 10 hours.....	42
Figure 4.9: (a) E-only device of structure ITO(120nm)/ETM(60nm)/Metal(100nm) under UV irradiation, where the ETM is TPBi, AlQ ₃ or BAQ, and the metal is Ag, Al or Mg. (b) Absorption spectra of TPBi, AlQ ₃ and BAQ.....	44
Figure 4.10: Changes in electron current (normalized to the initial current level at time zero) under a constant forward bias of TPBi based e-only devices containing different metal contacts versus time during which the devices are exposed to (a) 333 nm illumination at a power density of ~0.3 mW/cm ² and (b) 365 nm illumination at a power density of ~0.5 mW/cm ²	45
Figure 4.11: (a) Current loss (i.e. left y-axis) due to exposure to 333 nm and 365 nm irradiations for periods of 10 minutes and 30 minutes, respectively, in case of TPBi e-only devices with Ag, Al and Mg contacts and the work functions of the corresponding metals (i.e. right y-axis). (b) Current loss in TPBi e-only devices with Ag, Al, Mg and Li-acac/Al contacts and the work functions of Ag, Al, Mg and Li.....	46
Figure 4.12: (a) Current-voltage characteristics of TPBi based e-only devices with different metal contacts. (b) Current loss (i.e. left y-axis) due to exposure to 333 nm and 365 nm	

irradiations for periods of 10 minutes and 30 minutes, respectively, and $V_{\text{turn-on}}$ (i.e. right y-axis) of the TPBi based e-only devices.	47
Figure 4.13: Changes in electron current (normalized to the initial current level at time zero) under a constant forward bias of AlQ ₃ based e-only devices containing different metal contacts versus time during which the devices are exposed to (a) 365 nm illumination at a power density of ~ 0.5 mW/cm ² and (b) 405 nm illumination at a power density of ~ 0.5 mW/cm ² . (c) Current loss (i.e. left y-axis) due to exposure to 365 nm and 405 nm irradiations for a period of 40 minutes of the devices with Ag, Al and Mg contacts and the work functions of these metals (i.e. right y-axis).	49
Figure 4.14: Changes in electron current (normalized to the initial current level at time zero) under a constant forward bias of BAlq based e-only devices containing different metal contacts versus time during which the devices are exposed to (a) 365 nm illumination at a power density of ~ 0.5 mW/cm ² and (b) 405 nm illumination at a power density of ~ 0.5 mW/cm ² . (c) Current loss (i.e. left y-axis) due to exposure to 365 nm and 405 nm irradiations for a period of 40 minutes of the devices with Ag and Al contacts and the work functions of these metals (i.e. right y-axis).	49
Figure 4.15: Band diagrams for organic/metal interfaces with metals of work functions (a) lower and (b) higher than the Fermi energy level of the ETM.	51
Figure 4.16: (a) OLEDs with the general structure ITO(120nm)/NPB(70nm)/Alq ₃ (70nm)/Cathode. (b) Changes in EL and V_d at a current density of 50 mA/cm ² as a function of time from OLEDs with cathode of Mg:Ag, Cs ₂ CO ₃ /Mg:Ag and Cs ₂ CO ₃ /Al, respectively.	52
Figure 4.17: (a) Samples with the general structure ITO(120nm)/Alq ₃ (70nm)/Cathode. (b) Changes in V_d at a current density of 20 mA/cm ² as a function of time during which the samples are irradiated by a 546nm external illumination with the power density of 1.0 mW/cm ²	53
Figure 5.1: V_d at a current density of 10 mA/cm ² versus time during which the devices are subjected to exposing to irradiation at 365 nm, at 546 nm or kept in the dark. The structures of these devices are: (a) untreated ITO/NPB(70nm)/Alq ₃ (70nm)/Mg:Ag(100nm), (b) plasma treated ITO/NPB(70nm)/Alq ₃ (70nm)/Mg:Ag(100nm), and (c) untreated ITO/MoO ₃ (1nm)/NPB(70nm)/Alq ₃ (70nm)/Mg:Ag(100nm).	57

Figure 5.2: Normalized EL and V_d at current density of 20 mA cm^{-2} versus electrical aging time of OLEDs with the structures ITO/NPB(70nm)/Alq₃(70nm)/Mg:Ag(100nm), PT-ITO/NPB(70nm)/Alq₃(70nm)/Mg:Ag(100nm) and ITO/MoO₃(1nm)/NPB(70nm)/Alq₃(70nm)/Mg:Ag(100nm). Inset: V_d at current density of 10 mA cm^{-2} versus 546 nm irradiation time of OLEDs with the same structures..... 60

Figure 5.3: (a) In $3d$ electron binding energy spectra from ITO substrate and ITO/NPB(3nm). (b) O $1s$ electron binding energy spectra from the same samples. A 365 nm illumination at a power density of $\sim 0.5 \text{ mW cm}^{-2}$ is used for irradiation for a period of 10 hours. 62

Figure 5.4: (a) In $3d$ electron binding energy spectra from PT-ITO substrate and PT-ITO/NPB(3nm). (b) O $1s$ and (c) F $1s$ electron binding energy spectra from the same samples. A 365 nm illumination at a power density of $\sim 0.5 \text{ mW cm}^{-2}$ is used for irradiation for a period of 10 hours..... 63

Figure 5.5: (a) In $3d$ electron binding energy spectra from samples ITO/MoO₃(1nm) and UT-ITO/MoO₃(1nm)/NPB(3nm). (b) O $1s$ and (c) Mo $3d$ electron binding energy spectra from the same samples. A 365 nm illumination at a power density of $\sim 0.5 \text{ mW cm}^{-2}$ is used for irradiation for a period of 10 hours. 64

Figure 6.1: Change in V_d at 20 mA/cm^2 in devices (a) with and (b) without the TPBi layer, versus time, during which the devices are subjected to stress scenarios: $\langle I \text{ only} \rangle$, $\langle L_{365\text{nm}} \text{ only} \rangle$ and $\langle I + L_{365\text{nm}} \rangle$. The curve $\Sigma(\langle I \text{ only} \rangle, \langle L_{365\text{nm}} \text{ only} \rangle)$ represents the algebraic sum of the ΔV in $\langle I \text{ only} \rangle$ and $\langle L_{365\text{nm}} \text{ only} \rangle$ 67

Figure 6.2: Changes in V_d at 20 mA/cm^2 in devices (a) with and (b) without the AlQ₃ layer, versus time, during which the devices are subjected to stress scenarios: $\langle I \text{ only} \rangle$, $\langle L_{365\text{nm}} \text{ only} \rangle$, $\langle I + L_{365\text{nm}} \rangle$ and $\langle I + L_{405\text{nm}} \rangle$. The curve $\Sigma(\langle I \text{ only} \rangle, \langle L_{365\text{nm}} \text{ only} \rangle)$ represents the algebraic sum of the ΔV in $\langle I \text{ only} \rangle$ and $\langle L_{365\text{nm}} \text{ only} \rangle$ 70

Figure 6.3: Time domain CBP fluorescence lifetime of 30 nm neat CBP and DCJTb-doped CBP (4%) films, excited by a 379 nm pulsed laser. 72

Figure 6.4: Changes in V_d at 20 mA/cm^2 in devices where (a) the DCJTb layer is in the CBP and 5 nm away from the CBP/TPBi interface, (b) the DCJTb layer is in the CBP and 1 nm away from the CBP/TPBi interface, (c) the DCJTb layer is in the TPBi and 1 nm away from the CBP/TPBi interface and (d) no DCJTb layer is present, versus time, during which the devices are subjected to scenarios: $\langle I \text{ only} \rangle$, $\langle L_{365\text{nm}} \text{ only} \rangle$ and $\langle I + L_{365\text{nm}} \rangle$. The curve

$\Sigma(\langle I \text{ only} \rangle, \langle L_{365\text{nm}} \text{ only} \rangle)$ represents the algebraic sum of the ΔV in $\langle I \text{ only} \rangle$ and $\langle L_{365\text{nm}} \text{ only} \rangle$	74
Figure 6.5: Change in driving voltage at a current of density 20 mA/cm ² in (a) CBP/TPBi based and (b) NPB/AIQ ₃ based OLEDs versus time of continuous electrical driving.	76
Figure 6.6: (a) Structure of PhOLEDs and molecular structures of the materials used. (b) Changes in normalized EL and V_d of the devices with different Ir(ppy) ₃ concentrations versus time during which the devices are continuously driven by a current of density 20 mA cm ⁻² . (c) Normalized EL spectra of the devices. The inset of (c) shows a detailed view of the spectra in the short-wavelength region.	78
Figure 6.7: Luminescence decay in time (a) at 400 nm (i.e., from the relaxation of CBP singlet excitons) and (b) at 520 nm (i.e., from the relaxation of Ir(ppy) ₃ triplet excitons) collected from CBP:Ir(ppy) ₃ films with different Ir(ppy) ₃ concentrations.	80
Figure 6.8: (a) EL (with normalization), (b) EL (without normalization) and (c) PL (with normalization) spectra with continuous electrical driving at 20 mA cm ⁻² in a device of structure ITO/MoO ₃ (5nm)/CBP(30nm)/TPBi(20nm)/LiF(0.5nm)/Al(100nm). Two photographs depicting the emission colors and corresponding CIE coordinates of the device before and after electrical driving are included in (b).	81
Figure 6.9: Normalized EL spectra of a device of structure ITO/MoO ₃ (5nm)/CBP(20nm)/CBP:PtOEP(2%)(20nm)/TPBi(30nm)/LiF(0.5nm)/Al(100nm) before and after 10 hours of electrical driving at 20 mA cm ⁻² . The inset shows a detailed view of the spectra in the short-wavelength region.	82
Figure 6.10: (a) Normalized EL spectra of a device of structure ITO(120nm)/MoO ₃ (5nm)/CBP(40nm)/TPBi(30nm)/LiF(0.5nm)/Al(100nm) before and after annealing at 120 °C for 20 and 60 minutes in a N ₂ atmosphere. The inset shows the differences between the EL spectra after 20 minutes and 60 minutes of annealing relative to the initial one. (b) Normalized PL spectra under a 365 nm excitation of a CBP film before and after annealing at 120 °C for 20, 60 and 100 minutes in a N ₂ atmosphere. The inset shows the differences between the PL spectra after 60 minutes and 100 minutes of annealing relative to the initial one. (c) Absorption spectra of a CBP film before and after 100 min of annealing at 120 °C. (d) Normalized PL under a 312 nm excitation of a TPBi film before and after thermal annealing at 150 °C.....	84

Figure 6.11: (a) H-only devices of structure ITO/MoO₃(5nm)/CBP(30nm)/TPBi(10nm)/MoO₃(10nm)/Al(100nm). (b) Changes in V_d (ΔV) driven by a current of density 20 mA cm⁻² in the devices versus time, during which these devices are subjected to scenarios <I only>, <L only> and <I + L> and kept in the dark (i.e., <C>). Traces representing the algebraic sum of the ΔV values caused by the scenarios <I only> and <L only> (denoted by $\Sigma(\langle I \text{ only} \rangle, \langle L \text{ only} \rangle)$) is also included. 86

Figure 6.12: (a) Illustration of the cathode replacing process, in which h-only devices are converted to light-emitting devices. (b) Normalized EL spectra of the four light-emitting devices. The inset shows a detailed view of the spectra at ~ 500 nm. (c) Differences between the EL spectra of the devices subjected to the scenarios <I + L>, <I only> and <L only> relative to that of the control device. 88

Figure 6.13: Molecular structures of a range of wide-bandgap organic materials..... 90

Figure 6.14: EL spectra (without normalization) with continuous electrical driving at 20 mA cm⁻² in devices of general structure ITO/MoO₃(5nm)/X(30nm)/TPBi(30nm)/LiF(0.5nm)/Al(100nm), where X is CBP, Spiro-CBP, TAPC, mCP, TCTA, TBAND, NPB or Spiro-NPB. 91

Figure 6.15: Ratio of aggregate/monomer EL bands versus the materials (a) E_g and (b) T_g temperatures. 92

Figure 6.16: EL intensity (normalized to initial values) and ΔV versus time during which PhOLEDs containing Ir(piq)₃ and PtOEP as guests are driven by a constant current of density 20 mA/cm². 94

Figure 6.17: EL spectra of the devices containing (a) 5% Ir(piq)₃, (b) 1.5% Ir(piq)₃, (c) 5% PtOEP, (d) 1.5% PtOEP collected before (i.e. from the fresh devices) and after the electrical stress. The insets show amplified EL spectra in the shorter-wavelength region, showing emission from CBP monomers at ~ 400 nm, CBP aggregates at ~ 500 nm and a higher level of thermally populated PtOEP triplet states with the little spike at ~ 545 nm (in the PtOEP devices only). 96

Figure 6.18: A plot of device lifetime versus rate of host aggregation. 97

Figure 6.19: EL spectra (normalized to peak intensities) collected from the fresh devices containing (a) 5% Ir(piq)₃, (b) 1.5% Ir(piq)₃, (c) 5% PtOEP, (d) 1.5% PtOEP driven at current densities of 20, 2 and 0.2 mA/cm². The insets show amplified spectra in the short-wavelength region. 98

Figure 6.20: A plot of (a) Device lifetime and (b) V_d stability versus host to guest EL bands ratio.	99
Figure 6.21: Phosphorescence versus time at (a) 620 nm (i.e. from the relaxation of Ir(piq) ₃ triplet states) and (b) 650 nm (i.e. from the relaxation of PtOEP triplet states) collected from the fresh devices shown in figure 1 excited by a 379 nm laser pulse.	100
Figure 6.22: Delayed EL signals collected from the devices with (a) 5% Ir(piq) ₃ , (b) 1.5% Ir(piq) ₃ , (c) 5% PtOEP and (d) 1.5% PtOEP versus time elapsed from the end of the forward bias pulse. A 200 μ s reverse bias pulse (with a magnitude of 2, 5 or 8 V) is applied to the devices during the signal collection. The insets of (a) and (c) show delayed EL spectra of the devices, whereas the inset of (b) shows amplified delayed EL upon the removal of the reverse bias.	103
Figure 6.23: LT50 values at 20 mA cm ⁻² for various phosphorescent guest materials and their concentrations.	105
Figure 6.24: EL spectra (normalized to the peak intensities) of devices with (a) 5% FIrpic, (b) 10% Ir(ppy) ₂ acac and (c) 10% Ir(ppy) ₃ , collected before and after electrical driving at 20 mA cm ⁻² for certain periods of time. Insets: differences between the EL spectra collected after the electrical driving relative to the initial ones.	106
Figure 6.25: Normalized EL spectra collected from fresh devices containing (a) FIrpic, (b) Ir(ppy) ₂ acac and (c) Ir(ppy) ₃ , with concentrations of 1.5, 5 and 10%.	108
Figure 6.26: EL spectra collected from devices of the structure ITO/MoO ₃ (5 nm)/CBP(30 nm)/Ir(ppy) ₂ acac(x nm)/TPBi(30 nm)/LiF(0.5 nm)/Al(100 nm), where x is equal to (a) 2, (b) 1 and (c) 0.5, before and after 14 hours of electrical driving at 20 mA cm ⁻¹ . (d) Differences between the spectra after the stress relative to the initial ones.	109
Figure 6.27: EL stability of the devices (i.e. LT50 values) versus time for onset of detectable aggregation in the devices by electrical aging (i.e. defined as the time of electrical driving elapsed until the aggregate EL band intensity reaches 1% of the monomer EL band intensity).	110
Figure 6.28: Molecular structures of Ir-based compounds used as phosphorescent emitters.	111
Figure 6.29: (a) Illustration of replacing the top electrode with an electron-injecting cathode, in which h-only devices are converted into bipolar devices. (b) Normalized EL spectra of FIrpic collected from the four bipolar devices. The inset shows differences between the EL	

<p>spectra of the devices subjected to the scenarios <I + L>, <I only> and <L only> relative to that of the control one.</p> <p>Figure 6.30: (a) Illustration of replacing the top electrode with an electron-injecting cathode, in which h-only devices are converted into bipolar devices. (b) Normalized EL spectra of CBP collected from the four bipolar devices. The inset shows differences between the EL spectra of the devices subjected to the scenarios <I + L>, <I only> and <L only> relative to that of the control one.</p> <p>Figure 6.31: EL spectra (after normalization) with continuous electrical driving at 20 mA cm^{-2} collected from devices of the structure ITO/MoO₃(5 nm)/NPB(40 nm)/Alq₃:C545T(10 nm)/Alq₃(20 nm)/LiF(0.5 nm)/Al(100 nm), in which the fluorescent emitter C545T is doped into the Alq₃ host with the concentration of (a) 10%, (b) 5% and (c) 0%.</p>	<p>113</p> <p>114</p> <p>116</p>
---	----------------------------------

List of Tables

Table 1.1: Performance of phosphorescent OLEDs from Universal Display Corporation.	11
Table 3.1: Organic molecules used in this study.	24

Chapter 1

Introduction

A new revolution in electronics/optoelectronics has been made possible in the past two decades due to the emergence of a new class of semi-conducting materials, i.e. organic semiconductors.¹ Enormous progress in science and technology has been made by the research and development of various applications of these materials in electronic/optoelectronic devices, such as organic light emitting devices (OLEDs),² organic field effect transistors,³ organic solar cells (OSCs),⁴ organic photo-detectors (OPDs)⁵ and organic memory devices.⁶

Among all the applications based on organic semiconductors, OLEDs have so far been the most promising in terms of technical superiority and commercialization. OLEDs are rapidly gaining momentum as high performance displays in mobile phones, and as future candidates for large area television displays and solid-state lighting, due to their unique advantages. OLEDs can be made extremely thin due to their thin-film architecture, and can be simply manufactured using low-cost and sustainable carbon based materials.

1.1 A Brief Introduction to OLEDs

Light, or photons, can be generated from materials via a number of mechanisms, such as incandescence (i.e., emission of light from a hot body due to its temperature), bioluminescence (i.e. emission of light by a living organism), chemoluminescence (i.e. emission of light as the result of a chemical reaction), photoluminescence (i.e. a process in which a substance absorbs photons and re-emits photons) and electroluminescence (EL) (i.e. an optical/electrical phenomenon in which a material emits light in response to an electric current passing through it), as shown in **figure 1.1**. The emission of light from an OLED is essentially the process of EL in organic materials.



Figure 1.1: Different approaches to generate light.⁷

The first OLED was invented by Eastman Kodak in 1987, using a novel double-organic-layer structure with separate hole-transport and electron-transport materials.² This started the current era of OLED research and development. Nowadays an OLED consists of a series of organic thin films, including typically a hole-transport layer (HTL), an emissive layer (EML) and an electron-transport layer (ETL), sandwiched between two thin-film conductive electrodes (i.e. a transparent anode and an opaque cathode), as shown in **figure 1.2**. When electricity is applied to the OLED (i.e. the anode is positively biased relative to the cathode), charge carriers (holes and electrons) are injected from the electrodes into the organic layers. Under the influence of the electrical field, holes and electrons migrate through the highest occupied molecular orbital (HOMO) and the lowest unoccupied molecular orbital (LUMO) of the organic materials, respectively, until they recombine, forming excited states (i.e. excitons). Once formed, the excitons relax to a lower energy level (i.e. ground state) by emitting light (i.e. radiative relaxation) and/or releasing heat (i.e. non-radiative relaxation).

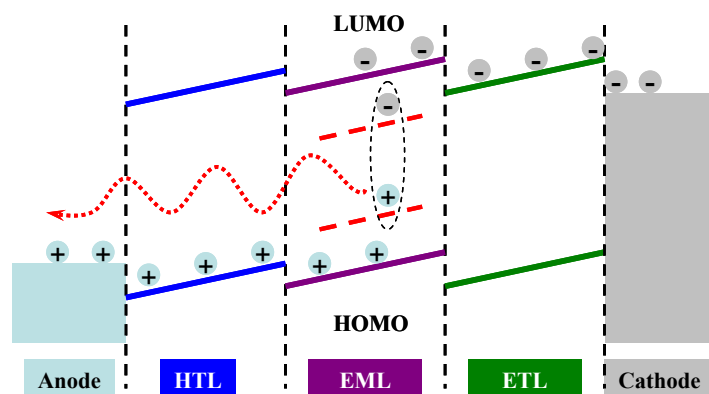


Figure 1.2: Schematic energy diagram of an OLED and its working principle.

The organic materials used in OLEDs can be either small molecules or polymers. Small-molecule devices are fabricated by thermal evaporation of organic molecules and metal electrode in high vacuum,² whereas polymer devices are fabricated by spin-coating of polymers (metal electrodes, however, still need to be deposited via thermal evaporation in high vacuum).⁸ Compared to polymer devices, small-molecule devices have so far achieved much better performance in efficiency and stability, and have been more easily commercialized. The OLEDs involved in this work are exclusively small-molecule based.

1.2 Background Theory

1.2.1 Organic Semiconductors

Organic semiconductors are organic materials that exhibit semiconductor properties, i.e., with an electrical conductivity between that of insulators and that of metals. Small organic molecules and polymers can be semi-conductive. Some representative small-molecule-based semiconductors include pentacene, rubrene and anthracene.

The nature of bonding in organic semiconductors is fundamentally different from their inorganic counterparts. In inorganic semiconductors (e.g. Si or Ge), the strong atomic bonding and the long-range order lead to strong delocalization of electronic wavefunctions and the formation of valence and conduction bands. Free electrons can be generated in the conduction band via thermal activation or photo-excitation, leaving behind holes in the valence band. Organic semiconductors, on the other hand, are bonded by van der Waals forces, implying a significantly weaker intermolecular bonding in comparison to covalently bonded inorganic semiconductors (e.g. Si or GaAs). The consequences are

evident in mechanical and thermodynamic properties such as reduced hardness and lower melting/boiling point. What is however more important is the much weaker delocalization of electronic wavefunctions among neighboring molecules. This has a direct impact on the charge-carrier transport characteristics and photo-physical properties of organic semiconductors, which will be introduced in details in the following sections.

1.2.2 Charge Injection and Transport

The flow of current through an OLED is the result of the injection and transport of charge carriers. Charge injection is significantly affected by the energy level alignment at organic/electrode interfaces, a fundamental phenomenon that strongly influences the overall performance of OLEDs. A well-known textbook model for understanding the energy level alignment at semiconductor/metal interfaces is Mott-Schottky model.⁹ **Figure 1.3** shows an example of an interface between a metal and an n-type semiconductor. When the organic solid and metal are isolated, the energy levels of the two solids are aligned at the common vacuum level between the two solids. When the two solids make contact, the Mott-Schottky model assumes (1) a vacuum level alignment right at the interface region and (2) band bending in the space charge layer to achieve the alignment of the bulk Fermi levels between them. The thermal equilibrium state, in which Fermi level is constant everywhere in the system, is assumed to be achieved. Since the Fermi level of the semiconductor coincides with that of the metal, the built-in potential coincides with the difference in the work function between the metal and the semiconducting solid.

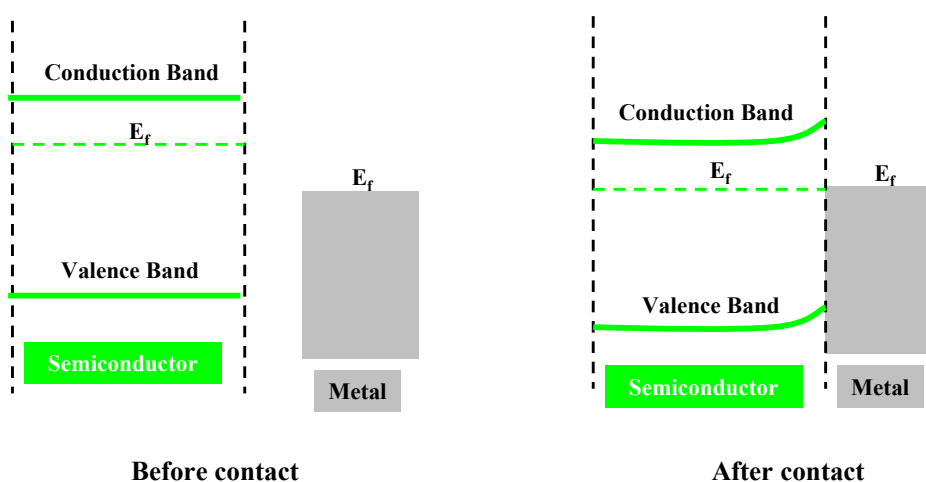


Figure 1.3: Energy level alignment at a semiconductor/metal interface.

The model above is a very classical and simple one despite that it has been used in OLEDs for a long time. As for the first assumption in this model, studies revealed that vacuum level alignment does not occur in most organic/metal interfaces due to the formation of an interface dipole inducing vacuum level shift Δ .¹⁰ The existence of Δ demonstrates that the barrier height estimated from the Mott-Schottky model has to be modified by the amount of Δ . Build-in voltage should be also modified by the same value. Moreover, the energy gap between HOMO and LUMO levels of most organic materials widely used in OLEDs is usually 2 - 3 eV. The concentration of thermally excited carriers in organic semiconductors is therefore extremely low. In addition, organic semiconductors are essentially molecular solids where molecules are bound by Van der Waals forces, and the wavefunctions and charge density are fairly localized within each molecule. This means that the carrier exchange process between adjacent molecules is not effective, which is in stark contrast to the case of inorganic semiconductors. As for the second assumption in the Mott-Schottky model, the mismatch in the Fermi level cannot be compensated by the redistribution of carriers and, as a result, the band-bending effect at organic/metal interfaces is usually negligible.

Instead, two models were proposed to explain the charge carrier injection behavior from a metal contact to an organic layer, (1) quantum mechanical tunneling of carriers through a triangular energy barrier and (2) field-assisted thermionic injection over an image force barrier. Their approximate physical pictures and the corresponding equations are illustrated in **figure 1.4**.

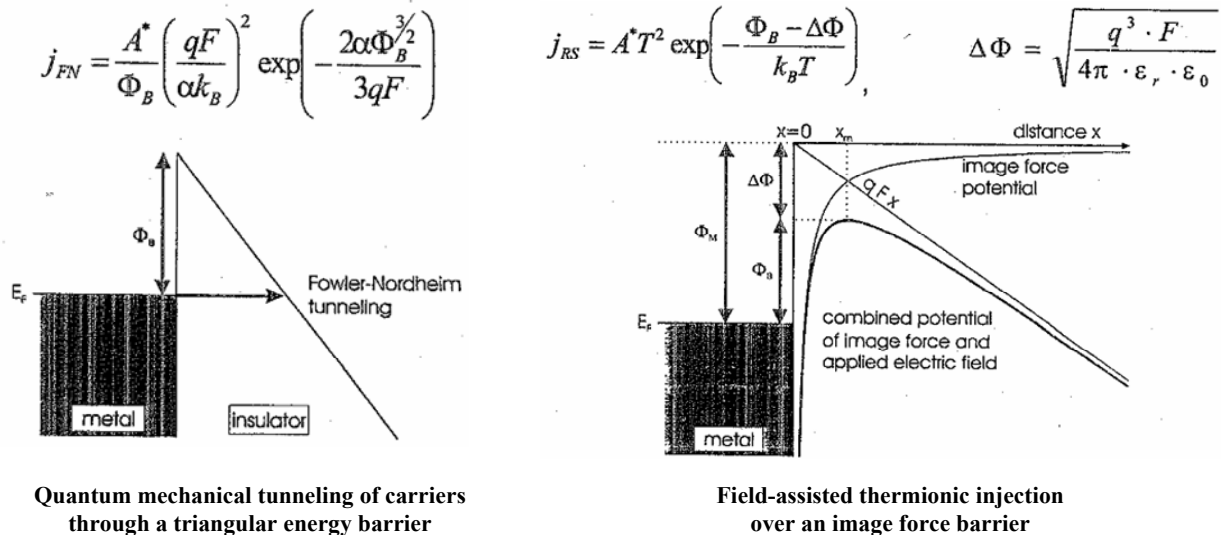


Figure 1.4: Two models for charge carrier injection from a metal contact to an organic layer.¹¹

The transport of charge carriers in organic semiconductors is dependent on π -bonding orbitals and the overlap of quantum mechanical wavefunctions. In organic semiconductors, there is limited π -bonding overlapping between molecules, indicating a weaker electronic delocalization. The conduction of charge carriers is therefore described by the quantum mechanical tunneling of charge carriers from one molecule to another. Due to the quantum mechanical tunneling nature of the charge transport and its dependence on a probability function, the transport process is commonly referred to as hopping transport. The mobility in hopping transport depends on both temperature and applied electric field (i.e. $\mu \propto \exp(-\Delta E/kT)\exp(\beta\sqrt{F}/kT)$), which is in stark contrast to the band transport characteristics in inorganic semiconductors where the mobility depends only on temperature (i.e. $\mu \propto T^{-n}$).

A more accurate physical picture for describing the transport of charge carriers in semiconductors is polarons. A polaron is essentially a quasiparticle composed of a charge and its accompanying polarization field. The polaron concept was proposed to describe a charge carrier (electron or hole) moving in a solid material where the atoms (or molecules) move from their equilibrium positions to effectively screen the electric charge of the carrier. This lowers the carrier mobility and increases its effective mass. The mobility of charge carriers in semiconductors can be greatly decreased by the formation of polarons. Organic semiconductors are also sensitive to polaronic effects. In this work, the two words “charge” and “polaron” are often used interchangeably.

1.2.3 Exciton Formation and Dissipation

An exciton is a bound state of an electron and a hole in a semiconductor or insulator, bound through Coulomb interaction. It is a quasiparticle in a solid, which provides a means to transport energy without transporting net charge. An example of exciton formation via photogeneration is as follows: a photon enters a semiconductor, exciting an electron from the valence band into the conduction band. The missing electron in the valence band leaves a hole behind, to which the electron is attracted by the Coulomb force. The exciton results from the binding of the electron with its hole. As a result, the exciton has slightly less energy than the unbound electron-hole pair.

Excitons can be classified into two categories, Wannier or Frenkel excitons, depending on the strength of the electron-hole interaction. The strength of such interaction is determined by the screening effect of the surrounding lattice. Polarized lattices, with high dielectric constant, ϵ , screen the electron-hole attraction more significantly, resulting in a smaller exciton binding energy. This

results in a Wannier exciton, which has a spatial extent much larger than the lattice spacing of the molecule. In less polarized lattices (i.e. low ϵ), the high exciton binding energy results in strongly bound Frenkel excitons, with a spatial extension of the same order as the intermolecular distance. In the case of organic semiconductors, excitons are primarily Frenkel ones, due to the generally lower dielectric constants of organic materials.

An exciton contains two unpaired electrons in different orbitals, and they can be of the same spin or different spins, corresponding to triplet and singlet excitons, respectively. The triplet exciton has a lower energy than the singlet exciton due to the repulsive nature of the spin-spin interaction between electrons of the same spin. From a quantum mechanical view, singlet and triplet states can be expressed as:

$$\left. \begin{array}{l} |1, 1\rangle = \uparrow\uparrow \\ |1, 0\rangle = (\uparrow\downarrow + \downarrow\uparrow)/\sqrt{2} \\ |1, -1\rangle = \downarrow\downarrow \end{array} \right\} s = 1 \text{ (triplet)}$$

$$|0, 0\rangle = (\uparrow\downarrow - \downarrow\uparrow)/\sqrt{2} \left. \right\} s = 0 \text{ (singlet)}$$

The equations above theoretically predict that 25% of the excitons that are created from uncorrelated electrons and holes in operating OLEDs are singlet while 75% are triplet.

Generally speaking, both singlet and triplet excitons are not long-lived (\sim ns for singlet excitons and \sim ms for triplet excitons¹²). They are forced to lose their energy within a period of time induced, collapsing to their ground states radiatively or non-radiatively. The processes responsible for their dissipation pathways are presented by the Jablonski-diagram shown in **figure 1.5**, in which S_0 is the ground state, S_1 is the first singlet excited state, S_2 is the second singlet excited state, T_1 is the first triplet excited state, A stands for absorption of photons, F stands for fluorescence, P stands for phosphorescence, VR is the abbreviation of vibrational relaxation, ISC is the abbreviation of intersystem crossing and IC is the abbreviation of internal conversion.

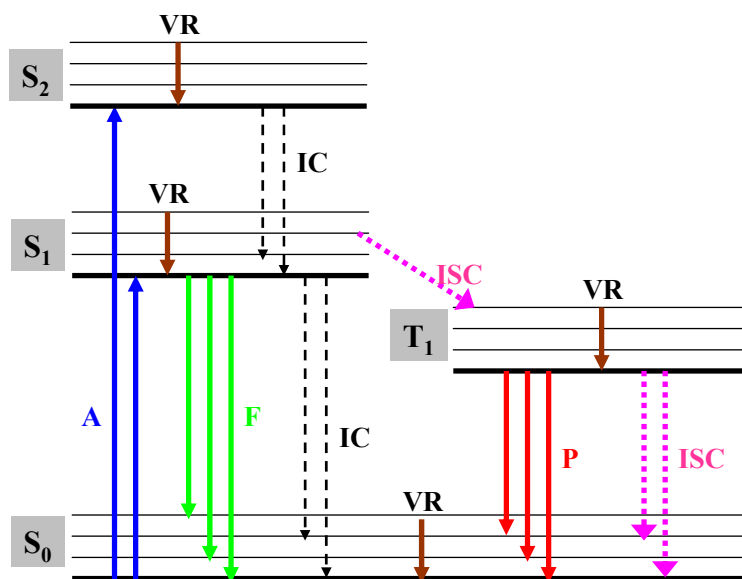


Figure 1.5: Jablonski diagram showing radiative and non-radiative dissipation pathways available to molecules.

As the figure shows, once a molecule is pumped up to an excited state from the ground state (e.g. $S_0 \rightarrow S_1$ or $S_0 \rightarrow T_1$), through, for example, optical excitation or electron-hole pair recombination, the pathways for the dissipation of electronic energy of the excited molecule can be classified into two major categories, radiative transitions and non-radiative transitions. In the case of radiative transitions, the excited molecule goes from a higher excited state to a lower one with the emission of a photon. There are two distinguishable processes in radiative transitions: (a) fluorescence, which results from a rapid radiative transition (\sim ns) between states of the same multiplicity, typically $S_1 \rightarrow S_0$ transition; and (b) phosphorescence, the result of a transition between states of different multiplicity, typically $T_1 \rightarrow S_0$. The rate of phosphorescence is usually much smaller than that of fluorescence in that phosphorescence is spin forbidden. However, the rate of phosphorescence can be dramatically increased by adding heavy atoms into molecules, which enables fast triplet dissipation due to strong spin-orbital coupling. Such molecular engineering is widely used in phosphorescent OLEDs.

Non-radiative transitions, on the other hand, arise from several different mechanisms. There are three processes in non-radiative transitions: (a) vibrational relaxation (VR), relaxation of a state to its lowest vibrational level, involving the dissipation of energy from a molecule to its surrounding molecules; (b) internal conversion (IC), a transition between isoenergetic states of the same spin

multiplicity; and (c) intersystem crossing (ISC), a transition between states of different spin multiplicity. The ISC from S_1 to T_1 is the fundamental principle for phosphorescent OLEDs in which a tremendous amount of triplets are harvested. The non-radiative transition between T_1 and S_1 however requires thermal activation of T_1 to a vibrational level isoenergetic with S_1 . In these non-radiative transitions, the energy of the excited state is given off to vibrational modes of the molecule. The excitation energy is therefore transformed into heat. It should be pointed out that the non-radiative processes are often competitive with the radiative processes (e.g. IC from S_1 to S_0 vs. fluorescence or ISC from T_1 to S_0 vs. phosphorescence) in order to deactivate an excited state, and the relative magnitude of the rate constants determines the contribution given by each pathway.

Based on the choice of emitter materials, OLEDs can be divided into two categories, fluorescent and phosphorescent OLEDs. Since both holes and electrons are fermions with half-integer spin, an exciton formed by the recombination of a hole and an electron may either be a singlet or triplet exciton, depending on how the spins have been combined. Statistically, there is a 25% probability of forming a singlet exciton and 75% probability of forming a triplet exciton.¹² In the case of fluorescent OLEDs, the decay of triplet excitons directly to the ground state is quantum mechanically forbidden by selection rules. It therefore follows that in fluorescent OLEDs only the decay of singlet excitons will lead to the emission of light, which naturally places a theoretical limit on device internal quantum efficiency (i.e. the percentage of excitons formed that relax radiatively) of 25%. In the case of PhOLEDs, on the other hand, the relaxation of triplet excitons via the emission of photons becomes allowed. The internal quantum efficiency can therefore reach nearly 100%.¹³ Such device efficiency unlocking is achieved by doping a wide-bandgap fluorescent host material with a phosphorescent guest made of an organometallic complex containing a heavy metal atom such as platinum or iridium at the centre of the molecule. The presence of such heavy metal atom brings very large spin-orbit coupling to the phosphorescent guest, facilitating singlet-triplet ISC, a process that essentially hybridizes the singlet-triplet characteristics of excitons.¹⁴ The dissipation pathways of singlet and triplet excitons in fluorescent and phosphorescent OLEDs are shown in **figure 1.6**. Owing to the unique capability in achieving high efficiency, PhOLEDs today have already become a primary option in the OLED industry.

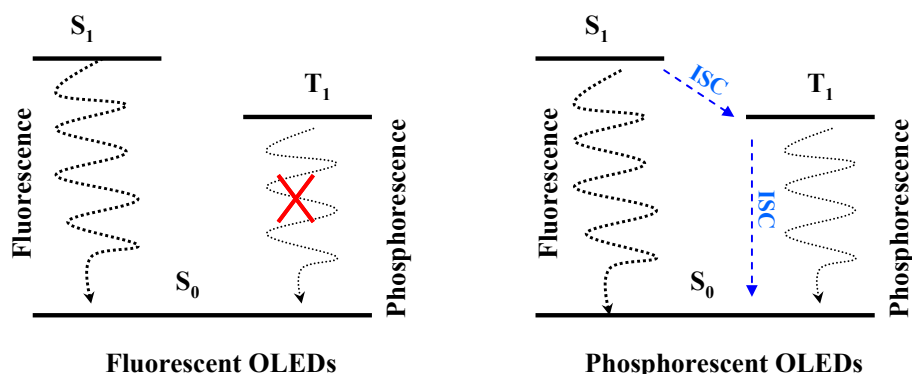


Figure 1.6: Dissipation pathways of single and triplet excited states in fluorescent and phosphorescent OLEDs.

1.3 OLEDs Stability

Despite the significant progress in the last two decades in realizing high performance OLEDs and the commercialization in a few consumer products in recent years, one of the biggest technical barriers for their wider commercial presence in areas such as flat-panel displays and solid-state lighting remains the rapid device EL degradation (i.e. a continuous decrease in device luminance during device operation). Specifically, the EL stability of blue devices is still much lower than that of green and red devices. As blue, green and red are necessary for full-color displays and white lighting, such difference in device stability between blue and the other two leads to serious problems such as differential color aging and continuous shift in color balance points. Moreover, the limited device EL stability is particularly more severe in case of PhOLEDs, an issue that still prevents their full utilization in commercial products. **Table 1.1** presents the state-of-the-art performance of PhOLEDs from Universal Display Corporation. As the table shows, the lifetime of blue PhOLEDs is significantly shorter than that of red and green ones. Understanding the underlying degradation mechanism is therefore a prerequisite for the realization of devices with prolonged stability.

PhOLEDs (at 1000 cd/m ²)	CIE Coordinates	Current Efficiency (cd/A)	Operating Lifetime (hour, LT 95%)
Red	(0.65, 0.35)	30	40,000
Green	(0.31, 0.63)	85	18,000
Blue	(0.18, 0.42)	50	700

Table 1.1: Performance of phosphorescent OLEDs from Universal Display Corporation.¹⁵

1.4 Thesis Outline

The thesis is organized into seven chapters. Chapter 1 gives an introduction and some background theory of OLEDs. Chapter 2 first focuses on a detailed literature review on OLEDs degradation mechanisms, and then proposes the motivations and objectives of this study. Chapter 3 covers all the experimental methods used in this study. Chapter 4, 5 and 6, as the main body of the thesis, present results on exciton-induced degradation of organic/metal interfaces, ITO/organic interfaces and organic/organic interfaces, respectively. Chapter 7 summarizes the main findings and suggests future work.

Chapter 2

Degradation Mechanisms of OLEDs

Degradation of an OLED is essentially a process in which the device gradually loses its luminance (measured under a constant current density) with time. The degradation can typically occur via two independent modes, ambient degradation and intrinsic degradation.

2.1 Ambient Degradation

Ambient degradation in OLEDs is primarily associated with the formation of dark-spots, i.e. non-emissive defects within the emissive area of a device, even without the device having been subjected to electrical stress. The areas of these dark-spots grow with time, causing a significant decrease in device emissive area, as shown in **figure 2.1**. The formation of dark-spots in an OLED can be mainly attributed to the evolution of structural defects (e.g. the crystallization and/or degradation of organic materials in the vicinity of the organic/cathode interface) due to the presence of ambient moisture that penetrates through pinholes in the top electrode or at other preexisting defects, eventually causing delamination at the organic/cathode interface and a permanent deterioration in charge carrier (i.e. electrons) injection.^{16,17}

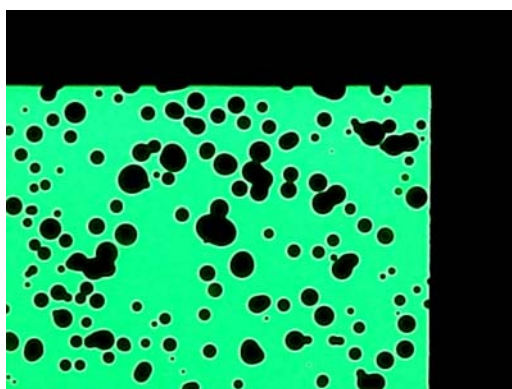


Figure 2.1: Formation of dark-spots in a corner of an OLED.

As ambient degradation arises essentially from the diffusion of ambient moisture and/or oxygen through the top electrode and device edges, it can be effectively suppressed by means of proper device encapsulation, as illustrated in **figure 2.2**. Moreover, as the underlying mechanisms have already been well understood, it no longer remains a research focus in the OLED community, and thus becomes a purely technical issue.

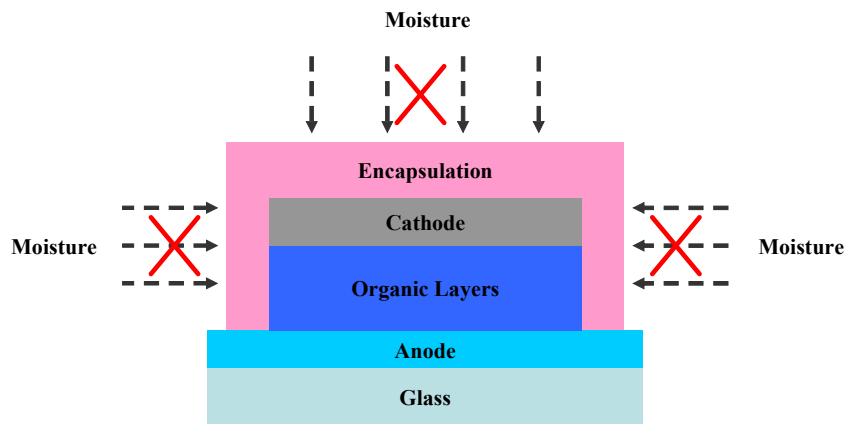


Figure 2.2: A schematic diagram showing OLED encapsulation.

2.2 Intrinsic Degradation

Intrinsic degradation in OLEDs is essentially a continuous decrease in device luminance when the device is driven by a current of constant density, as shown in **figure 2.3**. Such decrease in device luminance is always accompanied with an increase in device driving voltage. Different from the ambient degradation, the intrinsic degradation in OLEDs is not associated with any obvious change in device appearance (i.e. the growth of dark-spots).

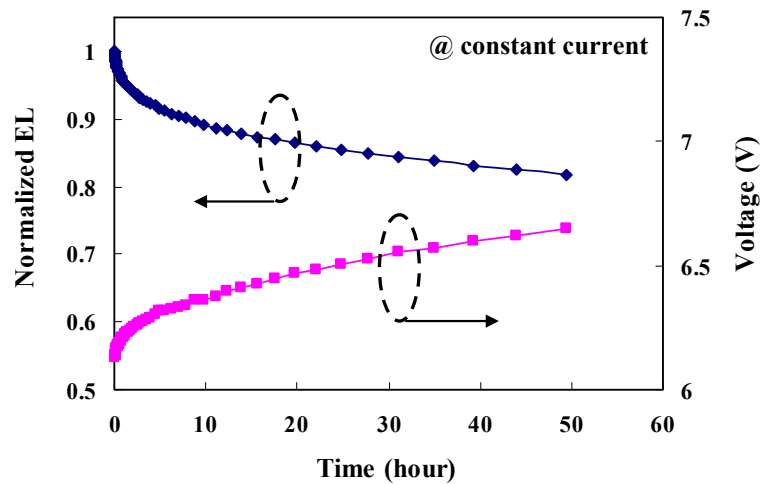


Figure 2.3: EL (normalized to initial intensity) and driving voltage versus time, collected from an OLED driven by a constant current.

The effective control of intrinsic degradation is far more challenging in comparison to that of ambient degradation. This is primarily due to the lack of a fundamental understanding on the underlying degradation behavior. Uncovering the root cause for intrinsic degradation is therefore still an active field in OLEDs research. In the past two decades, extensive studies were conducted in order to uncover the degradation mechanisms and a number of models were proposed. The most significant ones include (1) unstable cationic molecules model, (2) space-charge accumulation model, (3) chemical degradation by excitons model and (4) exciton-polaron annihilation model.

2.2.1 Unstable Cationic Molecules Model

The pioneer work on uncovering the intrinsic degradation of OLEDs was first done in the most widely used fluorescent emitter tris(8-hydroxyquinolino)aluminium (AlQ₃) in 1999.¹⁸ The degradation of AlQ₃-based devices was well explained by the unstable cationic molecules model. In this model, device degradation is attributed to the transport of holes into AlQ₃ and the subsequent formation of cationic AlQ₃ species, which causes a decrease in AlQ₃ fluorescence quantum efficiency. The degradation products are fluorescence quenchers, and thus lead to a decrease in device EL. On the other hand, the transport of electrons into AlQ₃ and the subsequent formation of anionic AlQ₃ species do not cause any significant change in AlQ₃ fluorescence quantum efficiency.

This model sheds a light on an approach for stabilizing OLEDs by reducing injection of holes into AlQ₃ molecules. A number of methods based on this principle such as doping of the hole-transport layer,¹⁹ introducing a buffer layer at the hole-injecting contact,²⁰ and using mixed emitting layers of hole-transport and AlQ₃ molecules¹⁸ successfully improve the lifetime of OLEDs.

2.2.2 Space-Charge Accumulation Model

Inspired by the unstable cationic molecules model, researchers in the OLED community further investigate whether the presence of charges (holes or electrons), as a result of current flow under device normal operation, plays a more general role in device degradation. It is found that the decrease in luminance efficiency in an OLED during aging is linearly correlated with an accumulation of immobile positive charges (possibly holes) in the vicinity of the HTL/ETL interface (i.e. the electron-hole recombination zone in double-organic-layer devices).²¹ The amount of the accumulated holes is found to be comparable to the total charges at the HTL/ETL interface in a fresh device under normal operation. A straightforward explanation for the correlation between the luminance loss and hole accumulation is therefore that the flow of current during device electrical aging generates defects that

are capable of trapping holes. Similarly, defects that can trap electrons are also found to be present in the vicinity of the HTL/ETL interface in OLEDs under prolonged electrical driving.²²

The accumulation of space charge (i.e. immobile holes and electrons) at the HTL/ETL interface due to device aging in turn causes a significant decrease in device luminance efficiency. This can occur via one of the two processes: (i) non-radiative recombination of a mobile electron (or hole) and a trapped hole (or electron), and (ii) quenching of emitter excitons by trapped charges via long-range Forster energy transfer.

Knowing that a strong correlation between the buildup of space charge in the recombination zone and device degradation exists, the long-term stability of OLEDs has been significantly enhanced by reducing the accumulation of space charge via utilizing HTL/ETL mixing layers.²³

2.2.3 Chemical Degradation by Excitons Model

Different from the unstable cationic molecules model and space charge accumulation model, in which the degradation of OLEDs is caused by charge carriers (holes or electrons), the chemical degradation of excitons model claims that the device degradation mainly arises from chemical degradation of organic molecules when in their excited states (i.e. excitons).^{24,25,26,27,28,29,30}

Two types of techniques can be used in this model for investigating the chemical composition of degradation products in OLEDs, high-performance liquid chromatography (HPLC)²⁵ and laser-desorption/ionization time-of-flight mass spectrometry (LDI-TOF-MS).²⁹ In both techniques, OLEDs are electrically driven for a period of time until the devices have completely degraded. When analyzing the chemical nature of the potential degradation products, the two types of techniques follow different approaches. HPLC requires the organic materials in aged devices to be dissolved in a solvent and analyze the solution, whereas LDI-TOF-MS can analyze the organic materials in aged devices as they are (i.e. without special treatment such as dissolving the devices). Both techniques managed to detect the presence of new chemical compositions in electrically degraded devices, which were identified to be degradation products due to bond cleavage of organic molecules.

Despite that the bond dissociation energies are not available for the organic molecules used in OLEDs, the stimulus for such bond cleavage is attributed to molecules that are in their singlet excited states (i.e. singlet excitons).²⁵ Meanwhile, no signs of chemical degradation in organic materials that are subjected to the flow of hole-only or electron-only current were detected,²⁵ ruling out the possibility that cationic or anionic molecules may cause device degradation.

2.2.4 Exciton-Polaron Annihilation Model

The exciton-polaron annihilation model is proposed to account for the luminance loss due to electrical driving primarily in PhOLEDs. In contrast to the previous models in which device degradation behavior was identified to be caused by single stimulus (either charges or excitons alone) via intramolecular/unimolecular processes, i.e., a molecule degrades on its own when it is charged or in an excited state without interacting with neighboring molecules, the exciton-polaron annihilation model however ascribes device degradation to intermolecular processes in which both excitons and charges play important roles.^{31,32}

In this model, the co-existence of host negative polarons (i.e. electrons on host molecules) and guest triplet excitons is found to cause rapid PhOLEDs degradation, whereas the presence of host polarons or guest excitons alone shows no detectable effect on device degradation.³¹ The degradation process of PhOLEDs is therefore attributed to exciton-polaron annihilation between host and guest molecules in which the energy of guest excitations is transferred to adjacent host polarons resulting in the formation of host excited polarons and the subsequent dissociation of host molecules. The non-radiative dissociation products are capable of quenching guest triplet excitons and also act as charge-trapping centers, causing the observed luminance loss and operating voltage rise in PhOLEDs.

As higher amount of energy provided to host molecules generally indicates higher possibility of molecular decomposition, it follows that the exciton-polaron annihilation rate and device degradation depends on the energy of guest excitons. In this regard, red phosphorescent OLEDs would show the best stability, followed by green and then by blue devices, due to the fact that red-emitting guest molecules produce less energetic host excited polarons via the exciton-polaron annihilation process than green- or blue-emitting guest molecules do. This general trend was observed in a number of studies.^{33,28} The exciton-polaron annihilation model thus provides an explanation for the dependence of device degradation on emission wavelength.

2.3 Limitation with Existing Knowledge

Despite the success in identifying several important degradation phenomena, it has always been very difficult, if not impossible, to explain device intrinsic degradation by a single theory, mainly because the degradation involves many different chemical/physical or photo-chemical/photo-physical processes that may be governed by completely unrelated factors. As a result, the existing models all more or less have limitation.

In the case of the unstable cationic molecules model, the major limitation is that it primarily applies to AlQ₃-based fluorescent OLEDs only. There is however no evidence that such model can also explain degradation phenomena in other fluorescent OLEDs or PhOLEDs.³⁴

In the case of the space-charge accumulation model, despite revealing very important phenomena on device degradation, it still has two major limitations. Firstly, correlation does not imply causation. Specifically, the correlation between the accumulation of space charge and device luminance loss does not necessarily imply that one causes the other. It is entirely possible that the two phenomena are both caused by a third factor through an unknown mechanism, which essentially may be the root cause of device degradation. Secondly, the observations and conclusions in this model originate mainly from electrical/physical measurements, thus no information with respect to the chemical nature of the space charge can be revealed, not to mention its origin and the process of formation.

In the case of the chemical degradation by excitons model, although the emergence of new species as a result of molecular decomposition is evident, whether they truly emerge in OLEDs under normal device operation and thus are the real degradation products are not fully clear. For example, the devices prepared for the HPLC and LDI-TOF-MS measurements are all extremely over-aged (e.g. the luminance of the devices has decreased to ~ 5% or even less of the initial value). However, the lifetime of an OLED is typically defined as the time elapsed during which the luminance has decreased to 70% or at most 50% of the initial value. In this regard, it is entirely possible that the degradation mechanism by which the luminance has decreased to 5% of the initial value is essentially dissimilar to that by which the luminance has decreased to only 70% or 50%. Therefore, the identified new species in the HPLC and LDI-TOF-MS measurements may not be the real degradation products in OLEDs under normal operation. It would be more relevant to the real degradation scenario if the devices for HPLC or LDI-TOF-MS measurements were aged until the luminance has decreased by just 50%. In fact, no evidence of molecular chemical degradation has been detected by the HPLC measurement in a device that has been electrically aged until its luminance decreases to as low as ~10% of the initial value,²⁵ suggesting that the technique itself may not be sensitive enough and/or the chemical degradation of excitons model may not play a major role in OLEDs degradation.

In the case of the exciton-polaron annihilation model, despite the significant progress made by this model in revealing the complexity of the degradation process in PhOLEDs, it still has several limitations in accounting for other key degradation phenomena. Firstly, it does not provide any clue

why there are often non-negligible variations in the lifetimes of devices containing emitter guests of similar excitation energy (thus similar emission wavelength). A widely known example is that devices containing emitter guests tris(2-phenylpyridine)iridium (Ir(ppy)_3) and bis(2-phenylpyridine)(acetylacetonate)iridium ($\text{Ir(ppy)}_2\text{acac}$) exhibit very different device lifetimes,^{35,33} despite that the two green emitters have essentially very similar bandgap and thus similar exciton energy. Secondly, this model cannot well explain the reason behind the generally lower stability of phosphorescent OLEDs relative to their fluorescent counterparts. All the two limitations originate essentially from a drawback in the model that it fails to consider whether/how emitter guests degrade. Moreover, negative polarons that reside on host molecules are found to play a significant role in this model, whereas positive polarons are not. However, negative polarons are generally minority carriers whereas positive polarons are major carriers in host materials due to the fact that the hole mobility of host materials is typically orders of magnitude higher than the electron mobility.²¹ Therefore, the population of positive polarons is expected to be more dominant relative to that of negative polarons in the electron-hole recombination zone in a PhOLED under normal operation. The root cause for such inconsistency is possibly that the design of the hole-current-only device in the study by Giebink et al.³¹ is flawed, i.e., not creating an interface having an energy barrier for the accumulation of holes in the host material, just as the scenario in the recombination zone of a bi-polar device. As a result, holes could rapidly transport through host molecules, which may not easily enable the occurrence of annihilation interactions between excitons and positive polarons.

In summary, the existing models appear to apply to a limited number of material systems only on a nearly case-by-case basis, and therefore are not able to provide explanations for some fundamental observations such as the generally much lower stability of blue devices relative to their green and red counterparts, especially in case of phosphorescent emitters, and the generally lower stability of phosphorescent OLEDs relative to their fluorescent counterparts.

2.4 Motivations and Objectives

There are numerous observations from previous studies, as well as an established understanding, that interfaces play a role in device performance such as efficiency and stability, but in the same time nobody knows exactly how or for what reasons the interfaces degrade. Most studies (including the models above) primarily focused on degradation phenomena that occur in the organic materials bulk. None has particularly emphasized the important role of interfaces, such as organic/organic interfaces and organic/electrode interfaces, in device degradation, not to mention revealing the underlying

mechanisms. In this thesis, the ultimate goal is to uncover the intrinsic failure modes in OLEDs. The research in this work focuses on degradation behavior at interfaces, including organic/organic, organic/metal and ITO/organic interfaces. The study aims at revealing degradation mechanisms that can explain a wide range of degradation phenomena in OLEDs.

The purpose of the study will be achieved by studying the following research objectives:

(a) Exciton-induced degradation of organic/metal interfaces:

- (i) Degradation mechanisms.
- (ii) Role in device EL loss.
- (iii) Approaches for suppressing interfacial degradation.

(b) Exciton-induced degradation of ITO/organic interfaces:

- (i) Degradation mechanisms.
- (ii) Role in device EL loss.
- (iii) Approaches for suppressing interfacial degradation.

(c) Degradation of organic/organic interfaces due to exciton-polaron interactions:

- (i) Degradation mechanisms.
- (ii) Role in device EL loss.
- (iii) Effect on morphological changes of organic materials.
- (iv) Implication on the difference in EL stability between PhOLEDs and their fluorescent counterparts.
- (v) Implications on the much lower stability of blue PhOLEDs relative to their green and red counterparts.

Results and discussion arising from these research objectives will be given in depth in chapters 4, 5 and 6.

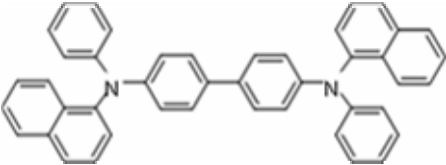
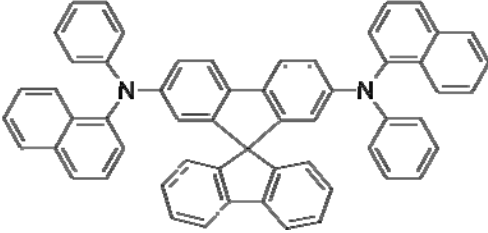
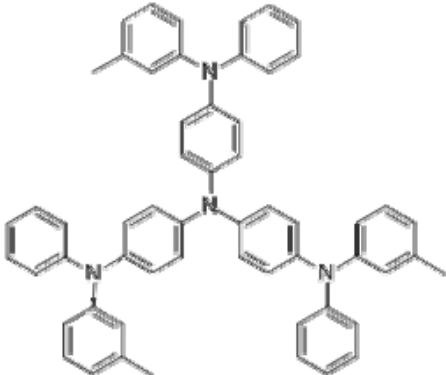
Chapter 3

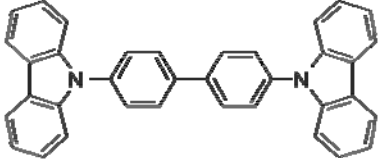
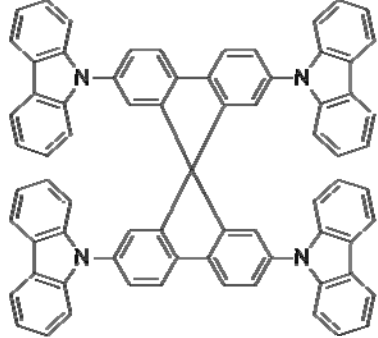
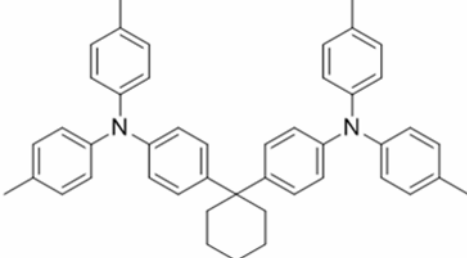
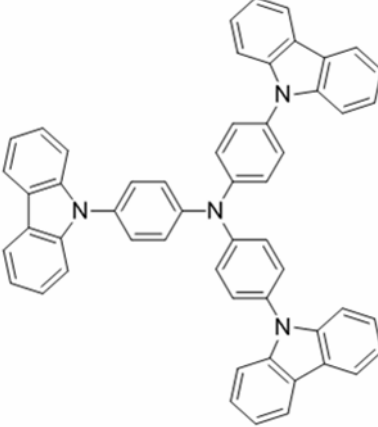
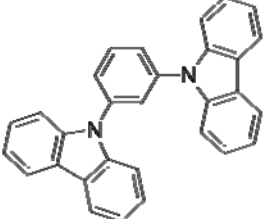
Experimental Methods

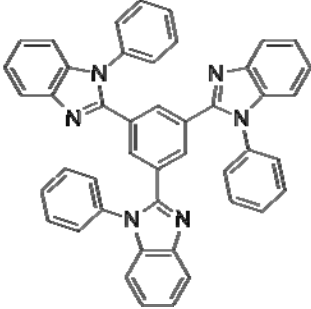
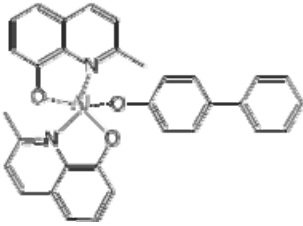
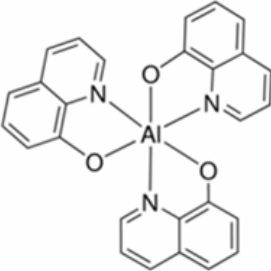
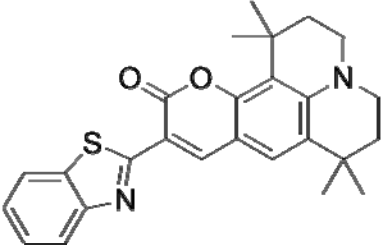
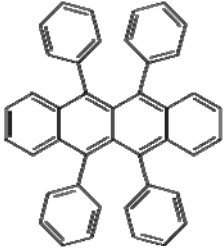
In this chapter, experimental methods including choice of materials, test-device configurations, device fabrication and device characterization will be introduced. A number of important measurement and analysis techniques will also be introduced.

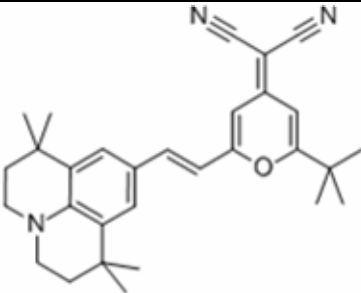
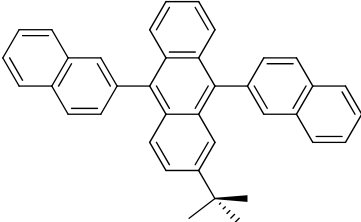
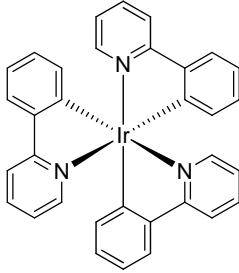
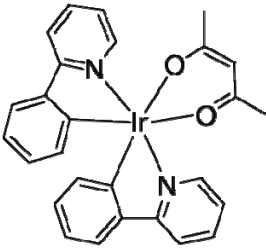
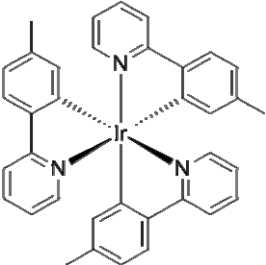
3.1 Materials

A variety of organic materials are used in this study. Their abbreviations, molecular structures and functions in devices are shown in **table 3.1**.

Chemical Name and Abbreviation	Chemical Structure	Functions in OLEDs
N,N' -Bis(naphthalen-1-yl)-N,N' -bis(phenyl)-benzidine (NPB)		Hole-Transport Material
N,N' -Bis(naphthalen-1-yl)-N,N' -bis(phenyl)-2,7-diamino-9,9-spirobifluorene (Spiro-NPB)		Hole-Transport Material
4,4',4''-Tris(N-3-methylphenyl-N-phenylamino)triphenylamine (m-MTDATA)		Hole-Transport Material

<p>4,4'-Bis(carbazol-9-yl)biphenyl (CBP)</p>		<p>Hole-Transport Material & Emitter Host</p>
<p>2,7-Bis(carbazol-9-yl)-9,9- ditolylfluorene (Spiro-CBP)</p>		<p>Hole-Transport Material & Emitter Host</p>
<p>Di-[4-(N,N-di-p-tolyl-amino)- phenyl]cyclohexane (TAPC)</p>		<p>Hole-Transport Material & Emitter Host</p>
<p>4,4',4''-Tris(carbazol-9- yl)triphenylamine (TCTA)</p>		<p>Hole-Transport Material & Emitter Host</p>
<p>1,3-Bis(carbazol-9-yl)benzene (mCP)</p>		<p>Hole-Transport Material & Emitter Host</p>

<p>2,2',2''-(1,3,5-Benzinetriyl)- tris(1-phenyl-1-H- benzimidazole) (TPBi)</p>		<p>Electron-Transport Material</p>
<p>Bis(2-methyl-8-quinolinolate)- 4-(phenylphenolato)aluminium (BAIq)</p>		<p>Electron-Transport Material</p>
<p>Tris(8-hydroxy- quinolinato)aluminium (Alq₃)</p>		<p>Electron-Transport Material & Green Fluorescent Emitter</p>
<p>2,3,6,7-Tetrahydro-1,1,7,7,- tetramethyl-1H ,5H ,11H -10- (2- benzothiazolyl)quinolizino[9,9a ,1gh]coumarin (C545T)</p>		<p>Green Fluorescent Emitter</p>
<p>5,6,11,12- Tetraphenylnaphthacene (Rubrene)</p>		<p>Red Fluorescent Emitter</p>

<p>4-(Dicyanomethylene)-2-tert-butyl-6-(1,1,7,7-tetramethyljulolidin-4-yl-vinyl)-4H-pyran (DCJTB)</p>		<p>Red Fluorescent Emitter</p>
<p>2-tert-Butyl-9,10-di(naphth-2-yl)anthracene (TBADN)</p>		<p>Blue Fluorescent Emitter</p>
<p>Tris(2-phenylpyridine)iridium (Ir(ppy)₃)</p>		<p>Green Phosphorescent Emitter</p>
<p>Bis(2-phenylpyridine)(acetylacetonate)iridium (Ir(ppy)₂acac)</p>		<p>Green Phosphorescent Emitter</p>
<p>Tris[2-(p-tolyl)pyridine]iridium (Ir(mppy)₃)</p>		<p>Green Phosphorescent Emitter</p>

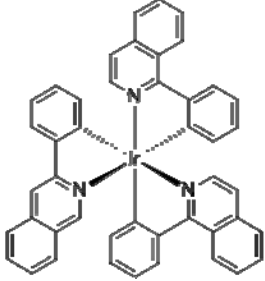
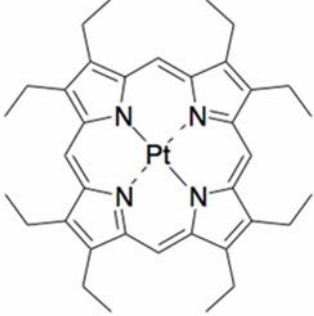
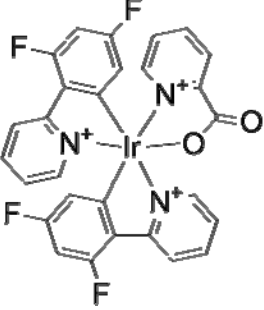
<p>Tris(1-phenylisoquinoline)iridium (Ir(piq)₃)</p>		<p>Red Phosphorescent Emitter</p>
<p>Platinum octaethylporphine (PtOEP)</p>		<p>Red Phosphorescent Emitter</p>
<p>Bis(3,5-difluoro-2-(2-pyridyl)phenyl-(2-carboxypyridyl)iridium (FIrpic)</p>		<p>Blue Phosphorescent Emitter</p>

Table 3.1: Organic molecules used in this study.

3.2 Test-Device Configurations

3.2.1 OLEDs

OLEDs studied in this work have primarily one of the two types of structures, double-organic-layer structure and “simplified” structure, as shown in **figure 3.1**. The double-organic-layer structure was first demonstrated by Tang *et al.*² in 1987, consisting of a HTL and an ETL sandwiched between a transparent indium tin oxide (ITO) anode and an opaque low-workfunction metal cathode (e.g. Al or Mg). The development was recognized as one of the most significant steps towards the application of OLEDs technology. Such device structure has thus become a standard practice for most fluorescent OLEDs. The “simplified” structure, on the other hand, was first demonstrated by Helander *et al.*³⁶ in

2011, by removing the HTL in the structure of conventional PhOLEDs and modifying the ITO surface in order for a direct hole injection from the ITO anode into a wide-bandgap host material. In this regard, the wide-bandgap material acts as both HTL and emitter host. The “simplified” structure has advantages in improving device efficiency and simplifying device fabrication process in comparison to conventional structures, and is therefore widely used in highly efficient PhOLEDs. For both double-organic-layer and “simplified” structures, inorganic interfacial layers at the two organic/electrode interfaces are used for efficient charge carrier injection from the electrodes to the adjacent organic layers. Typical electrode interfacial layers include hole-injection layer (HIL) MoO₃ and electron-injection layer (EIL) LiF.

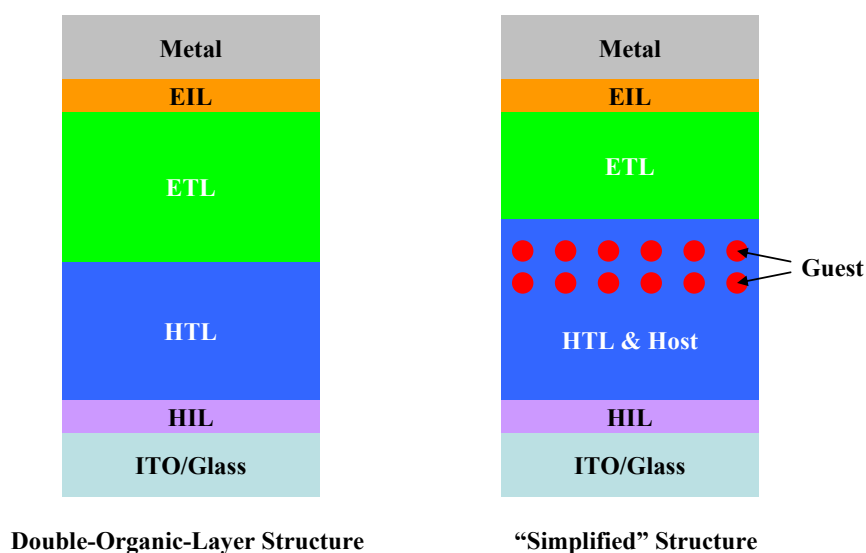


Figure 3.1: General structures of OLEDs used in this study.

3.2.2 Single-Carrier Devices

OLEDs are bipolar devices in which both electrons and holes are majority carriers. Single-carrier devices, on the other hand, are unipolar devices, which allow the flow of either holes or electrons only. The purpose of using single-carrier devices is to independently investigate the injection and transport characteristics of single carriers (electrons or holes) in a material. This is achieved by blocking one type of carriers from one electrode with an inorganic carrier-blocking layer (i.e. hole-blocking layer (HBL) or electron-blocking layer (EBL)). Specifically, hole-only and electron-only single-carrier devices have general structures of ITO/HTL/EBL/Metal and ITO/HBL/ETL/Metal, respectively, as shown in **figure 3.2**. **Figure 3.3** shows the corresponding energy diagrams of the two

types of single-carrier devices. For example, in the case of the hole-only device, when under a forward bias (i.e., the ITO is positively biased relative to the metal), the injection of electrons from the metal electrode is blocked by the EBL, and therefore the flow of current occurs exclusively by holes injected from the ITO electrode. As a result, the device exhibits unipolar hole-only transport characteristics.

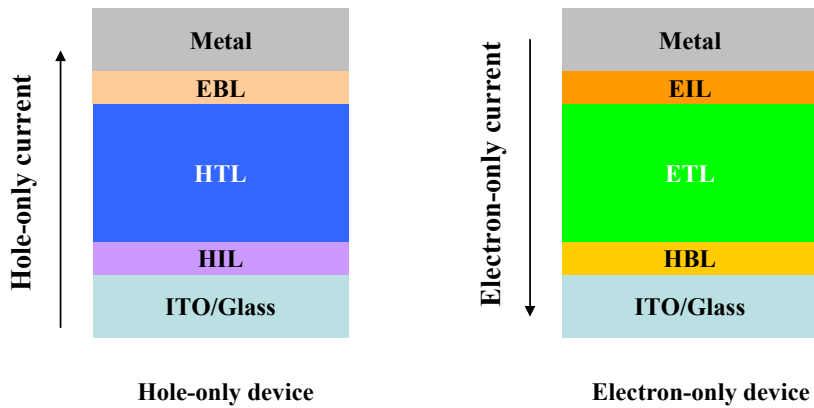


Figure 3.2: Schematic structures of hole-only and electron-only single-carrier devices.

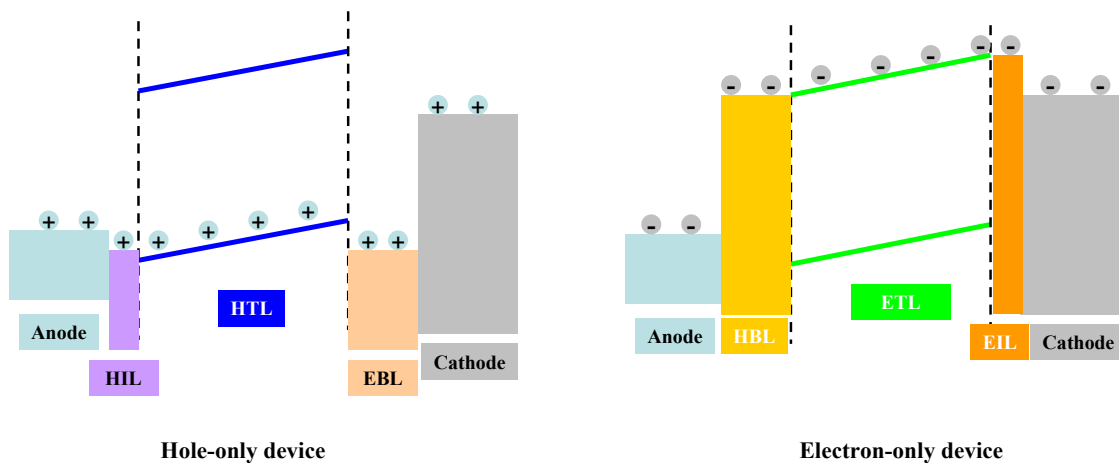


Figure 3.3: Energy diagrams of hole-only and electron-only devices.

The charge distribution across the charge-transport layers in the single-carrier devices in figure 3.2 is approximately uniform due to the uniform electric field between the two electrodes and the homogeneous mobility of the charge-transport layers. Such charge distribution in the devices can however be altered by adding an additional charge-transport layer of the opposite polarity into the existing charge-transport layer. **Figure 3.4** presents the structures of modified single-carrier devices,

in which thin layers of ETL and HTL are inserted into the existing hole-only and electron-only devices, respectively. **Figure 3.5** shows the corresponding energy diagrams. Obviously, as the figure shows, the insertion of the additional layers creates charge accumulation at the HTL/ETL interfaces due to the presence of energy barriers at the interfaces. As a result, single-carrier devices with non-uniform carrier distributions across the organic layers are realized.

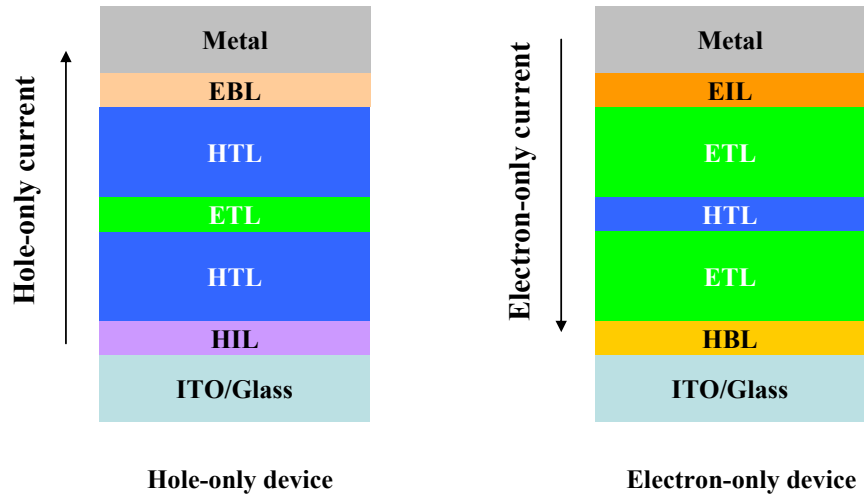


Figure 3.4: Schematic structures of modified hole-only and electron-only devices.

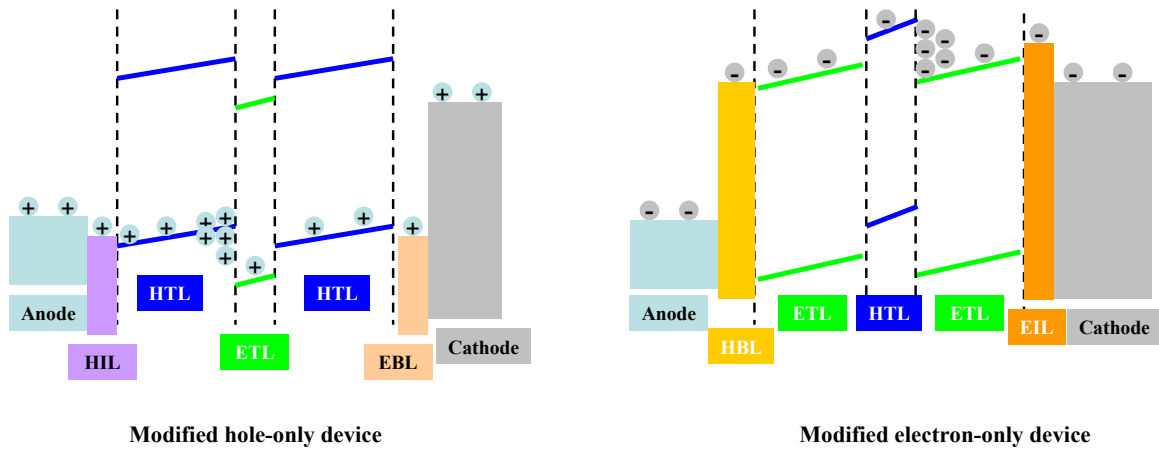


Figure 3.5: Energy diagrams of modified hole-only and electron-only devices.

3.2.3 Converting Single-Carrier Devices into Bipolar Devices

Single-carrier devices, specifically hole-only devices, can be converted into bipolar devices (i.e. OLEDs). The process is illustrated in **figure 3.6**, in which the top metal electrode of a hole-only

device is peeled off by a scotch tape (the inorganic EBL would also be peeled off with the metal as the adhesion of inorganic/inorganic interfaces is much stronger than that of organic/inorganic interfaces) and an EIL and metal cathode (e.g. LiF/Al) are deposited. As such, electron injection from the new cathode becomes possible. It however should be pointed out that there is always a very small amount of residual EBL material remaining on the ETL layer after the removal of the EBL and metal layers. The hole-only device is converted into bipolar devices, capable of EL, by replacing the top electrode with an electron-injecting cathode. This conversion technique is extensively used in chapter 6 and reveals very important information on the degradation behavior of organic/organic interfaces.

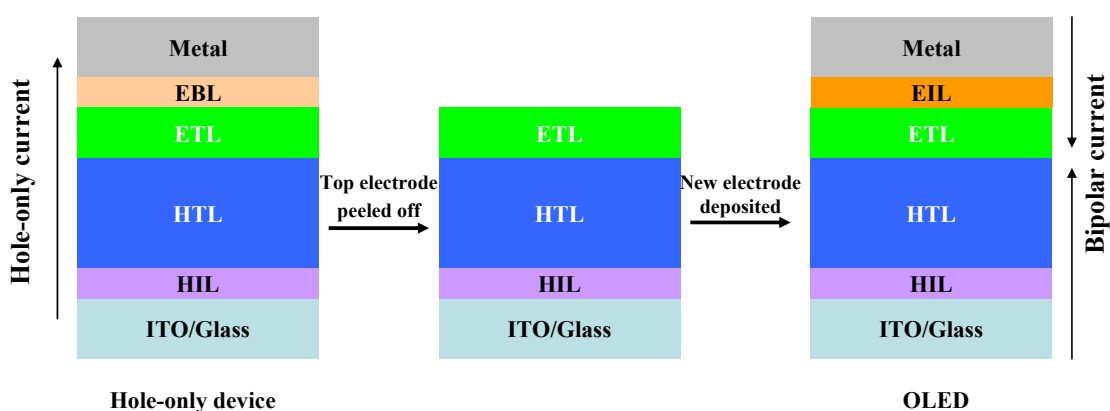


Figure 3.6: Process of converting a hole-only device into an OLED.

3.3 Device Fabrication and Characterization

In this work, all devices are fabricated by physical vapor deposition of organic materials and metals at rates ranging from ~ 0.01 to 3 \AA/s at a base pressure of $\sim 10^{-7}$ to 10^{-6} Torr using thermal evaporation on patterned ITO-coated glass substrates. The ITO thickness is $\sim 120 \text{ nm}$. Film thicknesses are monitored by a calibrated quartz crystal microbalance (QCM). Prior to materials deposition, ITO substrates are cleaned ultrasonically with acetone and isopropanol for 20 minutes, respectively. After device fabrication, basic device performance such as current-voltage-luminance (I-V-L) characteristics and EL spectra can be quickly measured. All the measurements are carried out in a N_2 atmosphere.

3.4 EL Stability Measurement

EL stability measurement is used to obtain the lifetime of an OLED. The test device is kept in a N_2 atmosphere to avoid any possible ambient degradation and continuously driven by a current of

constant density (typically 20 mA/cm^2). Both EL intensity and driving voltage versus electrical-driving time are collected, as already shown in figure 2.3. The lifetime of the device is typically defined as the time elapsed before the EL decreases to a percentage (such as 50 % or 70%) of its initial value. In this study, the lifetime value of any test device is obtained from the average lifetime of three to five identical devices. The standard deviation associated with the device lifetime is less than 5%.

3.5 Photo-Stability Measurement

Photo-stability measurement is used to study photo-induced changes in device interfacial resistance. In the measurement, an OLED or a single-carrier device is maintained in a N_2 atmosphere and exposed to monochrome illumination of different wavelengths from a 200W Hg-Xe lamp equipped with Oriel-77200 monochromator. The power density of the irradiation spot can vary from 0.2 to 2 mW/cm^2 . During the irradiation, an external voltage can be simultaneously applied to the device in order for a flow of electric current in the device. The current at a constant voltage (or the voltage at a constant current) versus the irradiation time are recorded. The photo-stability measurement is widely used in chapters 4 and 5.

3.6 Delayed EL Measurement

Delayed EL is a residual light emission from an OLED after the device is just switched off. It can typically last from a few tens of microseconds to several milliseconds, depending on the choice of emitter materials and device structures. Delayed EL measurement is a powerful technique for investigating triplet exciton dynamics and exciton-charge interactions in OLEDs.

In the delayed EL measurement, an OLED is subjected to a forward bias pulse (i.e., anode is positively biased relative to cathode) of a few volts in magnitude (e.g. 8 V) and $\sim 0.5 \text{ ms}$ in width, which is sufficiently long for prompt EL to reach its steady-state intensity. When the forward bias is removed, delayed EL will be collected after a time delay of $\sim 0.5 \text{ ms}$. **Figure 3.7** shows the schematic sequence for the acquisition of delayed EL from an OLED.

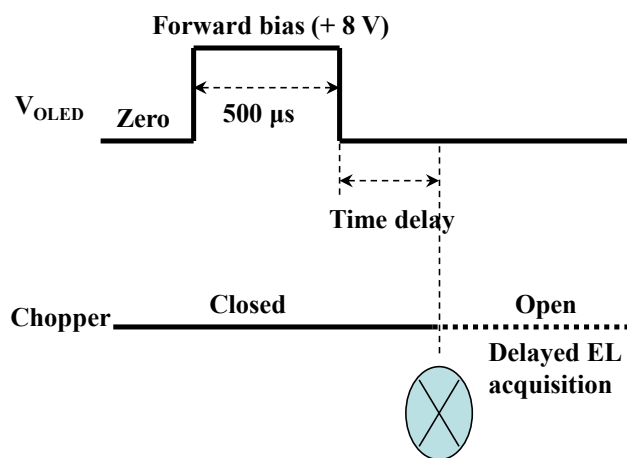


Figure 3.7: Schematic sequence for the acquisition of delayed EL.

As such 0.5 ms time delay is much longer than the lifetime of singlet states, the only species present in the device that can lead to delayed EL will be the long lived triplets and/or any un-recombined (i.e. residual) trapped charges. These two species (i.e. triplets and trapped charges) can produce delayed EL via one or two of the following processes: (1) delayed recombination of the de-trapped charges, and (2) triplet-triplet annihilation (TTA), in which two triplets interact upon collision to produce one singlet.³⁷

3.7 X-ray Photoelectron Spectroscopy

X-ray photoelectron spectroscopy (XPS) is a surface-sensitive quantitative spectroscopic technique that analyzes the surface chemistry, such as elemental composition and local bonding environment, of a material. In this study, XPS is used to mainly analyze chemical bonds between metal atoms and organic molecules at various organic/electrode interfaces. XPS is performed using a Thermo-VG Scientific ESCALab 250 Microprobe with a monochromatic Al KR source (1486.6 eV), capable of an energy resolution of 0.4–0.5 eV full width at half-maximum.

3.8 Interfacial Adhesion Test

Interfacial adhesion test is particularly used in this work to study the adhesion of organic/metal interfaces. A detailed experimental setup and methodology will be given in chapter 4 where it appears to be more relevant.

Chapter 4

Exciton-Induced Degradation of Organic/Metal Interfaces

Metal contacts are an integral part of OLEDs, used for injecting electrons into organic materials. In this chapter, degradation of organic/metal interfaces will be studied. Firstly, exciton-induced degradation of organic/metal interfaces will be investigated in section 4.1. The dependence of such interfacial degradation on energy-level conditions at organic/metal interfaces will be discussed in section 4.2. Finally, the use of interfacial layers and its role in improving OLEDs stability will be explored in section 4.3.

4.1 Investigation of Exciton-Induced Degradation of Organic/Metal Interfaces

The material presented in this section was published in *J. Appl. Phys.* **112**, 064502 (2012). It is reproduced here with the permission from the publisher.

First samples of the structure: ITO(120nm)/NPB(20 nm)/NPB:BAIq(50 nm, 1:1 by volume)/BAIq(30 nm)/Al(100 nm) were fabricated and tested. In these test samples, NPB serves as a hole-transport material and BAIq serves as an electron-transport material. Such structure has been widely used as an OPD (under reverse bias, i.e. when Al is at a more positive potential vs. ITO) or alternatively an OLED (under forward bias, i.e. when Al is at a more negative potential vs. ITO). **Figure 4.1(a)** shows the change in photo-current (I_{ph}) extracted from the device under a reverse bias of 7 V as a function of time during which the sample is exposed to 365 nm illumination at a power density of $\sim 0.5 \text{ mW cm}^{-2}$, normalized to the initial I_{ph} at time zero. The I_{ph} decreases by $\sim 10\%$ in 10 hours, which is consistent with previous report. In spite of the decrease in I_{ph} , photoluminescence (PL) measurements reveal no detectable decrease in the PL from the organic layers in the time frame. This observation suggests that the decrease in I_{ph} is not due to a significant loss in the light absorption of the bulk organic materials, for example due to possible photo-bleaching, or due a significant change in their fluorescence yield.

The changes in injection current under forward bias in the dark (I_{dark}) was also monitored. The results show that I_{dark} (at any given bias) decreases even more significantly due to irradiation. Figure 4.1(b) shows the changes in both I_{ph} (measured under a reverse bias of 7V) and I_{dark} (measured under a forward bias of 2.5 V, 3.5V and 5 V) of the same sample during irradiation. Clearly, the figure

shows a strong correlation between photo-induced changes in I_{ph} and I_{dark} , where a linear decline in I_{ph} is associated with a logarithmic decline in I_{dark} . From a charge transport viewpoint, I_{ph} depends on the magnitude of the electric field in the organic layers, which in turn is proportional to the externally applied voltage V_{bias} minus the voltage drop at the two contacts ($V_{contacts}$) caused by non-negligible contact resistance ohmic losses.^{38,39} On the other hand, I_{dark} , at low current densities, is governed primarily by the injection of charge carriers from the electrode to the organic layer. In this regard, current generally depends exponentially on the height of the energy barrier between the LUMO of the organic material and the work function of the electrode metal.⁴⁰ Given the linear versus logarithmic trends in I_{ph} and I_{dark} with irradiation, it follows that the changes must be arising from changes in the organic/electrode contacts rather than in the organic layers bulk. Knowing that the organic/metal contacts are susceptible to photo-degradation,⁴¹ one may conclude that the decrease in I_{ph} in figure 4.1(a) is mainly due to the photo-degradation of the BAQq/Al contact.

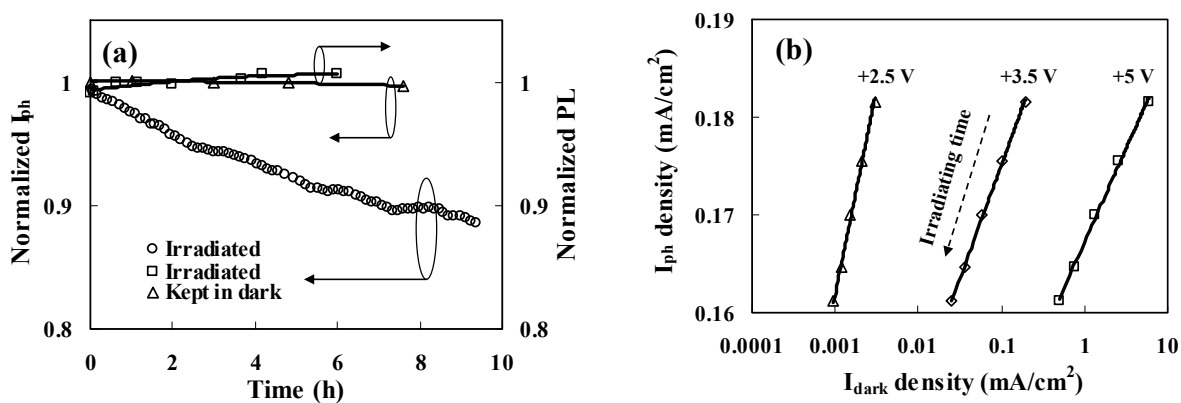


Figure 4.1: (a) Normalized I_{ph} (at a reverse bias of 7 V) and normalized PL versus irradiation time in samples of structure ITO/NPB(20nm)/NPB:BAQq(50nm)/BAQq(30)/Al(100nm). A 365 nm illumination at a power density of $\sim 0.5 \text{ mW cm}^{-2}$ is used for irradiation. The control sample kept in dark is also shown. (b) Changes in I_{ph} at a reverse bias of 7 V vs. I_{dark} at a forward bias of 2.5 V, 3.5 V and 5 V, respectively, during irradiation.

Since contact photodegradation behavior is found to impact I_{dark} much more severely than I_{ph} , changes in I_{dark} were monitored as a tool to probe changes in the organic/metal contacts. **Figures 4.2(a)** shows changes in I_{dark} (normalized to the initial I_{dark}) in samples of structure ITO/Alq₃(60nm)/Al(100nm) at a forward bias of 8 V as a function of time during which the samples are exposed to monochromatic irradiation of various wavelengths at a power density of $\sim 0.35 \text{ mW}$

cm^{-2} . As the figure show, only samples exposed to irradiation show an obvious decrease in I_{dark} , whereas the one kept in the dark shows no detectable change. This verifies that the decrease in I_{dark} is indeed photo-induced. Also, quite evidently, the rate of decrease in I_{dark} depends on the irradiation wavelength, despite the similar illumination power density. Figures 4.2(b) and (c) show results from similar tests on samples of structure ITO/Alq₃(60nm)/Ag(100nm) and ITO/Alq₃(60nm)/Mg(50nm)/Ag(50nm), respectively. Clearly, all samples show the same photodegradation behavior regardless of the metal used. Quite interestingly, samples in which a Cs₂CO₃ layer (~1nm thick) between the Alq₃ and the metal is introduced show much smaller decrease in I_{dark} at the same 405 nm irradiation. This further verifies that the photo-degradation is mainly occurring at the Alq₃/metal contact. That photodegradation rate depends on the irradiation wavelength despite the unchanged irradiation power density can be attributed to the fact organic molecules in their excited states are, by nature, more reactive than in their ground states, making them more susceptible to chemical changes. As exciton density depends on the extinction coefficient of the material at any given wavelength, one can expect that irradiation at wavelengths where optical absorption is higher can cause the photodegradation to be faster. To see if this is indeed the case, the % loss in I_{dark} in samples after irradiation for a period of 5 minutes at different wavelengths was compared with the ultraviolet-visible (UV-Vis) absorption spectrum of neat Alq₃. As can be seen from **figure 4.3**, the results show a clear correlation between the rate of loss in I_{dark} and Alq₃ absorption, as expected.

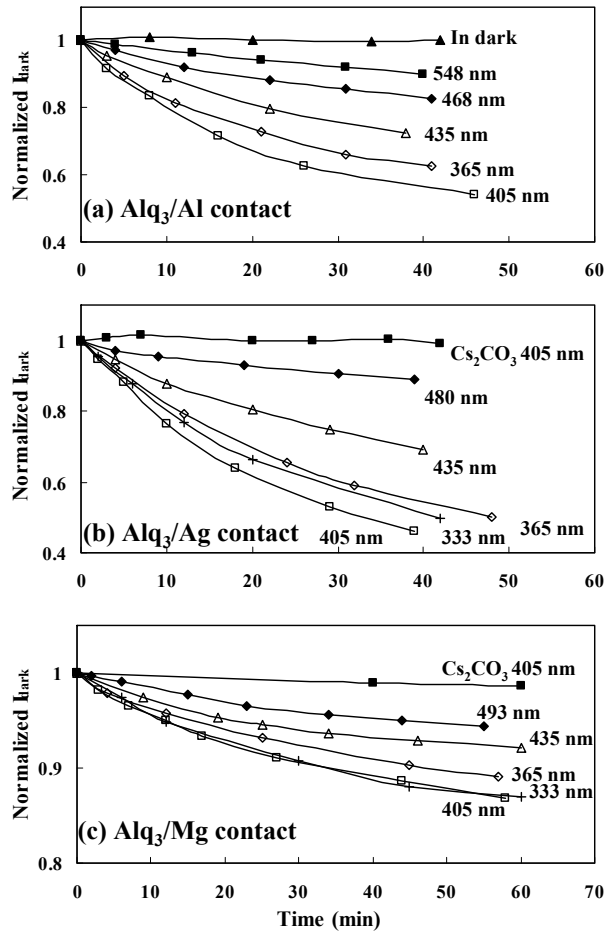


Figure 4.2: Normalized I_{dark} versus irradiation time in samples of structure (a) ITO/Alq₃(60nm)/Al(100nm), (b) ITO/Alq₃(60nm)/Ag(100nm) and (c) ITO/Alq₃(60nm)/Mg(50nm)/Ag(50nm). Monochromatic illumination of various wavelengths at a power density of $\sim 0.35 \text{ mW cm}^{-2}$ is used for irradiation.

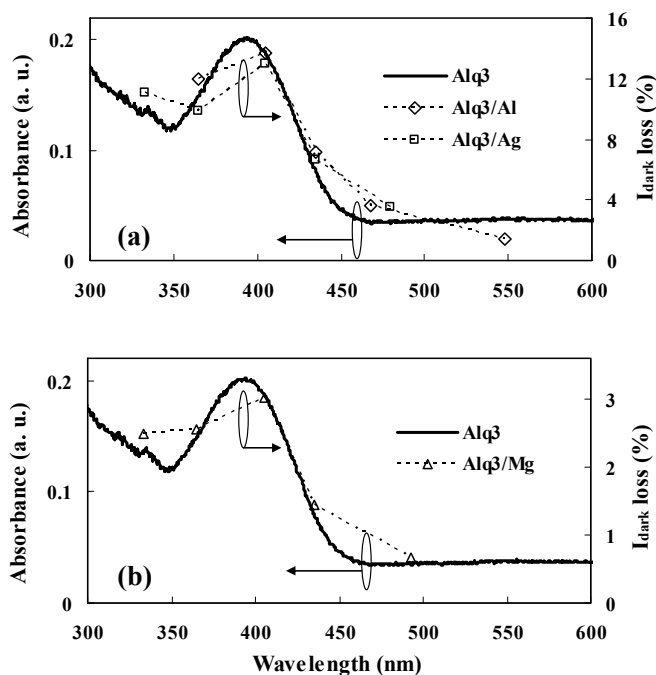


Figure 4.3: Absorption spectrum of neat Alq₃ film and the % loss in I_{dark} in samples of structure (a) ITO/Alq₃(60nm)/Al(100nm), ITO/Alq₃(60nm)/Ag(100nm) and (b) ITO/Alq₃(60nm)/Mg(50nm)/Ag(50nm) after irradiation for a period of 5 minutes at different wavelengths.

Samples containing TPBi or BAQ (instead of AlQ₃) were also studied to investigate if TPBi/metal and BAQ/metal contacts are susceptible to the same photodegradation behavior observed in case of AlQ₃/metal contacts. The general sample structure is ITO/TPBi(60nm)/Metal(100nm) and ITO/BAQ(60nm)/Metal (100nm), respectively, where, as before, the metal is Al, Ag or Mg. Here again, irradiation results in a decrease in I_{dark} , and that the rate of decrease in I_{dark} depends on the irradiation wavelength, and correlates with the UV-Vis absorption spectra of the organic materials. **Figures 4.4(a) and (b)** summarize these results for TPBi and BAQ, respectively. Obviously, these results indicate that the photodegradation behavior occurs in a various organic/metal contacts, suggesting the phenomenon may have a universal presence.

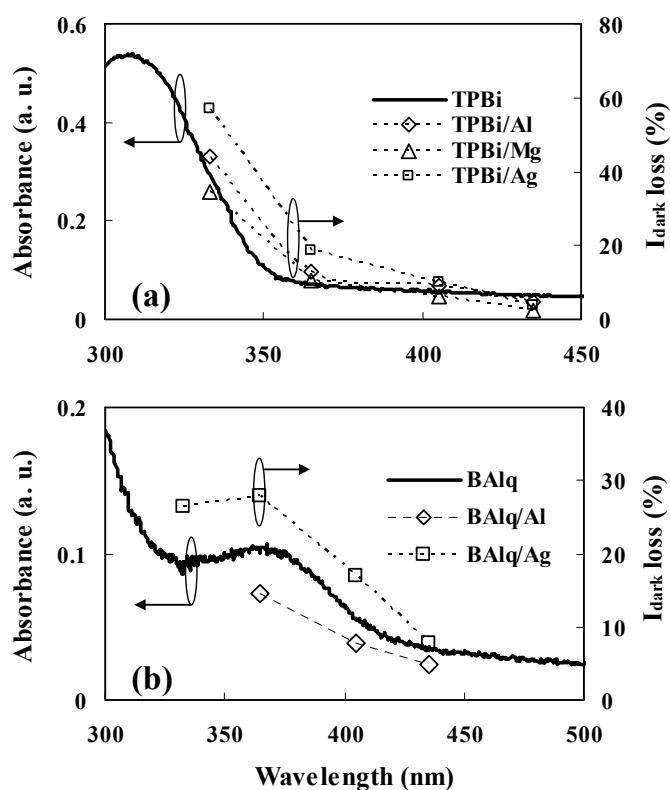


Figure 4.4: Absorption spectra of neat (a) TPBi film, (b) BALq film and the % loss in I_{dark} after irradiation for a period of 5 minutes at different wavelengths.

To find out if the mechanism behind the contact photo-degradation process is chemical in nature, XPS measurements are used to investigate if irradiation results in any changes in the chemical characteristics of the organic/metal contacts. For this, Alq₃/Ag and Alq₃/Al were studied as representative contacts, in consideration of Alq₃ being a very widely used electron-transport material in OLEDs in general, and its contacts with metals being the focus of several XPS studies before.^{42,43,44,45}

Figure 4.5(a) shows the Ag 3d electron binding energy spectra obtained from samples consisting of ITO/Ag(10nm)/Alq₃(10nm). One of the samples has been exposed to 365 nm irradiation at a power density of $\sim 0.5 \text{ mW cm}^{-2}$ for 10 hours in a N₂ atmosphere whereas the other (control) has been kept in the dark (and also in N₂) for the same span of time. It should be pointed out that each sample contained an additional thick Ag protective layer ($\sim 100 \text{ nm}$) covering the Alq₃ to protect it from any possible photo-oxidation due to the presence of any trace amounts of oxygen in the environment

during the irradiation time.⁴⁶ Therefore, the irradiation by the 365 nm illumination was done from the ITO side through the thin (10 nm), semi-transparent silver layer. The top thick silver layer was peeled off by an adhesive tape immediately before the XPS measurements. As can be seen from figure 4.5(a), a spectral shift in binding energy is observed. The shift corresponds to a decrease in a band with a peak at ~368.5 eV and an increase in a band with a peak at ~367.9 eV, suggesting irradiation causes a chemical change at the Ag/Alq₃ contact. As the peak of the elemental Ag 3*d* electrons is at 368.2 ± 0.1 eV,⁴⁷ the bands whose peaks are at 367.9 eV and 368.5 eV must correspond to other chemical species that contain non-elemental Ag. Since the total amount of silver should not change during sample irradiation, the decrease in the 368.5 eV band can be attributed to a species that is initially present at the Ag/Alq₃ contact but gradually decreases as a result of irradiation. In contrast, the increase in the 367.9 eV band can be attributed to another chemical species with a concentration that gradually increases with irradiation. According to literature, binding energy values for Ag 3*d* electrons of 368.5 eV and 367.9 eV are typical for silver-organic complexes and silver oxides (AgO and Ag₂O), respectively.^{48,49,50} Given the fact that the formation of organic-metal complexes at organic/metal contacts usually facilitates charge injection, whereas the formation of the less conductive metal oxides generally hinders it, it is expected that the decrease in *I*_{dark} with irradiation may be associated with a possible reduction in some Ag-Alq₃ complex (as suggested by the decrease in the 368.5 eV band) and the increase in oxide species (as suggested by the increase in the 367.9 eV band). In order to verify if the 367.9 eV band can indeed correspond to silver oxide, XPS scans on Ag films only (i.e. without any organic layers) deposited on glass substrates were conducted. Figure 4.5(b) shows the Ag 3*d* spectrum from an Ag film that has been exposed to air prior to the XPS test, and hence expected to have a thin native oxide layer on the surface, and another spectrum from the same film after a brief sputtering period (Ar ions) to remove the native oxide layer, hence expose the elemental silver. The difference between the two spectra, also shown in figure 4.5(b), corresponds to a band with a peak at exactly 367.9 eV, corresponding to the silver oxide. These results therefore show that the phenomena behind the photo-induced degradation of the Alq₃/Ag contact, and the subsequent deterioration of charge injection, are chemical (i.e. photochemical) in nature, possibly involving the formation of an oxide at the interface.

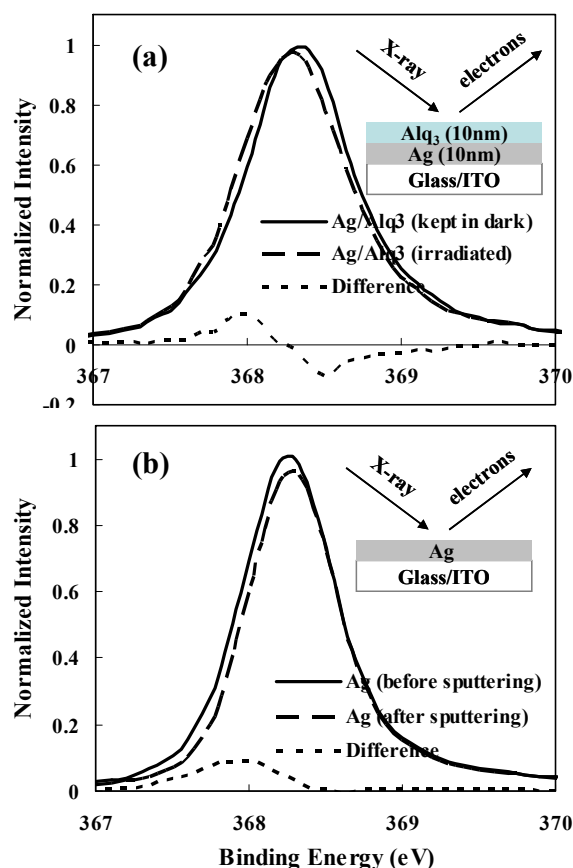


Figure 4.5: (a) Ag 3d electron binding energy spectra from samples of structure ITO/Ag(10nm)/Alq₃(10nm). A 365 nm illumination at a power density of $\sim 0.5 \text{ mW cm}^{-2}$ is used for irradiation for a period of 10 hours. (b) Ag 3d electron binding energy spectra from an Ag film that has been exposed to air prior to the XPS test.

Similarly, XPS was utilized to study photo-induced changes at the Al/Alq₃ contact using samples of structure ITO/Al(10nm)/Alq₃(10nm). **Figure 4.6(a)** shows the binding energy spectra of Al 2p electrons collected from a sample that has been exposed to 365 nm irradiation at a power density of $\sim 0.5 \text{ mW cm}^{-2}$ for 10 hours in a N₂ atmosphere and from a control sample that has been kept in the dark for the same span of time. In these spectra, the band with peak at 72.9 eV corresponds to elemental Al 2p electrons whereas the band with peak at 75.3 eV corresponds to a Al-Alq₃ complex bond (note: the binding energy of Al 2p electrons from the 8-hydroxyquinoline aluminum bond in Alq₃ is 74.6 eV).⁵¹ As can be seen from the figure, irradiation results in a decrease in the 75.3 eV band relative to the 72.9 eV band, revealing a photo-induced change in the chemical characteristics of

the Al/Alq₃ contact, likely associated with changes in the concentration of the Al-Alq₃ complex species. Clearly, here again the results show that the photodegradation mechanism of the Al contact also is photochemical in nature. However, as interfaces produced by the deposition of an organic material on a metal (i.e. metal/organic contact) can be different from those produced by the deposition of a metal on an organic material (i.e. organic/metal contact),⁵² it is reasonable to wonder if the photo-induced changes observed from XPS (i.e. using samples containing metal/organic contacts) can closely represent phenomena in organic/metal contacts. Therefore, photochemical changes in Alq₃/Al contacts were also investigated. Figure 4.6(b) shows the Al 2p spectra of samples with the structure ITO/Alq₃(10nm)/Al(5nm). The thin layer of aluminum is chosen to enable the X-ray to reach the Alq₃/Al contact without the need for sputtering. As the figure shows, here again irradiation results in a decrease in the intensity of the bond of Al-Alq₃ complex, showing that the photochemical changes are essentially the same in both organic/metal and metal/organic contacts.

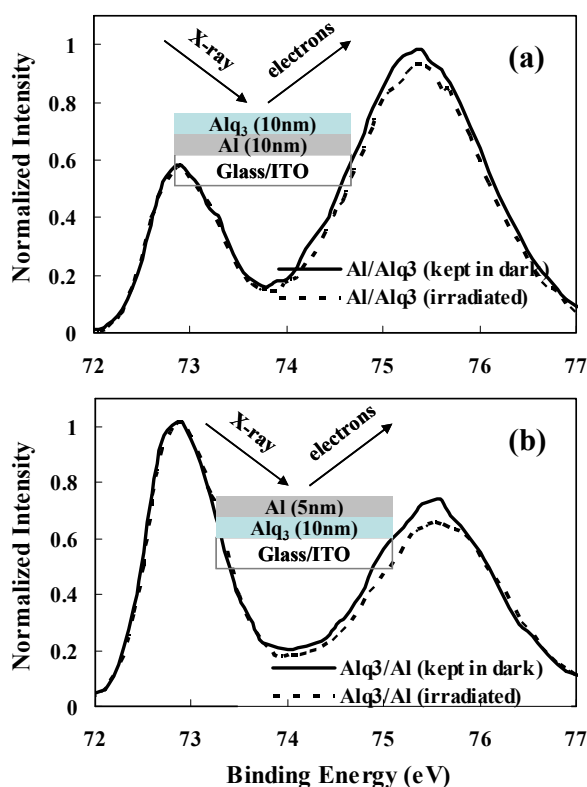


Figure 4.6: (a) Al 2p electron binding energy spectra from samples of structure ITO/Al(10nm)/Alq₃(10nm). (b) Al 2p electron binding energy spectra from samples of structure ITO/Alq₃(10nm)/Al(5nm).

ITO/Alq₃(10nm)/Al(5nm). A 365 nm illumination at a power density of ~0.5 mW cm⁻² is used for irradiation for a period of 10 hours.

As the XPS results suggest a decrease in the organic-metal bonds as a result of irradiation, it is natural to question if the organic/metal interfacial adhesion is also consequently reduced. Therefore, a four-point-bending adhesion tester was used to characterize the critical interfacial fracture strength between the metal and the organic layer following the experimental procedures described by Barakat *et al.*⁵³ For these measurements, test samples consisting of glass substrate Glass(1)/Alq₃(100nm)/Metal(100nm)/Glass(2) are used. The Alq₃ and metal layers (100 nm each) are thermally deposited on glass 1, and then glass 2 is bonded to the metal surface using epoxy glue. A pre-notch is made in glass 1 using a diamond saw. Schematic drawings of a typical adhesion sample stack and the four-point-bend loading configuration are shown in **figure 4.7(a)**. During the adhesion experiments, a normal load is applied on the sample at a constant displacement rate of 2500 nm s⁻¹ while the load and displacement information are recorded. The gradual increase in stress in the sample initiates a crack at the tip of the notch in glass 1. The crack will first penetrate into the stack until reaching the weakest interface in the stack, which, in this case, is the Alq₃/metal interface,⁵⁴ and then propagate along the Alq₃/metal interface. Figure 4.7(b) shows a typical load vs. displacement characteristics of a sample. The sudden drop in load in figure 4.7(b) points to the displacement at which the crack reaches the organic/metal interface and starts to propagate along the interface. As the crack can propagate along the interface with little resistance (due to the generally poor adhesion of organic/metal contacts), a plateau in the curve is observed. The critical energy-release-rate (G_c) or the interfacial adhesion strength is expressed as:

$$G_c = \frac{21(1-\nu^2)P^2 l^2}{16 E b^2 h^3} \quad (1)$$

where ν is the Poisson's ratio of the glass substrate, E is the elastic modulus of the substrate, P is the total force exerted onto the sample that initiates critical interfacial fracture, b is the width of the sample, h is the substrate thickness, and l is the distance between the inner and the outer pins.^{55,56} A greater G_c value corresponds to a stronger interface. **Figures 4.8(a)** and **(b)** display the energy release rate in case of Alq₃/Ag and Alq₃/Al contacts, respectively, comparing in each case, results from samples kept in the dark and from others that have been exposed to 365 nm irradiation at a power density of ~0.5 mW cm⁻² for 10 hours. As expected, the energy release rate of both Alq₃/Ag and Alq₃/Al contacts is found to be lower in the irradiated samples, revealing that organic/metal contact

adhesion indeed deteriorates as a result of irradiation. The results convincingly prove that irradiation results in a decrease in interfacial metal-organic bonding, as was suggested by the XPS measurements above. The decrease in these interfacial metal-organic complex species and the formation of some metal oxide can be behind the deterioration in charge injection characteristics of the contact with irradiation.

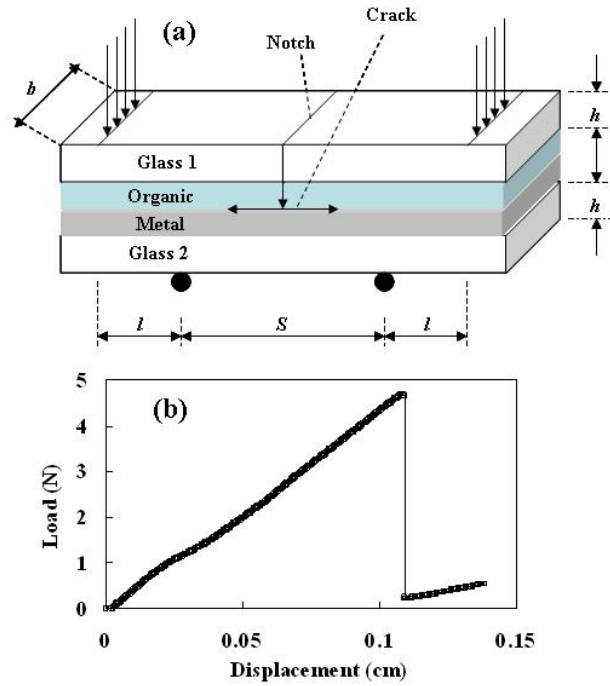


Figure 4.7: (a) Schematic of a four-point flexure specimen for adhesion measurement. (b) A typical load versus displacement characteristics.

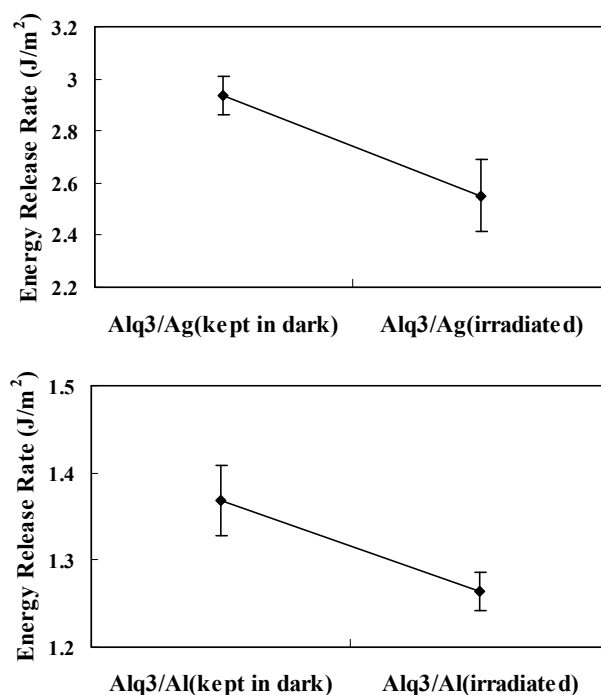


Figure 4.8: Energy release rate of (a) Alq₃/Ag and (b) Alq₃/Al contacts before and after 365 nm irradiation at a power density of $\sim 0.5 \text{ mW cm}^{-2}$ for a period of 10 hours.

In conclusion, irradiation by light in the visible and UV range is found to result in a gradual deterioration in the electrical properties in a number of organic/metal contacts commonly used in organic optoelectronic devices. This photo-induced contact degradation reduces both charge injection (i.e. from the metal to the organic layer) and charge extraction (i.e. from the organic layer to the metal). XPS measurements reveal detectable changes in the interface characteristics after irradiation, indicating that the photo-degradation is chemical in nature. Changes in XPS characteristics after irradiation suggests a possible reduction in bonds associated with organic-metal complexes. Measurements of interfacial adhesion strength reveal a decrease in organic/metal adhesion in irradiated samples, consistent with a decrease in metal-organic bond density. The results shed the light on a new material degradation mechanism that appears to have a wide presence in organic/metal interfaces in general, and which likely plays a key role in limiting the stability of various organic optoelectronic devices such as OLEDs, OSCs and OPDs.

4.2 Investigating the Correlation between Interfacial Degradation vs. Energy-Level Offset at Organic/Metal Interfaces

The material presented in this section was published in *SPIE Organic Photonics+ Electronics*, 882920-882920-9 (2013). It is reproduced here with the permission from the publisher.

Prolonged exposure to irradiation in the ultraviolet (UV)-visible range is found to result in a gradual deterioration in charge carrier transport across these interfaces. Such interfacial degradation behavior is verified to be photochemical in nature. Since organic/metal interfacial degradation is essentially induced by excitons in the vicinity of organic/metal interfaces, it follows that the degradation rate of any given organic/metal interfaces must be strongly dependent on the absorption spectra of corresponding organic materials used at the interfaces. However, there is still a need to explain additional observations such as why organic/metal interfaces containing the same organic material but different metals may degrade differently even under irradiations of the same wavelength and power density (i.e. the same density of photo-generated exciton in organic materials). Furthermore, despite the fact that the use of thin inorganic interfacial layers can significantly improve the organic/metal interfacial stability, the reason behind such phenomenon remains unknown. It is therefore worthwhile to investigate the role of metals and interfacial layers in organic/metal interfacial degradation.

Electron-only (e-only) devices of structure ITO(120nm)/ETM(60nm)/Metal(100nm) were first fabricated and tested, as shown in figure 4.9(a). In these devices, TPBi, AlQ₃ and BAQ are used as the ETM, respectively, and Ag, Al and Mg are used as metal, respectively, due to their widespread presence in OLEDs and other organic optoelectronic devices. When under a forward bias (i.e. ITO is positively biased relative to metal), these devices show e-only transport characteristics. Since the degradation of organic/metal interfaces when subjected to irradiation is essentially induced by excitons created in their vicinity and in general the ETMs absorb more significantly in the UV region than in the visible/infrared region, as evident in their absorption spectra in figure 4.9(b), it is convenient to use UV to irradiate the organic/metal interfaces of these devices. As these e-only devices do not emit light, changes in current at a constant driving voltage were used as an indicator of device organic/metal interfacial degradation due to UV irradiation.

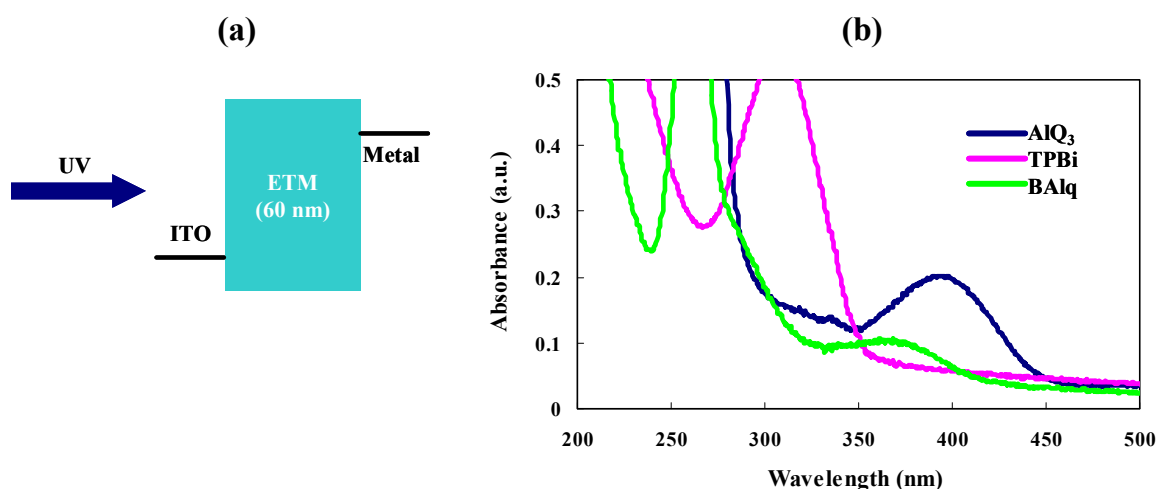


Figure 4.9: (a) E-only device of structure ITO(120nm)/ETM(60nm)/Metal(100nm) under UV irradiation, where the ETM is TPBi, AlQ₃ or BAQ, and the metal is Ag, Al or Mg. (b) Absorption spectra of TPBi, AlQ₃ and BAQ.

Figure 4.10(a) shows the changes in electron current (normalized to the initial current level at time zero) under a constant forward bias of 3 V, 5 V, 11 V and 17 V in TPBi based e-only devices containing Li-acac/Al, Mg, Al and Ag, respectively, as metal contacts versus time during which the devices are exposed to 333 nm illumination at a power density of $\sim 0.3 \text{ mW/cm}^2$. The devices are not electrically biased during the irradiation. As the figure shows, the current in case of Mg, Al and Ag based devices has decreased significantly, from 20 % in case of Mg based one to 60 % in case of Ag based one, in 10 to 15 minutes, whereas that in case of the device with a Li-acac interfacial layer ($\sim 0.5 \text{ nm}$ thick) has decreased only less than 3 % in the same period. As the most obvious difference among these four devices is whether or not a Li-acac interfacial layer is present between the TPBi layer and the metal cathode, it follows that the underlying changes that lead to much faster decrease in current in case of the devices without the Li-acac layer in figure 4.10(a) must be occurring at the TPBi/metal interfaces, which is expected to happen and due to exciton-induced degradation of organic/metal interfaces. Most remarkably, in this figure, the rate of the decrease in current of the devices without the Li-acac layer is quite different, where the Ag based device shows the fastest decrease in current and the Mg based one shows the slowest, even though these devices are subjected to the same irradiation condition. Similar study in which the same e-only devices are subjected to 365 nm illumination at a power density of $\sim 0.5 \text{ mW/cm}^2$ were also conducted. As figure 4.10(b) shows, among the devices without the Li-acac interfacial layer, again, the Ag based one shows the

fastest decrease in current whereas the Mg based one shows the slowest, under the same 365 nm irradiation in the tests, which is essentially consistent with the trend in figure 4.10(a). Therefore, the results in figures 4.10(a) and (b) clearly suggest that metal contacts play a significant role in exciton-induced degradation of organic/metal interfaces.

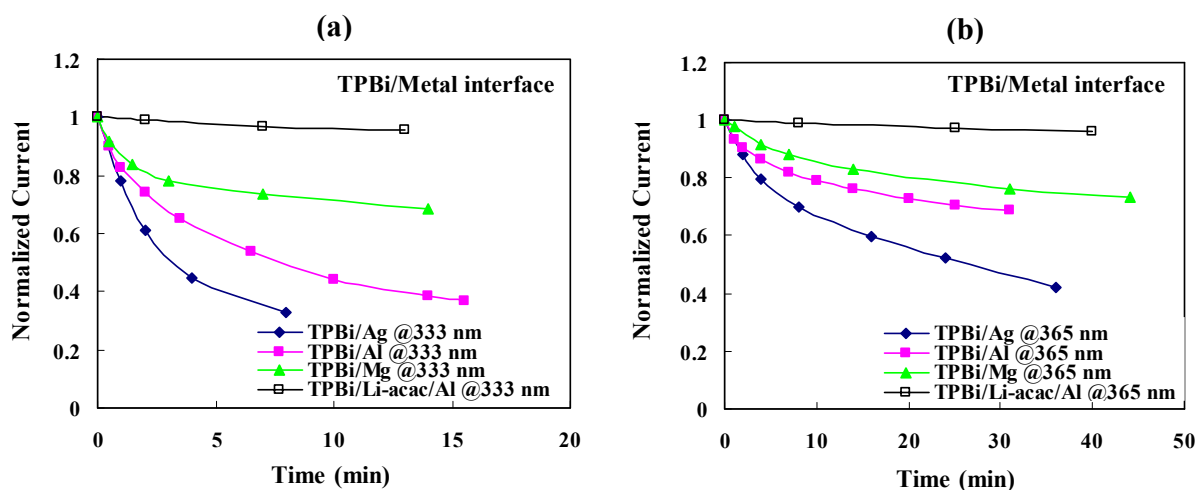


Figure 4.10: Changes in electron current (normalized to the initial current level at time zero) under a constant forward bias of TPBi based e-only devices containing different metal contacts versus time during which the devices are exposed to (a) 333 nm illumination at a power density of ~0.3 mW/cm² and (b) 365 nm illumination at a power density of ~0.5 mW/cm².

Given the different exciton-induced degradation behaviors of TPBi/metal interfaces in figure 4.10, it is natural to wonder if this is due to the different work functions of the metals (i.e. Ag, Al and Mg) used at the interfaces. To test for this, the trend of the current loss due to UV irradiation in TPBi based e-only devices was compared with different metal contacts to that of the work functions of the metals present at the interfaces. Figure 4.11(a) shows the current loss (i.e. left y-axis) due to exposure to 333 nm and 365 nm irradiations for periods of 10 minutes and 30 minutes, respectively, in case of TPBi e-only devices with different metal contacts and the work functions of the corresponding metals (i.e. right y-axis). The work function of Ag, Al and Mg is 4.28, 3.74 and 3.46, respectively.⁵⁷ As the figure shows, a clear correlation between the current loss in TPBi devices and the work functions of the metals used in these devices can be found, indicating that the use of metals of low work functions (e.g. Mg) improves the photo-stability of TPBi/metal interfaces whereas the use of metals of high work functions (e.g. Ag) deteriorates the photo-stability of TPBi/metal interfaces. The results in

figure 4.10(a) therefore prove that the exciton-induced degradation of TPBi/metal interfaces is indeed highly related to the work function of the metals used.

Inspired by the correlation in figure 4.11(a), it is wondered whether the current loss behavior in TPBi e-only device with the Li-acac interfacial layer will also fit into this correlation, especially given the fact that elemental Li will be released from Li-acac when a thick metal contact is subsequently deposited onto the thin Li-acac layer⁵¹ and the work function of elemental Li is quite low (~2.39 eV) as compared to that of metals such as Ag, Al and Mg. Figure 4.11(b) shows the current loss in case of the four TPBi based e-only devices (i.e. including the one with the Li-acac layer) and the work functions of the metals used. Clearly, the device with the Li-acac layer fit quite consistently into the correlation, suggesting that the role of inorganic interfacial layers containing alkali metals (e.g. LiF and Li-acac) in significantly improving the photo-stability of organic/metal interfaces primarily stems from the extremely low work function of the alkali metals.

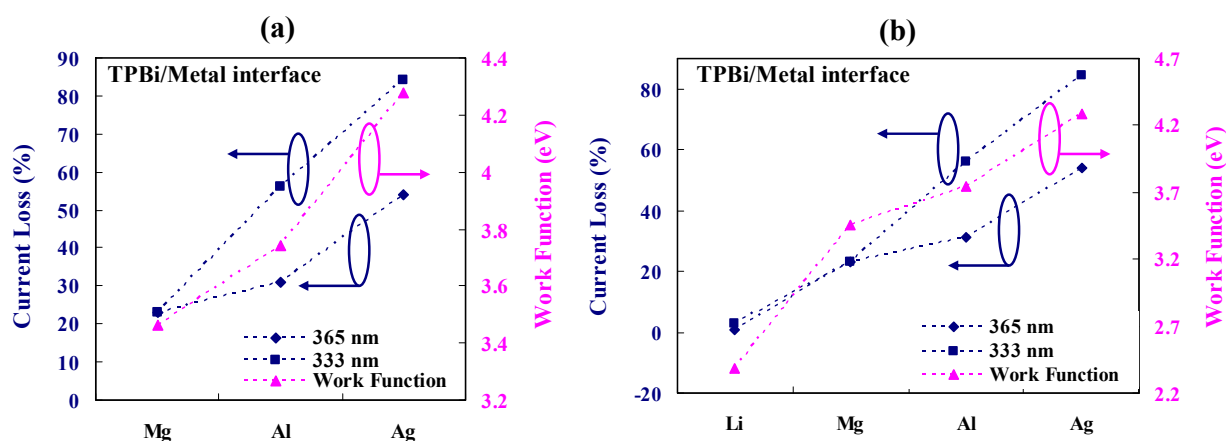


Figure 4.11: (a) Current loss (i.e. left y-axis) due to exposure to 333 nm and 365 nm irradiations for periods of 10 minutes and 30 minutes, respectively, in case of TPBi e-only devices with Ag, Al and Mg contacts and the work functions of the corresponding metals (i.e. right y-axis). (b) Current loss in TPBi e-only devices with Ag, Al, Mg and Li-acac/Al contacts and the work functions of Ag, Al, Mg and Li.

Since the work function of the metal at organic/metal interfaces is indicative of the electron-injection capability from the metal to the LUMO level of the organic layer, it is wondered if the exciton-induced degradation of organic/metal interfaces may be also correlated with the energy barrier for electron injection at these interfaces. Figure 4.12(a) shows the current-voltage

characteristics of TPBi based e-only devices with different metal contacts. As can be seen in the figure, the turn-on voltage ($V_{\text{turn-on}}$) of the devices with Mg, Al and Ag contacts is 3.2 V, 6.6 V and 11.6 V, respectively. Figure 4.12(b) shows the current loss (i.e. left y-axis) due to exposure to 333 nm and 365 nm irradiations for periods of 10 minutes and 30 minutes, respectively, and the $V_{\text{turn-on}}$ (i.e. right y-axis) of these devices. Again, as figure 4.12(b) shows, a clear correlation between these two physical quantities is observed. Given the above results and analysis, it may be concluded that the different exciton-induced degradation behaviors of TPBi/metal interfaces may actually be arising from the difference in energy barrier for electron injection at different TPBi/metal interfaces.

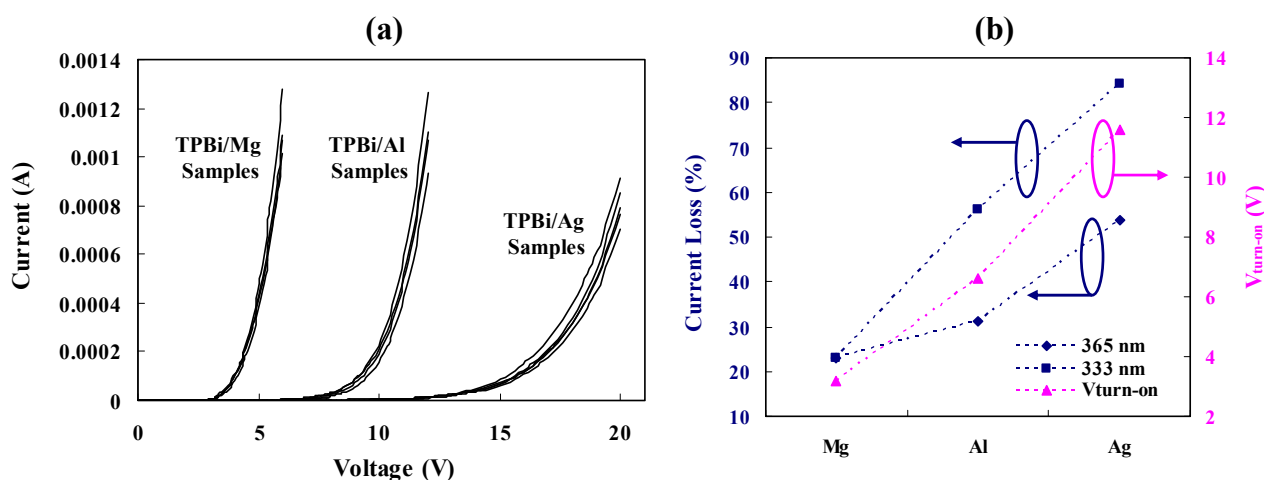


Figure 4.12: (a) Current-voltage characteristics of TPBi based e-only devices with different metal contacts. (b) Current loss (i.e. left y-axis) due to exposure to 333 nm and 365 nm irradiations for periods of 10 minutes and 30 minutes, respectively, and $V_{\text{turn-on}}$ (i.e. right y-axis) of the TPBi based e-only devices.

E-only devices containing AlQ₃ or BAQ (instead of TPBi) were also studied to investigate if similar correlation between exciton-induced degradation of organic/metal interfaces and energy barrier for electron injection at the interfaces is present in case of AlQ₃/metal and BAQ/metal interfaces, as observed in case of TPBi/metal interfaces. The device structure is ITO(120nm)/AlQ₃(60nm)/Metal(100nm) and ITO/BAQ(60nm)/Metal(100nm), respectively, where, as before, the metal is Al, Ag or Mg. Figures 4.13 (a) and (b) show the changes in electron current (normalized to the initial current level at time zero) under a constant forward bias of AlQ₃ based e-only devices containing different metal contacts versus time during which the devices are exposed to 365 nm illumination at a power density of ~0.5 mW/cm² and 405 nm illumination at a power density

of $\sim 0.5 \text{ mW/cm}^2$, respectively. Here again, the rate of the decrease in current of these devices is significantly different, despite the same irradiation condition used in each set of tests. Figure 4.13(c) shows the current loss (i.e. left y-axis) due to exposure to 365 nm and 405 nm irradiations for a period of 40 minutes of the devices with Ag, Al and Mg contacts and the work functions of these metals (i.e. right y-axis). Again, a clear correlation between the current loss of the devices and the work functions of the metals used can be found. Similar observations are also found to be present in case of BAQ based e-only devices, as shown in figures 4.14(a)-(c). Seeing the above results from TPBi, AlQ₃ and BAQ based devices, it may therefore be concluded that metal contacts unquestionably play a significant role in exciton-induced degradation of organic/metal interfaces in general, and such interfacial degradation behavior is, to a large extent, highly correlated with the work function of the metal contacts used and the energy barrier for electron injection at organic/metal interfaces.

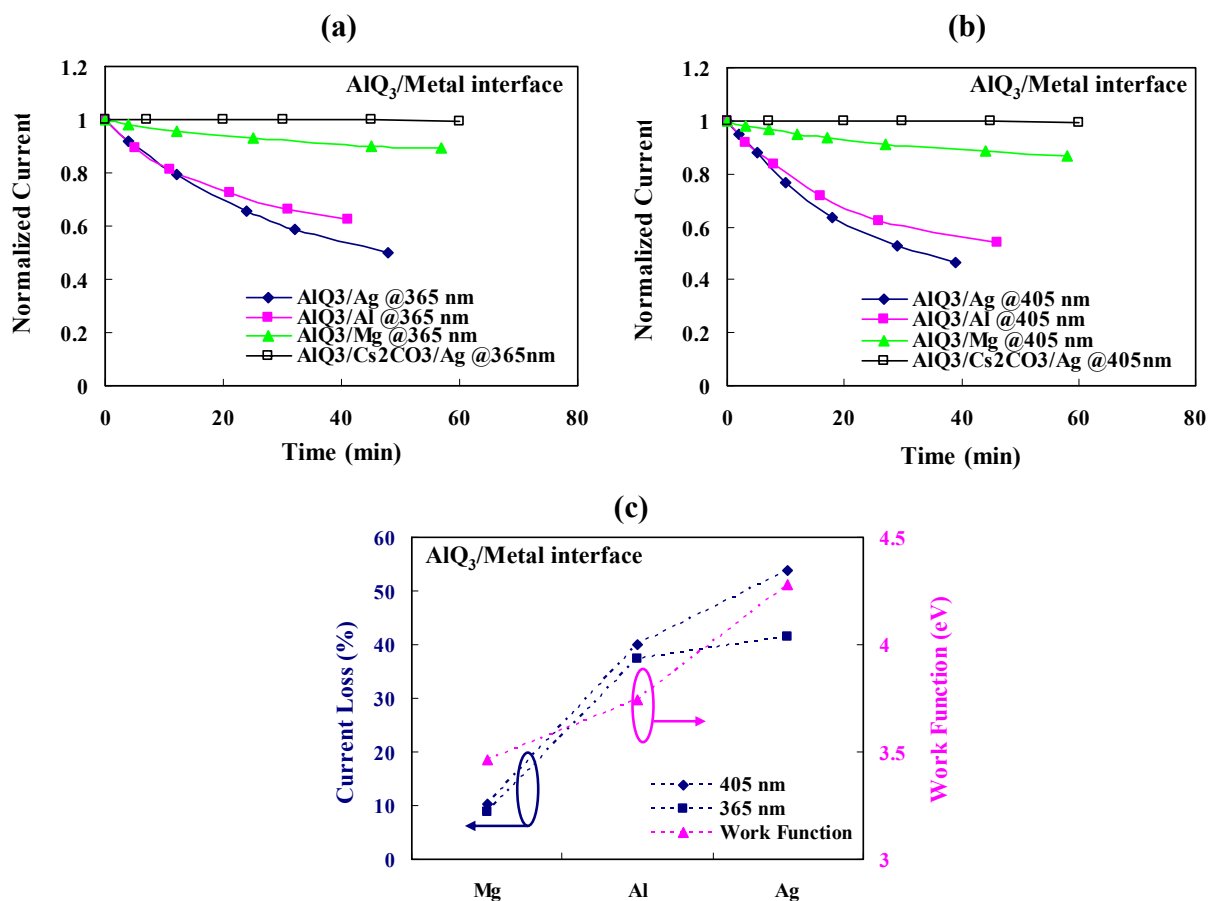


Figure 4.13: Changes in electron current (normalized to the initial current level at time zero) under a constant forward bias of AlQ₃ based e-only devices containing different metal contacts versus time during which the devices are exposed to (a) 365 nm illumination at a power density of ~0.5 mW/cm² and (b) 405 nm illumination at a power density of ~0.5 mW/cm². (c) Current loss (i.e. left y-axis) due to exposure to 365 nm and 405 nm irradiations for a period of 40 minutes of the devices with Ag, Al and Mg contacts and the work functions of these metals (i.e. right y-axis).

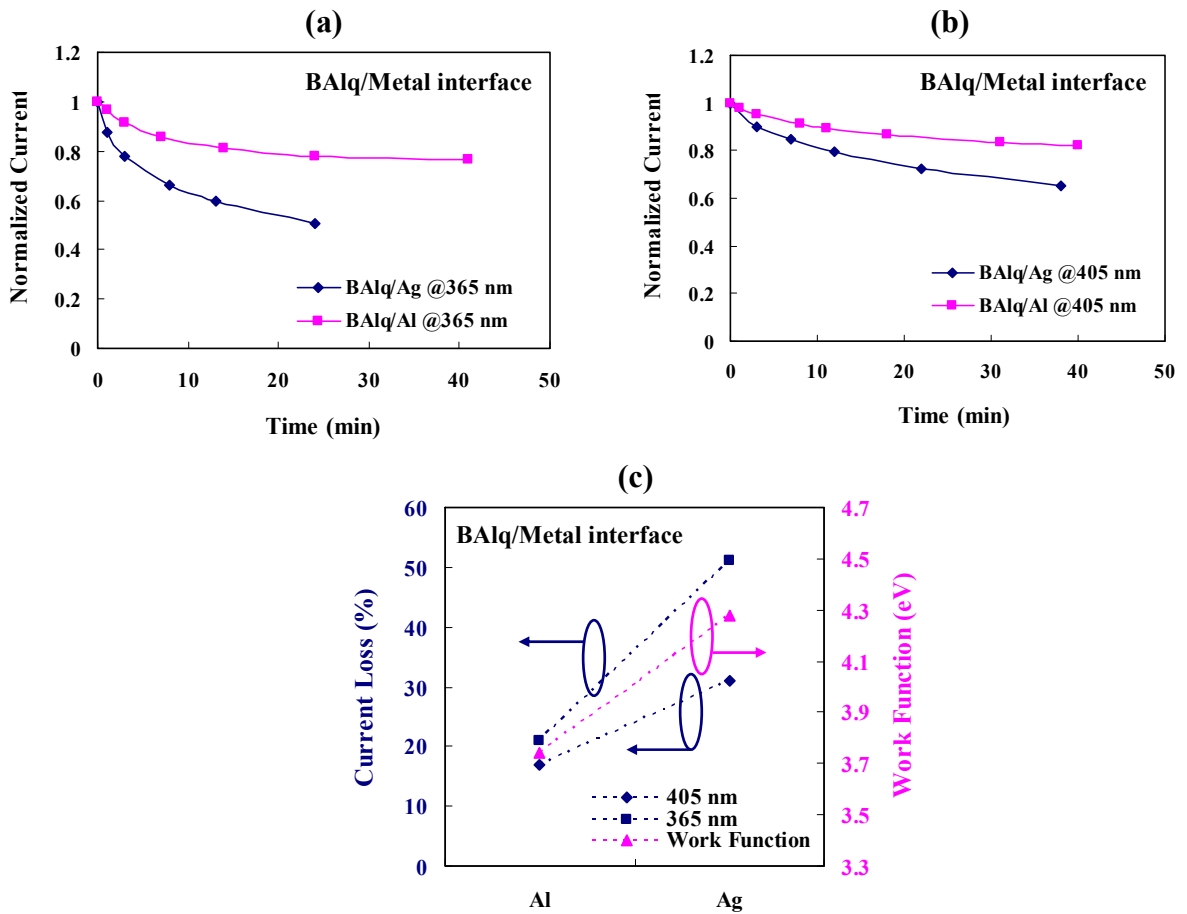


Figure 4.14: Changes in electron current (normalized to the initial current level at time zero) under a constant forward bias of BAQ based e-only devices containing different metal contacts versus time during which the devices are exposed to (a) 365 nm illumination at a power density of ~0.5 mW/cm² and (b) 405 nm illumination at a power density of ~0.5 mW/cm². (c) Current loss (i.e. left y-axis) due to exposure to 365 nm and 405 nm irradiations for a period of 40

minutes of the devices with Ag and Al contacts and the work functions of these metals (i.e. right y-axis).

Observing a clear correlation between exciton-induced degradation of organic/metal interfaces and energy barrier for electron injection at organic/metal interfaces in a range of organic/metal systems suggests that the phenomenon may be associated with the chemical and physical characteristics of organic/metal interfaces. Since the vacuum deposition of metals onto organic materials leads to the formation of organometallic bonds at organic/metal interfaces, one possible reason behind such correlation may be the difference in the strength of these interfacial metal-organic bonds. For example, in case of organic/metal interfaces with low work function metals (including elemental alkali metals such as Li and Cs that can be released from interfacial layers by the subsequent deposition of thick metal contacts), the metals can easily react with the underlying organic materials to form strong chemical bonds. These bonds could be sufficiently stable and thus robust to exciton-induced degradation, leading to the formation of photo-stable organic/metal interfaces. However, in case of organic/metal interfaces with high work function metals (e.g. Ag), the metals may not react chemically with the underlying organic materials, or form only weak bonds. These weak organometallic bonds may be very susceptible to exciton-induced degradation, leading to fast degradation of organic/metal interfaces under UV irradiation.

Another possible reason that contributes to the observed correlation may arise from the difference in band bending of organic materials at organic/metal interfaces with metals of different work functions, which is illustrated in the band diagrams in figure 4.15. As figure 4.15(a) shows, in case of organic/metal interfaces with metals of work functions lower than the Fermi energy level of the ETM, electrons will spontaneously migrate from the metal to the ETM due to the difference in Fermi energy level at the ETM/metal interface, which leads to an obvious band bending of the ETM in the vicinity of the interface. The occurrence of the band bending, which is also indicative of the presence of a high concentration of electrons at the ETM/metal interface, suggests that the lifetime of excitons formed at the ETM/metal interface will become shorter due to the efficient quenching of excitons by the high density electrons nearby. As a result, the exciton-induced degradation of the ETM/metal interface will be reduced. On the other hand, in case of organic/metal interfaces with metals of work functions higher than the Fermi energy level of the ETM, as figure 4.15(b) shows, the number of electrons that spontaneously migrate from the ETM to the metal due to the difference in Fermi energy level at the ETM/metal interface may be relatively small due to the extremely low

concentration of free electrons created in organic semiconductor materials at room temperature, which leads to a very insignificant band bending of the ETM at the interface. As a result, the lifetime of excitons formed at the ETM/metal interface will not be reduced and the exciton-induced degradation of the ETM/metal interface will thus be significant.

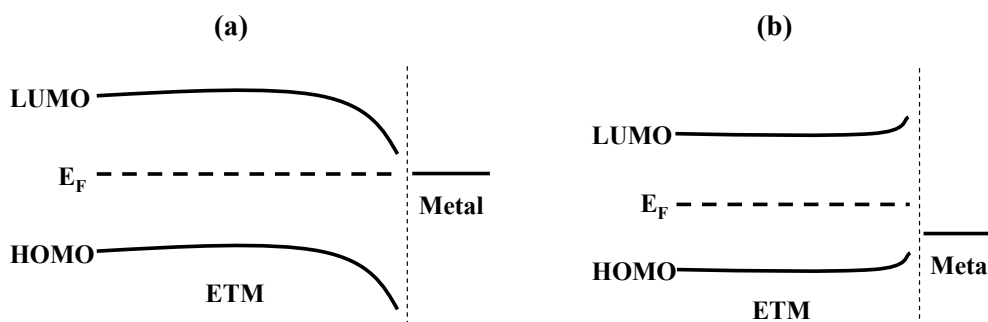


Figure 4.15: Band diagrams for organic/metal interfaces with metals of work functions (a) lower and (b) higher than the Fermi energy level of the ETM.

In conclusion, exciton-induced degradation of various organic/metal interfaces in organic optoelectronic devices was studied. The results show that organic/metal interfaces are susceptible to irradiation in general, resulting in a deterioration in charge transport across the interfaces. Interestingly, it is found that organic/metal interfaces containing the same organic material but different metals degrade quite differently, where interfaces with metals of high work functions tend to be more susceptible to exciton-induced degradation than those with metals of low work functions under the same irradiation condition. The results suggest a clear correlation between exciton-induced degradation of organic/metal interfaces and energy barrier for electron injection at organic/metal interfaces. Furthermore, the fact that the use of interfacial layers, which usually contain alkali metals of extremely low work function, can greatly improve organic/metal interfacial photo-stability is also, to a large extent, consistent with such correlation. The reason behind such correlation may stem from the difference in the strength of organic-metal bonds formed at different organic/metal interfaces and/or the difference in band bending of organic materials in the vicinity of organic/metal interfaces due to the use of metals of different work functions at the interfaces.

4.3 Identifying the Role of Interfacial Layers in Improving Device Stability

The material presented in this section was published in *SPIE Organic Photonics+ Electronics*, 84760D-84760D-5 (2012). It is reproduced here with the permission from the publisher.

Seeing that organic/metal interfaces are susceptible to exciton-induced degradation and the use of interfacial layers can reduce such degradation, it is natural to wonder if this degradation mechanism plays a role in OLEDs degradation and the typically better stability of devices containing interfacial layers essentially originates from the suppression in the exciton-induced degradation of organic/metal interfaces.

First OLEDs with the general structure of ITO(120nm)/NPB(70nm)/Alq₃(70nm)/Cathode were fabricated and tested, shown in figure 4.16(a). In these OLEDs, Mg:Ag (9:1 in volume, 100nm) and Al (100nm) are used as metal cathode, and Cs₂CO₃ (1 nm) is used as the interfacial layer. Figure 4.16(b) shows the changes in device EL (presented in the form of normalized EL) and driving voltage (V_d) at a current density of 50 mA/cm² as a function of time from OLEDs with the cathode of Mg:Ag, Cs₂CO₃/Mg:Ag and Cs₂CO₃/Al. The initial brightness of these devices is 1200~1300 cd/m². As the figure shows, the increase in V_d under continuous electrical driving in devices with Mg:Ag is much bigger than that in case of the devices with Cs₂CO₃/Mg:Ag and Cs₂CO₃/Al. Meanwhile, device with Mg:Ag shows much low EL lifetime as compared to devices with Cs₂CO₃/Mg:Ag and Cs₂CO₃/Al. Given the fact that the initial brightness and V_d of these devices are comparable in magnitude, the electron-hole balance of these devices is therefore expected to be similar. Accordingly, EL degradation resulting from the holes accumulation at the NPB/Alq₃ interface is expected to be similar in these devices. Thus, the different trends in EL and V_d stability in figure 4.16(b) must be arising from the difference in the stability of the organic/cathode contacts.

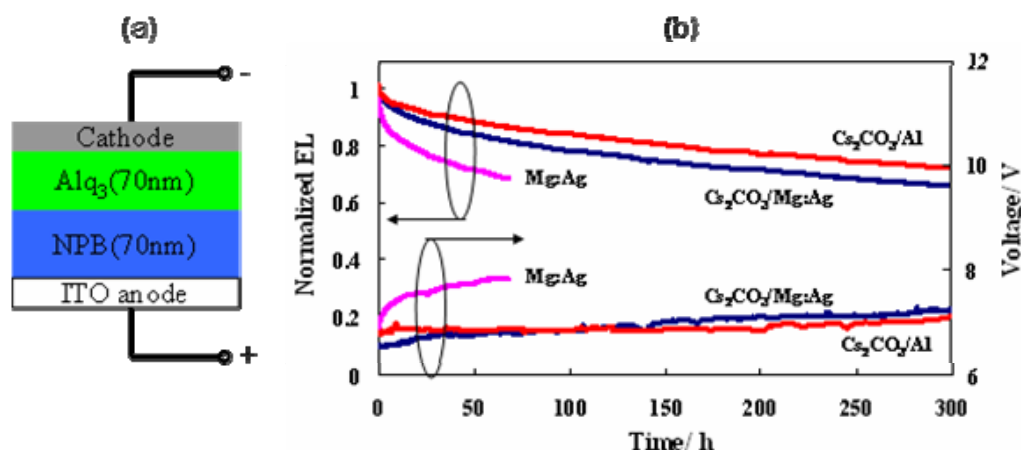


Figure 4.16: (a) OLEDs with the general structure ITO(120nm)/NPB(70nm)/Alq₃(70nm)/Cathode. (b) Changes in EL and V_d at a current density

of 50 mA/cm^2 as a function of time from OLEDs with cathode of Mg:Ag, $\text{Cs}_2\text{CO}_3/\text{Mg:Ag}$ and $\text{Cs}_2\text{CO}_3/\text{Al}$, respectively.

To find out if the difference in the EL and V_d stability of the organic/metal contact is mainly due to the different photo-degradation behaviors of these organic/metal contacts, the photo-stability of these organic/metal contacts was studied. As figure 4.17(a) shows, the general structure of these samples is ITO/ $\text{Alq}_3(70\text{nm})$ /Cathode. In these samples, Mg:Ag (9:1 in volume, 100nm) and Al (100nm) are used as metal cathode, and Cs_2CO_3 (1 nm) is used as the interfacial layer. Figure 4.17(b) shows the changes in V_d at a current density of 20 mA/cm^2 as a function of time during which the samples with the structure of ITO/ $\text{Alq}_3(70\text{nm})$ /Mg:Ag, ITO/ $\text{Alq}_3(70\text{nm})$ / $\text{Cs}_2\text{CO}_3(1\text{nm})$ /Mg:Ag and ITO/ $\text{Alq}_3(70\text{nm})$ / $\text{Cs}_2\text{CO}_3(1\text{nm})$ /Al are irradiated by a 546nm external illumination with the power density of 1.0 mW/cm^2 . As can be seen from the figure, an significant increase in V_d in case of Mg:Ag is found while no detectable change in V_d is observed in similar irradiating time. The increase in V_d induced by external irradiation alone in figure 4.17(b) follows a trend similar to that under electrical driving alone in figure 4.16(b) for any device type. For example, after 60 minutes of irradiation, an increase in V_d of about 0.5V was observed for sample without Cs_2CO_3 buffer layer and nearly 0 V for the samples with Cs_2CO_3 buffer layer, whereas the increase in V_d upon electrical driving for the same period of time is about 0.2 V and nearly 0 V, respectively.

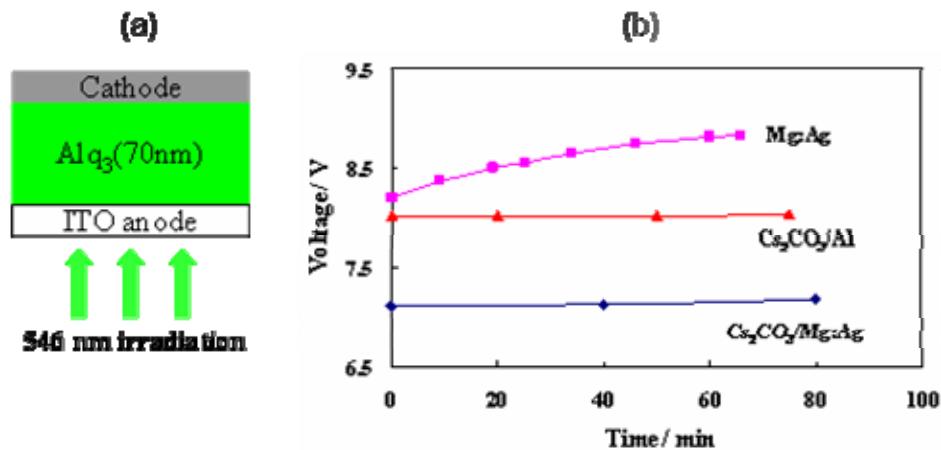


Figure 4.17: (a) Samples with the general structure ITO(120nm)/ $\text{Alq}_3(70\text{nm})$ /Cathode. (b) Changes in V_d at a current density of 20 mA/cm^2 as a function of time during which the samples are irradiated by a 546nm external illumination with the power density of 1.0 mW/cm^2 .

Given that the external coupling efficiency for an ITO-glass substrate and organic layers is ~17%,⁵⁸ the brightness of 1200-1300 cd/m² from the EL of OLEDs in previous electrical aging tests is equivalent to a brightness of ~7000-7600 cd/m² inside the devices. According to the relationship between the luminance and the power density,⁵⁹ the green (530 nm) emission of 7000-7600 cd/m² inside these devices corresponds to an irradiation with an approximate power density of 1.0-1.1 mW/cm², which is quite close to power density 1.0 mW/cm² used in the photo-stability measurements. Therefore, The similar trends in V_d in figure 4.16(b) and 4.17(b) suggest that the increase in device V_d during continuous electrical driving may indeed be at least in part due to the exciton-induced degradation of the organic/metal contact by device own EL, and the increase in device stability by Cs₂CO₃ layers is indeed due to the improvement in the photo-stability of the organic/metal contacts.

In conclusion, irradiation by light is found to result in a gradual deterioration in the electrical properties in the organic/metal contacts commonly used in OLEDs. This photo-induced contact degradation reduces both charge injection (i.e. from the electrodes to the organic layer) and charge extraction (i.e. from the organic layer to the electrodes). It is also found that interfacial layers such as Cs₂CO₃ can greatly improve the photo-stability of the organic/metal contacts, and thus improve the stability of OLEDs.

4.4 Summary

In this chapter, exciton-induced degradation of organic/metal interfaces is investigated. Results show that such degradation leads to a deterioration in both charge injection (i.e. from metal to organic layer) and charge extraction (i.e. from organic layer to metal) across the interfaces. This exciton-induced degradation was found to be photo-chemical in nature, associated with a reduction in bonds between organic molecules and metal atoms. The adhesion strength of organic/metal interfaces after the degradation decreases.

The studies further show that organic/metal interfaces containing the same organic material but different metals degrade differently, where interfaces with metals of high work functions tend to be more susceptible to exciton-induced degradation than those with metals of low work functions. It was found that a clear correlation between exciton-induced degradation of organic/metal interfaces and energy barrier for electron injection at organic/metal interfaces exists. The reason behind such correlation may stem from the difference in the strength of organic-metal bonds formed at different organic/metal interfaces. It was also found that the use of interfacial layers, which usually contain

alkali metals of extremely low work function, can greatly improve organic/metal interfacial photo-stability, and thus improve the stability of OLEDs.

Chapter 5

Exciton-Induced Degradation of ITO/Organic Interfaces

ITO is widely used as a transparent electrical contact in OLEDs due to its high optical transparency, good electrical conductivity and high work function. It is commonly used in the form of a thin film (~ 100 nm thick) that is pre-deposited on a glass substrate via a sputtering process. In this chapter, exciton-induced degradation of ITO/organic interfaces in OLEDs, and the role of ITO surface treatments and interfacial layers in improving device stability will be studied.

5.1 Investigation of Exciton-Induced Degradation of ITO/Organic Interfaces

The material presented in this section was published in *Org. Electron.* **13**, 2075-2082 (2012). It is reproduced here with the permission from the publisher.

Surface treatment of the ITO and/or the use of interfacial layers in-between the ITO and HTL are often required for improving device efficiency and stability. Examples of surface treatments of ITO include chemical treatment by acids or halogens,^{60,36} self-assembled monolayers⁶¹ and plasma treatments. Among these, plasma treatment is particularly popular due to its effectiveness in improving device performance and relative ease of application.^{62,63,64,65,66} Examples of interfacial layers that are often used in-between ITO and organic hole transport materials include copper phthalocyanine, Pt, SiO₂ and MoO₃.^{67,68,69,70} Among these, MoO₃ has recently attracted significant attention, owing to its wide success in enhancing the efficiency and stability of OLEDs.^{71,72} Despite the wide utilization of these techniques for improving device performance, the underlying mechanisms behind their role in enhancing device stability are still not completely understood. In general, the stability improvement effect is usually attributed to the possible role of these contact modification techniques in impeding the diffusion of indium from ITO into the organic semiconductor layers and in suppressing the crystallization of the organic layers.^{62,72}

A study by Heil *et al*⁷³ has shown that ITO/organic interfaces in OLEDs can be susceptible to photo-induced changes when irradiated by sunlight, resulting in a deterioration in the charge injection efficiency from ITO into HTL. However, whether this photo-degradation can be induced by device own EL as may conceivably occur in case of OLEDs, and the possible role of this phenomenon in limiting device stability, has not been investigated. Furthermore, the possible effect of ITO contact

modification, by means of surface treatments or interfacial layers, on interfacial photo-stability has never been studied before. A better understanding of the photo-degradation behavior of the ITO/organic contacts and whether it may be influenced by ITO surface treatments or interfacial layers are therefore still required.

In order to see if the ITO/organic contacts are similarly susceptible to photo-induced changes, the effect of exposure to optical and near UV illumination on a series of OLEDs of the general structure: ITO (120 nm)/NPB (70nm)/Alq₃ (70 nm)/Mg:Ag (100nm) was first studied. In these devices, ITO, NPB, Alq₃ and Mg:Ag function as anode, hole transport layer, electron transport layer and cathode, respectively. Figure 5.1(a) shows the changes in driving voltage (V_d) required to drive a current of density =10 mA cm⁻² in three identical devices, as a function of time, during which these devices are subjected to one of three scenarios: (1) irradiation by 365 nm illumination at a power density of ~0.5 mW cm⁻², (2) irradiation by 546 nm illumination at a power density of ~0.5 mW cm⁻² and (3) kept in the dark. The devices are not subjected to electrical bias during that time. As the figure shows, V_d increases quite significantly in case of the two devices exposed to irradiation but remains essentially unchanged in case of the device kept in the dark. The observations clearly show that the increase in V_d observed in case of the irradiated devices are photo-induced.

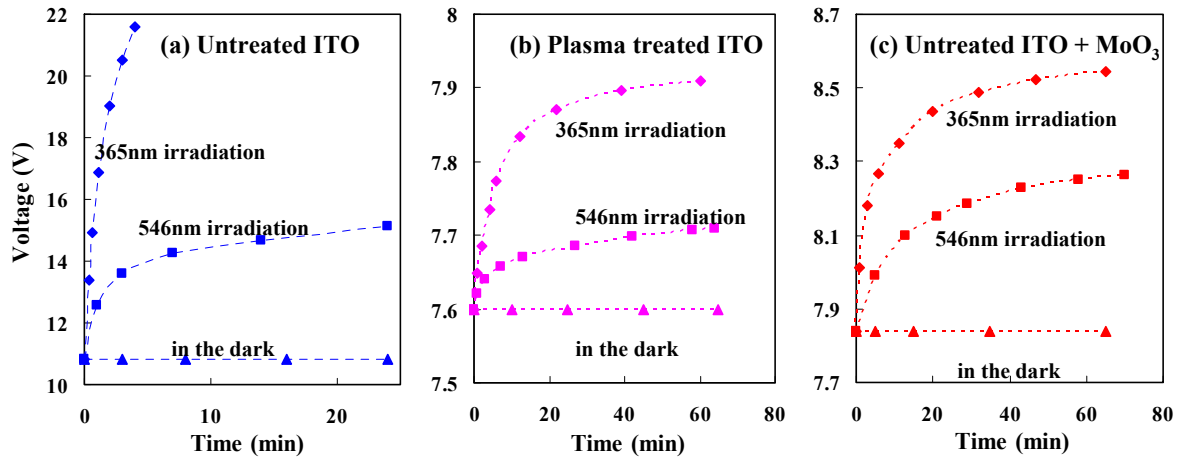


Figure 5.1: V_d at a current density of 10 mA/cm² versus time during which the devices are subjected to exposing to irradiation at 365 nm, at 546 nm or kept in the dark. The structures of these devices are: (a) untreated ITO/NPB(70nm)/Alq₃(70nm)/Mg:Ag(100nm), (b) plasma treated ITO/NPB(70nm)/Alq₃(70nm)/Mg:Ag(100nm), and (c) untreated ITO/MoO₃(1nm)/NPB(70nm)/Alq₃(70nm)/Mg:Ag(100nm)

Figure 5.1(b) shows results from a similar test conducted on a second group of devices which are in all respects identical to the first group, except that in these devices, the ITO is treated by plasma (CF₄/O₂ gas mixture (3:1)) prior to the deposition of the organic layers. As shown in figure 5.1(b), the initial V_d is much lower in this case, due to the known effect of the plasma treatment increasing the ITO work function and thereby decreasing the energy barrier between the ITO anode and the hole transport layer NPB.^{63,64} Here again, the V_d is found to increase quickly in case of the devices exposed to irradiation but remains essentially unchanged in case of the device kept in the dark. More notably, a comparison between the V_d rise trends in figures 5.1(b) versus those in figure 5.1(a) shows that the changes in V_d (represented as ΔV_d , where $\Delta V_d = V_d$ after exposure to illumination for a period t – the initial value of V_d) as a result of irradiation at 365 nm or 546 nm are much smaller in magnitude in case of the second group devices (i.e. in figure 5.1(b)). For example, after 20 minutes of 546 nm irradiation, devices in group 2 exhibit a ΔV_d of only ~ 0.1 V, versus ~ 4 V in case of group 1 devices. Since the only difference between the two groups of devices is at the ITO/organic contact (due to the plasma treatment of the ITO surface in the second group only), it follows that the marked differences in the magnitude of ΔV_d between the two groups must be due to light-induced changes at the ITO/organic interface. The results therefore show that the ITO contact is susceptible to photo-induced changes that bring about a deterioration in its hole injection capacity into the NPB, evident in the resulting increase in the required V_d . These light-induced changes occur more slowly in case of devices with the plasma-treated ITO, revealing that the treatment increases the contact photo-stability.

It has been known that the use of a plasma treatment of the ITO surface prior to depositing organic layers in OLEDs can result in a significant improvement in device stability.⁶² Finding that plasma treatment increases contact photo-stability, as evident from the smaller ΔV_d , it is natural to wonder if the device stability improvement may be the result of the higher photo-stability of the ITO/organic interface. As the introduction of MoO₃ interfacial layers in between the ITO and organic layers is known to also result in an increase in device stability, the question of whether the use of MoO₃ may have a similar effect naturally arises. Hence, a third group of devices that are in all respects identical to the first group of devices was tested, except that in this case, the devices further contained a thin interfacial MoO₃ layer (~ 1 nm thick) in between the ITO and the NPB. (In this case, no plasma treatment is used). The test results on group 3 devices are shown in figure 5.1(c). As expected, the devices have a lower initial V_d in comparison to group 1 devices, due to the enhanced hole injection when using MoO₃. Interestingly, similar to group 2 devices (i.e. devices with plasma-treated ITO), the devices here exhibit a much slower increase in V_d upon continuous irradiation. For

example, after 20 minutes of 546 nm irradiation, devices in group 3 exhibit a ΔV_d of only ~ 0.2 V, versus ~ 4 V in case of group 1 devices. Clearly, the results reveal that, similar to plasma treatment, the use of an interfacial layer of MoO_3 reduces photo-induced changes at the ITO contact, thereby increasing its photo-stability. The results therefore reveal not only that the ITO contact is susceptible to photo-induced deterioration in hole injection upon continuous irradiation, but also that approaches commonly used for improving device stability (e.g. plasma treatment or MoO_3 interfacial layers) slow down this photo-degradation behavior, suggesting that their effectiveness in enhancing device stability may, at least in part, be due to them taking this role.

Since irradiation at 546 nm results in significantly different changes in V_d of devices with various ITO/organic interfaces, it becomes curious if similar effects may be induced by device own emission. Changes in V_d under continuous electrical driving (hence the devices are continuously producing EL) were therefore tested in similar devices, but without any external irradiation. Figure 5.2 shows the changes in device EL (presented in the form of normalized EL, where normalized EL = device EL intensity at any given time / its initial EL Intensity) and V_d at a current density of 20 mA cm^{-2} from devices of the same structure as those described in figure 5.1 (i.e. untreated ITO, plasma-treated ITO, or untreated ITO plus a MoO_3 interfacial layer, and denoted as ITO, PT-ITO and ITO/ MoO_3 , respectively). The initial brightness of these devices is $400\text{-}500 \text{ cd/m}^2$. As the figure shows, the increase in V_d under continuous electrical driving in devices with the untreated ITO is much bigger than that in case of the devices with the PT-ITO or ITO/ MoO_3 . To facilitate comparison, the changes in V_d with time due to external 546 nm irradiation alone, for the three different device types of figure 5.1, are re-plotted in the inset of figure 5.2. As can be seen from the figure, the increase in V_d under electrical driving alone follows a trend similar to that induced by external irradiation alone for any device type. For example, after 30 minutes of electrical driving, an increase in V_d of about 2V, 0.03 V and 0.25 V was observed for the devices with ITO, PT-ITO and ITO/ MoO_3 , respectively, whereas the increase in V_d upon irradiation for the same period of time is about 4 V, 0.08 V and 0.35 V, respectively. Clearly, the device with the untreated ITO, which exhibited the lowest contact photo-stability in the above tests, here also exhibits the lowest stability. As known, since the external coupling efficiency for ITO-glass substrate and organic layers is $\sim 17\%$,⁵⁸ the brightness of $400\text{-}500 \text{ cd m}^{-2}$ from the emitted light of these devices is equivalent to a brightness of $2400\text{-}3000 \text{ cd m}^{-2}$ inside these devices. According to the relationship between the luminance and the power density,⁵⁹ such green (530 nm) emission of $2400\text{-}3000 \text{ cd m}^{-2}$ inside these devices approximately corresponds to an irradiation of power density $0.35\text{-}0.44 \text{ mW cm}^{-2}$, which is quite

close to power density 0.5 mW cm^{-2} used in the above tests. Therefore, the very similar trends suggest that the increase in device V_d during continuous device EL may indeed be caused at least in part by the photo-degradation of the ITO contact. They also further support the conclusion that the increase in device stability attained on using plasma treatment of the ITO or MoO₃ layers is indeed due to the improvement in photo-stability of the ITO/organic contacts.

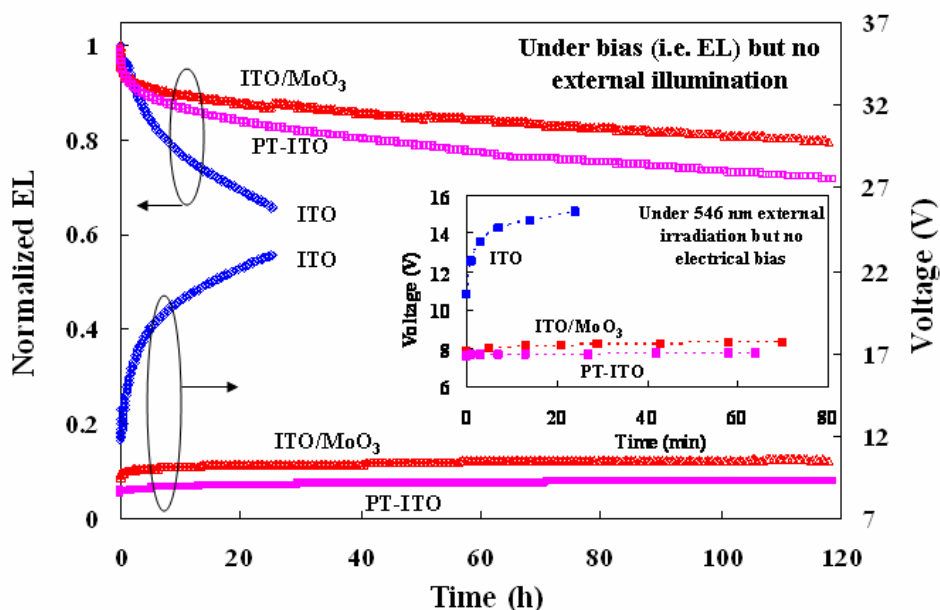


Figure 5.2: Normalized EL and V_d at current density of 20 mA cm^{-2} versus electrical aging time of OLEDs with the structures ITO/NPB(70nm)/Alq₃(70nm)/Mg:Ag(100nm), PT-IITO/NPB(70nm)/Alq₃(70nm)/Mg:Ag(100nm) and ITO/MoO₃(1nm)/NPB(70nm)/Alq₃(70nm)/Mg:Ag(100nm). Inset: V_d at current density of 10 mA cm^{-2} versus 546 nm irradiation time of OLEDs with the same structures.

Having seen the photo-stability of different ITO/organic contacts and their role in enhancing the stability of OLEDs, it is desirable to find out if the mechanism behind the anode/organic contacts photo-degradation process is chemical in nature. As a result, XPS measurements were used to test if irradiation results in any changes in the chemical characteristics of the ITO/organic interface. For this analysis, the ITO/NPB, PT-IITO/NPB and ITO/MoO₃/NPB as representative contacts were studied, in consideration of the fact that NPB is a very widely used hole-transport material in organic optoelectronic devices.

Figure 5.3(a) shows the binding energy spectra of In 3d electrons collected from test samples of untreated ITO films and ITO/NPB(3nm) stacks coated on glass substrates. One set of samples has been exposed to 365 nm irradiation at a power density of $\sim 0.5 \text{ mW cm}^{-2}$ for 10 hours in a N_2 atmosphere whereas the other set (control) has been kept in the dark (and also in N_2) for the same period of time. The N_2 atmosphere is used in order to avoid possible ambient oxygen-mediated photo-oxidation and/or other ambient-induced photochemical changes. Furthermore, to ensure that any such ambient-induced photochemical changes remain negligible in the event that trace amounts of residual ambient oxygen remain in the environment, the samples contained an additional thick Ag protective layer ($\sim 100 \text{ nm}$) covering the NPB.⁴⁶ Therefore, the irradiation by the 365 nm illumination was done from the ITO side. The top thick silver layer is peeled off by an adhesive tape immediately before the XPS measurements. As shown in figure 5.3(a), a spectral shift in the binding energy is observed in samples containing a thin layer of NPB coated on the untreated ITO surface, suggesting a reconfiguration of the In 3d electrons, possibly a sign of new bond formation with NPB. There is, however, no detectable difference in the spectra collected from the sample kept in the dark versus those collected from the irradiated one, indicating that irradiation has no major effect on the chemical state of indium in ITO. Figure 5.3(b) shows the O 1s electron binding energy spectra collected from the same samples. The spectrum collected from the ITO sample shows a peak at 530.4 eV, characteristic of In_2O_3 ,⁷⁴ and a broad shoulder at around 532 eV, which corresponds to InO_x ⁷⁴ and/or In(OH)_x .⁷⁵ In samples where ITO is coated with a thin layer of NPB, a new band with peak at 533 eV can be observed. This band can be attributed to a bond between O (in ITO) and aryl group of NPB.⁷⁶ The intensity of this new band was somewhat lower in spectrum collected from the irradiated sample. The decrease in the intensity of this band with irradiation suggests a decrease in the density of this bond, which may also be the reason behind the deterioration in hole injection upon prolonged irradiation.

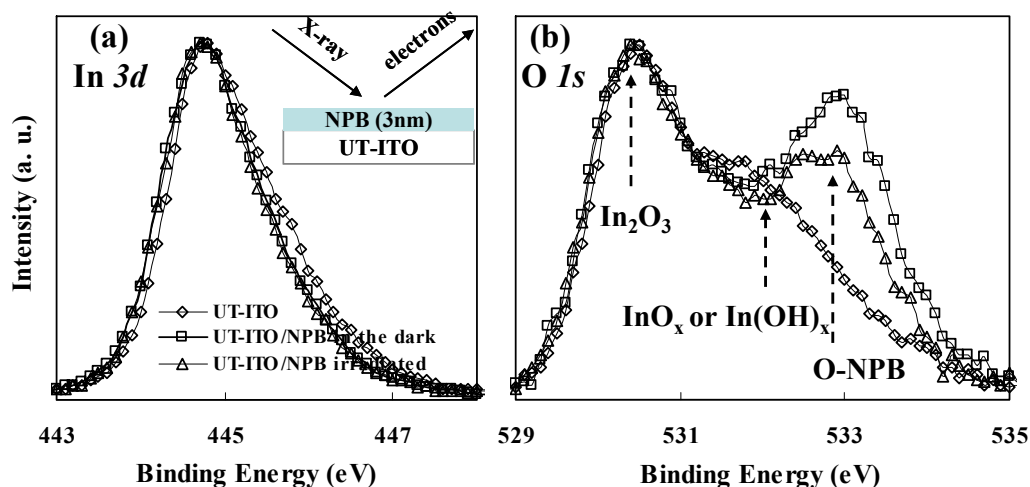


Figure 5.3: (a) In 3d electron binding energy spectra from ITO substrate and ITO/NPB(3nm). (b) O 1s electron binding energy spectra from the same samples. A 365 nm illumination at a power density of $\sim 0.5 \text{ mW cm}^{-2}$ is used for irradiation for a period of 10 hours.

Figure 5.4(a) and (b) show the binding energy spectra of the In 3d and O 1s electrons, respectively, obtained from test samples of PT-ITO films and PT-ITO/NPB(3nm) stacks, also coated on glass substrates, and subjected to the same conditions as those used above. Similar to the case of untreated ITO/NPB contact, a small spectral shift in the binding energy of In 3d electrons is observed in samples containing a thin NPB layer coated on the PT-ITO. Again, figure 5.4(a) shows no appreciable differences in the In 3d spectra collected from the sample kept in the dark versus those collected from the irradiated one. However, at odds with the case of untreated ITO/NPB, the spectra of O 1s electrons in case of the PT-ITO/NPB (in figure 5.4(b)) show only the In_2O_3 and InO_x and/or In(OH)_x bands but not the 533 eV band (corresponding to O-NPB bond). Figure 5.4(c) shows the F 1s electron binding energy spectra obtained from the same samples. In this figure, the band with peak at 685 eV corresponds to InF_3 ⁶⁶ which results from the CF_4/O_2 plasma treatment of the ITO. Except for a small increase in the 687-690 eV range, the F 1s spectrum from the PT-ITO/NPB sample kept in the dark is very similar to that from the bare PT-ITO sample. In contrast, the spectrum from the irradiated PT-ITO/NPB sample contains a strong second band, revealing a photo-induced change in the chemical characteristics of the PT-ITO/NPB contact. The peak of this band is at 688.5 eV, suggesting it may be associated with a bond between F and the aryl group of NPB.⁷⁷ The results therefore suggest that the photo-induced degradation of the PT-ITO/NPB contact could be occurring, mechanistically, by the break-down of InF_3 and the formation of fluorinated NPB species.

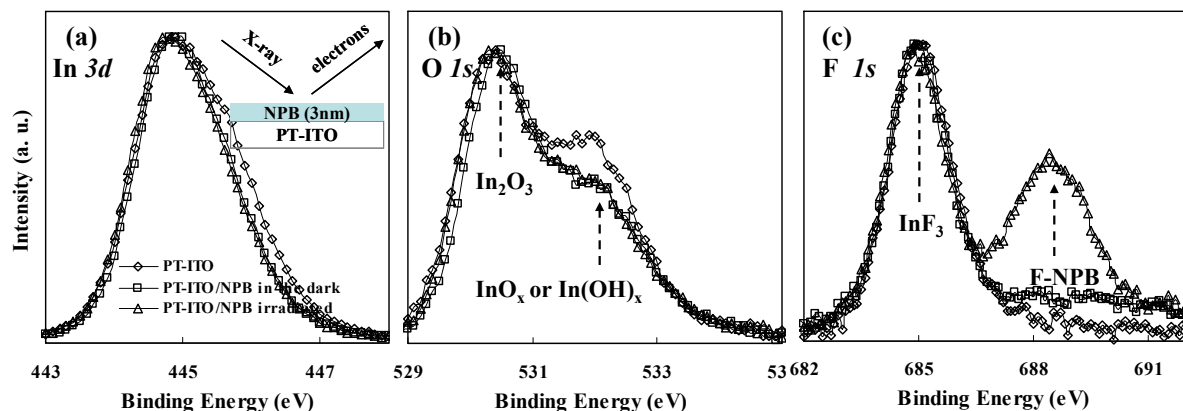


Figure 5.4: (a) In 3d electron binding energy spectra from PT-ITO substrate and PT-ITO/NPB(3nm). (b) O 1s and (c) F 1s electron binding energy spectra from the same samples. A 365 nm illumination at a power density of $\sim 0.5 \text{ mW cm}^{-2}$ is used for irradiation for a period of 10 hours.

Figure 5.5(a) and b show the In 3d and O 1s electron binding energy spectra from test samples of untreated ITO/MoO₃(1nm) and untreated ITO/MoO₃(1nm)/NPB(3nm). The In spectra show essentially the same behavior as in the other samples, again exhibiting no appreciable changes in the irradiated samples. The O spectra from ITO/MoO₃(1nm)/NPB(3nm) also show no changes by irradiation, but that from ITO/MoO₃(1nm) exhibits a broader band with the peak at 532 eV, which can be ascribed to hydroxyl (OH) groups and the absorbed water by MoO₃ film.⁷⁸ Figure 5.5(c) shows the Mo 3d electron binding energy spectra from the same samples. As the figure shows, a clear spectral shift to lower binding energy is observed in the sample containing the thin NPB, suggesting a bond formation between MoO₃ and NPB. This spectral shift is due to the relative increase of the lower oxidation states Mo⁺⁴ and Mo⁺⁵ with respect to Mo⁺⁶, indicating the partial transition from MoO₃ to MoO₂ and Mo₂O₅ with the NPB deposition onto ITO/MoO₃.⁷⁹ In contrast, the Mo 3d spectrum from the irradiated sample displays a small (yet clearly resolvable) shift towards higher binding energy, indicating a photo-induced chemical change in the ITO/MoO₃/NPB contact, possibly associated with a cleavage of the bonds.

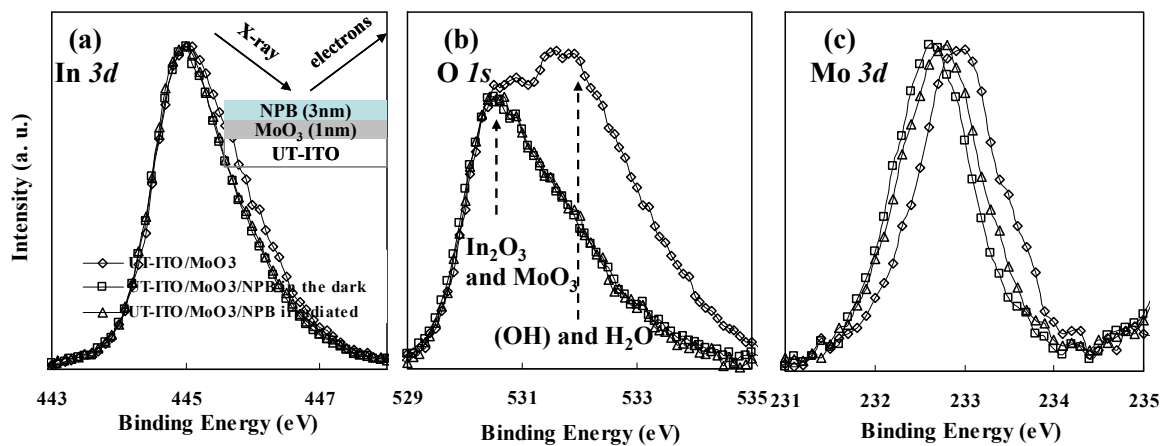


Figure 5.5: (a) In 3d electron binding energy spectra from samples ITO/MoO₃(1nm) and UT-ITO/MoO₃(1nm)/NPB(3nm). (b) O 1s and (c) Mo 3d electron binding energy spectra from the same samples. A 365 nm illumination at a power density of $\sim 0.5 \text{ mW cm}^{-2}$ is used for irradiation for a period of 10 hours.

From the above analysis, it may be concluded that irradiation of these contacts always leads to a re-distribution in the chemical bonds. In the case of untreated and plasma treated samples, this variation in chemical bonding may be associated with the photo-degradation of the studied organic optoelectronic devices due to prolonged irradiation. In the case of the MoO₃ samples, the change in chemical bonding is either insignificant or irrelevant to the interface's capacity to inject or extract holes.

In conclusion, irradiation by light in the visible and UV range is found to result in a gradual deterioration in the electrical properties of a number of ITO/organic contacts commonly used in OLEDs. This photo-induced contact degradation can be greatly reduced by the interfacial modification of the ITO/organic contacts such as the treatment of the ITO surface and the insertion of interfacial layers between ITO and the organic layer. A correlation between the photo-stability of the ITO/organic contacts and the stability of OLEDs is found. XPS measurements reveal detectable changes in the interface characteristics after irradiation, indicating that the photo-degradation of the ITO/organic contacts is chemical in nature. Changes in XPS characteristics after irradiation suggest a possible reduction in bonds between ITO and its adjacent organic layer. The results shed the light on a new material degradation mechanism that appears to have a wide presence in ITO/organic contacts

in general, and which likely plays a key role in limiting the stability of various organic optoelectronic devices such as OLEDs, OPDs and OSCs.

5.2 Summary

In this chapter, exciton-induced degradation of ITO/organic interfaces is investigated. Results show that such interfacial degradation result in a gradual deterioration in the electrical properties of a number of ITO/organic interfaces commonly used in OLEDs. Such degradation was found to be photo-chemical in nature, associated with a reduction in bonds between ITO and its adjacent organic layer. This degradation can be greatly reduced by the interfacial modification of the ITO/organic contacts such as the treatment of the ITO surface and the insertion of interfacial layers between ITO and the organic layer.

Chapter 6

Degradation of Organic/Organic Interfaces due to Exciton-Polaron Interactions

In this chapter, degradation of organic/organic interfaces will be studied. Firstly, degradation of organic/organic interfaces due to exciton-polarons interactions will be investigated in section 6.1. After that, the attention will be turned to highly efficient PhOLEDs, where degradation mechanisms of host and guest materials will be respectively uncovered in sections 6.2 and 6.3.

6.1 Degradation of Organic/organic Interfaces by Exciton-Polaron Interactions

The material presented in this section was published in *ACS Appl. Mater. Interfaces* **5**, 8733–8739 (2013). It is reproduced here with the permission from the publisher.

The stability of the CBP/TPBi interface under various stress scenarios was first studied. For this purpose, CBP hole-only devices that contain a thin TPBi layer (~5nm), and thus a CBP/TPBi interface, and others without the TPBi layer for comparison were utilized. The structure of the devices is ITO(120nm)/MoO₃(5nm)/CBP(20nm)/TPBi(5nm or 0nm)/CBP(20nm)/MoO₃(5nm)/Al(100nm). When under a forward bias (i.e. ITO is positively biased relative to Al), the 5 nm MoO₃ on the ITO side facilitates hole injection from ITO to CBP and the 5 nm MoO₃ on the Al side prevents electron injection from Al to CBP. Given the high hole mobility of CBP,⁸⁰ these devices show hole-only transport characteristics. As these devices do not emit light, changes in driving voltage (V_d) were used as an indicator of device degradation due to the different stress conditions. **Figures 6.1(a) and (b)** show the changes in V_d (ΔV), defined as the V_d at any given time needed to drive a current of density 20 mA/cm² minus the initial V_d (at time = 0) in the devices with and without the TPBi layer, respectively, as a function of time, during which these devices are subjected to one of the following stress scenarios: (1) Current flow only (denoted by <I only>), under a forward bias to sustain a current flow of density ~20 mA/cm²; (2) Irradiation by light only (denoted by <L_{365nm} only>), at 365 nm of power density ~0.5 mW/cm²; and (3) Current flow and irradiation together (denoted by <I + L_{365nm}>), in which the device is subjected to conditions (1) and (2) simultaneously.

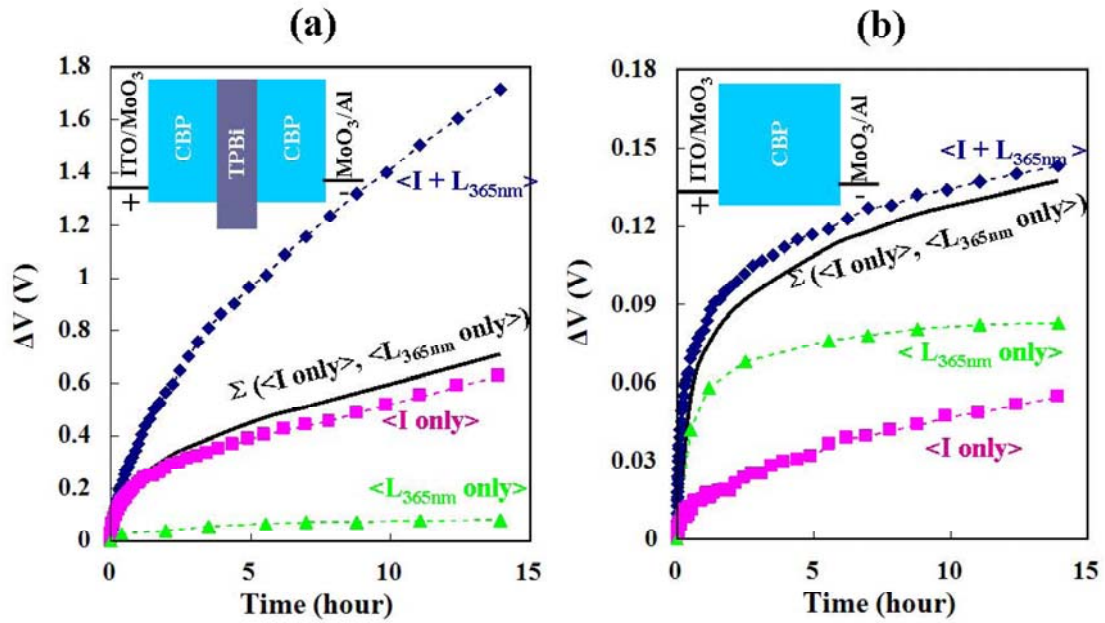


Figure 6.1: Change in V_d at 20 mA/cm^2 in devices (a) with and (b) without the TPBi layer, versus time, during which the devices are subjected to stress scenarios: $\langle I \text{ only} \rangle$, $\langle L_{365\text{nm}} \text{ only} \rangle$ and $\langle I + L_{365\text{nm}} \rangle$. The curve $\Sigma(\langle I \text{ only} \rangle, \langle L_{365\text{nm}} \text{ only} \rangle)$ represents the algebraic sum of the ΔV in $\langle I \text{ only} \rangle$ and $\langle L_{365\text{nm}} \text{ only} \rangle$.

As CBP absorbs significantly at 365 nm whereas TPBi does not, this irradiation wavelength allows exciting CBP only, creating CBP singlet excitons. The initial V_d of the devices with and without the TPBi layer (i.e. for the trends in figures 6.1(a) and 1(b), respectively) is $\sim 5.5 \text{ V}$ and $\sim 1.3 \text{ V}$, respectively. As the figures show, subjecting both types of devices to light alone (i.e. $\langle L_{365\text{nm}} \text{ only} \rangle$) for 14 hours results in a small increase in V_d ($\Delta V \sim 0.08 \text{ V}$). As both devices exhibit almost the same increase in voltage due to the irradiation, it follows that the underlying (light-induced) changes must be occurring in layers and/or interfaces that are present in both devices, and therefore are not related to the TPBi layer or the CBP/TPBi interface. The flow of current only (i.e. $\langle I \text{ only} \rangle$) leads to an increase in V_d of $\sim 0.63 \text{ V}$ and 0.05 V in the devices with and without the TPBi layer, respectively. The larger ΔV exhibited by the device containing the TPBi layer may be attributed to hole accumulation at the CBP/TPBi interface due to the hole-blocking effect of TPBi.¹⁸ Exposing the devices to irradiation and current flow simultaneously (i.e. $\langle I + L_{365\text{nm}} \rangle$) results in a faster increase in V_d in comparison to that induced by irradiation alone or current flow alone. What is most remarkable

however is that the much faster increase in V_d in the device with the TPBi layer by this stress scenario ($\Delta V \sim 1.71$ V) surpasses not only that in the device without the TPBi by the same scenario ($\Delta V \sim 0.14$ V) but also those produced by the separate exposure to irradiation or current flow (0.63 V and 0.08 V, respectively). For comparison, traces representing the algebraic sum of the ΔV 's caused by $\langle I \text{ only} \rangle$ and $\langle L_{365\text{nm}} \text{ only} \rangle$ (denoted by $\Sigma(\langle I \text{ only} \rangle, \langle L_{365\text{nm}} \text{ only} \rangle)$) were included. As can be seen from figure 6.1(a), the measured ΔV values produced by the $\langle I + L_{365\text{nm}} \rangle$ scenario are much higher than the corresponding computed $\Sigma(\langle I \text{ only} \rangle, \langle L_{365\text{nm}} \text{ only} \rangle)$ values, indicating that the effect of simultaneous exposure to light and current significantly surpasses the sum (or linear combination) of their individual contributions. This suggests that some interaction between the two stimuli (illumination and current flow) occurs, which leads to additional or faster degradation, hence the much faster voltage rise in this case. Since the distinguishing feature of $\langle I + L_{365\text{nm}} \rangle$, as compared to $\langle I \text{ only} \rangle$ and $\langle L_{365\text{nm}} \text{ only} \rangle$, is the presence of both positive polarons and CBP excitons simultaneously, it is possible that the additional degradation in $\langle I + L_{365\text{nm}} \rangle$ in figure 1(a) is due to interactions between positive polarons and CBP singlet excitons. Given that the concentration of excitons will be relatively uniform across the entire CBP layers (attenuation of 365nm light in 40 nm of CBP is approximately 5%⁸¹) whereas the concentration of positive polarons will generally be higher at the CBP/TPBi interface, this interaction will most likely take place at the CBP/TPBi interface, rather than inside the CBP layer bulk or at the opposite TPBi/CBP interface. As the concentration of excitons within the TPBi layer must be very small (TPBi absorption at 365nm is negligible and energy transfer from CBP to TPBi is inefficient due to the wider bandgap of TPBi), such interactions between excitons and polarons can not be happening within the TPBi layer bulk. The results therefore suggest that interactions between CBP singlet excitons and CBP positive polarons at the CBP/TPBi interface must be behind the additional degradation. This is further verified from devices without TPBi, and thus no CBP/TPBi interface, in figure 6.1(b), where the ΔV in case of $\langle I + L_{365\text{nm}} \rangle$ is approximately equal to the sum of the individual effects of illumination and current (i.e. $\Sigma(\langle I \text{ only} \rangle, \langle L_{365\text{nm}} \text{ only} \rangle)$), indicating that the additional degradation processes are not significant when the interface is absent. To check if the second interface, i.e. the TPBi/CBP one, is contributing to this degradation behavior, hole-only devices that do not have the second CBP layer, and thus no TPBi/CBP interface [i.e. ITO/MoO₃(5nm)/CBP(20nm)/TPBi(5nm)/MoO₃(5nm)/Al(100nm)] were tested, in order to compare their behavior to that of the devices in figure 6.1(a). The results show that these devices have essentially the same degradation behavior as that of the devices reported in figure 6.1(a), indicating that the second interface does not play a significant role in the observed degradation behavior. The

additional degradation in $\langle I + L_{365\text{nm}} \rangle$ in figure 6.1(a) is therefore primarily interfacial, and is likely induced by interactions between CBP positive polarons and CBP singlet excitons at the CBP/TPBi interface. It should be noted that hole-only devices subjected to $\langle I \text{ only} \rangle$ and $\langle L_{365\text{nm}} \text{ only} \rangle$ in sequence (first $\langle I \text{ only} \rangle$ then $\langle L \text{ only} \rangle$ or first $\langle L \text{ only} \rangle$ then $\langle I \text{ only} \rangle$) show similar ΔV as in $\Sigma(\langle I \text{ only} \rangle, \langle L_{365\text{nm}} \text{ only} \rangle)$. This indicates that this interfacial degradation indeed occurs only when both excitons and polarons co-exist, as opposed, for example, to being the product of their individual effects in some particular sequence of events.

Finding that CBP/TPBi interface degrades significantly when both positive polarons and excitons on CBP are present, similar studies were conducted on NPB/AIQ₃ interface, utilizing NPB based hole-only devices that contain a thin AIQ₃ layer (~5nm thick), and thus an NPB/ AIQ₃ interface, and others without the AIQ₃ layer for comparison. The device structure is ITO(120nm)/MoO₃(5nm)/NPB(20nm)/AIQ₃(5nm or 0 nm)/NPB(20nm)/MoO₃(5nm)/Al(100nm), respectively. Figures 6.2(a) and (b) show the changes in V_d at 20 mA/cm² in devices with and without the AIQ₃ layer, respectively, as a function of time, under the same stress scenarios used above: $\langle I \text{ only} \rangle$, $\langle L_{365\text{nm}} \text{ only} \rangle$ and $\langle I + L_{365\text{nm}} \rangle$. In addition, a fourth scenario, $\langle I + L_{405\text{nm}} \rangle$, was used in which the device is subjected to current flow of density ~20 mA/cm² and 405 nm irradiation of power density ~0.5 mW/cm² simultaneously. As the 405 nm irradiation can excite AIQ₃ only, whereas the 365 irradiation can excite both NPB and AIQ₃, including this fourth scenario allows differentiating between the influence of NPB excitons versus AIQ₃ excitons in the degradation process. This approach was difficult to implement in case of the CBP/TPBi devices due to the significant overlap between CBP and TPBi optical absorption spectra, which makes it impossible to excite TPBi without exciting CBP. The V_d of the devices with and without the AIQ₃ layer (i.e. for the trends in figures 6.2(a) and 2(b), respectively) is ~8 V and ~2.4 V, respectively.

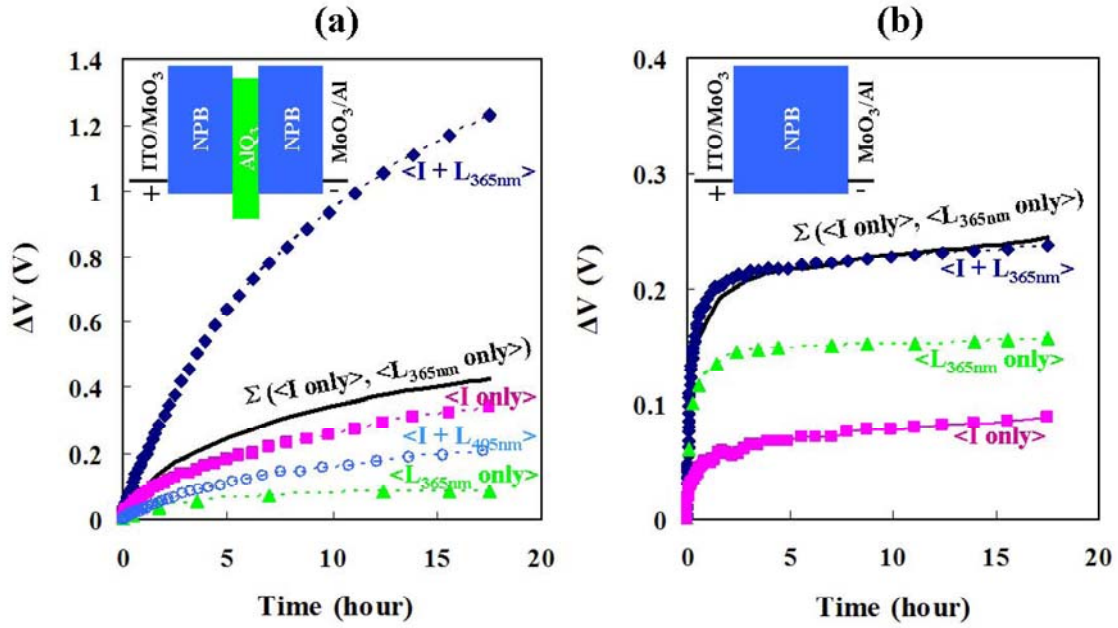


Figure 6.2: Changes in V_d at 20 mA/cm^2 in devices (a) with and (b) without the AlQ_3 layer, versus time, during which the devices are subjected to stress scenarios: $\langle \text{I only} \rangle$, $\langle \text{L}_{365\text{nm}} \text{ only} \rangle$, $\langle \text{I} + \text{L}_{365\text{nm}} \rangle$ and $\langle \text{I} + \text{L}_{405\text{nm}} \rangle$. The curve $\Sigma(\langle \text{I only} \rangle, \langle \text{L}_{365\text{nm}} \text{ only} \rangle)$ represents the algebraic sum of the ΔV in $\langle \text{I only} \rangle$ and $\langle \text{L}_{365\text{nm}} \text{ only} \rangle$.

As can be seen from the figures, the three stress scenarios $\langle \text{L}_{365\text{nm}} \text{ only} \rangle$, $\langle \text{I only} \rangle$ and $\langle \text{I} + \text{L}_{365\text{nm}} \rangle$ bring about changes in the V_d of the devices with and without the AlQ_3 layer that very closely resemble, qualitatively, those in figure 6.1. Here again the exposure to light alone ($\langle \text{L}_{365\text{nm}} \text{ only} \rangle$) results in small and comparable changes in the V_d ($\Delta V \sim 0.08$) in devices with and without the AlQ_3 , indicating that these changes are not related to the AlQ_3 layer or the NPB/AlQ_3 interface. $\langle \text{I only} \rangle$ produces larger ΔV in case of the device with the AlQ_3 layer, which, again, can be attributed to hole accumulation at the NPB/AlQ_3 interface. Most importantly, again the ΔV caused by $\langle \text{I} + \text{L}_{365\text{nm}} \rangle$ surpasses the sum of the individual effects of illumination and current (i.e. $\Sigma(\langle \text{I only} \rangle, \langle \text{L}_{365\text{nm}} \text{ only} \rangle)$) in case of the device with the AlQ_3 layer (figure 6.2(a)), but not in case of the device without the AlQ_3 layer (figure 6.2(b)). Such comparison again points to additional degradation mechanisms when the interface is present and is subjected to current and light simultaneously, revealing that interfacial degradation due to polaron-exciton interactions occurs in case of NPB/AlQ_3 as well. More details of such degradation are revealed by utilizing 405 nm irradiation in figure 6.2(a), where the ΔV caused

by $\langle I + L_{405\text{nm}} \rangle$ is not as large as that caused by $\langle I + L_{365\text{nm}} \rangle$ (note: the same power densities were used for both 365 nm and 405 nm irradiation. Therefore the number of photons in case of 405nm irradiation is necessarily higher. As AIQ₃ absorption at 405 nm is also higher, the number of excitons on AIQ₃ in this scenario will be significantly higher). Since only AIQ₃ excitons but no NPB excitons are created by the scenario $\langle I + L_{405\text{nm}} \rangle$, the results suggest that only NPB excitons play a significant role in NPB/AIQ₃ interfacial degradation process. It should be pointed out that the ΔV in case of $\langle I + L_{405\text{nm}} \rangle$ is even slightly smaller than that in case of $\langle I \text{ only} \rangle$, which may be due to the higher conductivity of AIQ₃ when under 405 nm irradiation which would reduce the concentration of polarons on the NPB side of the interface.

It is noteworthy to point out that similar studies utilizing electron-only devices were also conducted to investigate if interactions between ETM negative polarons and excitons may have a similar effect on HTM/ETM interfaces. Preliminary results however show that subjecting the interfaces to electron current and light simultaneously leads to very little additional degradation. This may be due to the lower accumulation of electrons (relative to holes) at the HTM/ETM interfaces. It is also possible that interactions between ETM negative polarons and excitons do not cause the same degradation effect.

Since the above results show that interactions between positive polarons and singlet excitons on the HTM are responsible for HTM/ETM interfacial degradation, it would be expected that reducing the exciton lifetime would reduce the interaction probability and thus slow down the degradation mechanism. To test for this, the effect of introducing a very thin layer of a narrower band-gap material, DCJTb, on the degradation behavior of the hole-only CBP/TPBi devices was studied. As the absorption spectrum of DCJTb and the emission spectrum of CBP significantly overlap, transfer of excitons from CBP to DCJTb via Forster process can be quite efficient, which would therefore reduce the lifetime of CBP singlet excitons. This effect is verified by fluorescence lifetime measurements. Figure 3 shows fluorescence versus time at 405 nm (i.e. from the relaxation of CBP singlet states) collected from a neat CBP film and a DCJTb-doped CBP film (doped at 4% by volume) excited by a 379 nm laser pulse (pulse width ~ 71 ps, average power ~ 5 mW). Clearly, the decay rate of CBP fluorescence becomes much faster in the presence of DCJTb, confirming the role of DCJTb in shortening the lifetime of CBP excitons.

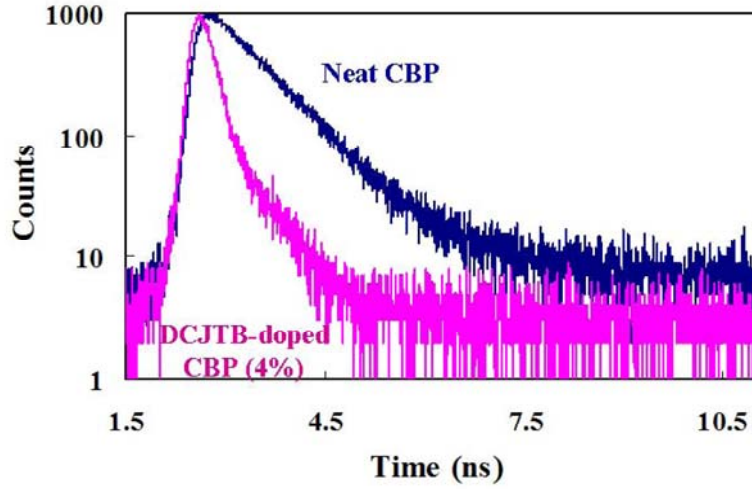


Figure 6.3: Time domain CBP fluorescence lifetime of 30 nm neat CBP and DCJTB-doped CBP (4%) films, excited by a 379 nm pulsed laser.

Figures 6.4(a)-(c) show changes in V_d under the three stress scenarios $\langle I \text{ only} \rangle$, $\langle L_{365\text{nm}} \text{ only} \rangle$ and $\langle I + L_{365\text{nm}} \rangle$ of CBP/TPBi hole-only devices containing an ultra thin layer ($\sim 0.5 \text{ \AA}$ thick) of DCJTB, located at various distances from the CBP/TPBi interface. Figure 6.4 (d) show the changes in V_d under the same conditions in case of a control device without a DCJTB layer. The initial V_d of these devices in figure 4(a)-(d) is 7.2 V, 8.5 V, 9.4 V and 5.2 V, respectively. As can be seen from the figure, introducing the ultra thin layer of DCJTB at a distance of $\sim 5\text{nm}$ from the CBP/TPBi interface has almost no effect on the degradation behavior of the devices, evident in the close similarity between the voltage rise trends in figures 6.4(a) and (d). In contrast, as can be seen from figure 6.4(b), placing the layer much closer to the interface (only $\sim 1 \text{ nm}$ away) reduces the voltage rise caused by the $\langle I + L_{365\text{nm}} \rangle$ scenario significantly, pointing to a slow down in the degradation process in comparison to the control device. Quite remarkably, the voltage trend becomes very similar to the sum of the individual effects of illumination and current (i.e. $\Sigma(\langle I \text{ only} \rangle, \langle L_{365\text{nm}} \text{ only} \rangle)$), suggesting that the additional degradation by exciton-polaron interactions are indeed greatly suppressed in this case. As the only difference between this device in figure 6.4(b) and that in 6.4(a) is the closer proximity of the DCJTB layer to the CBP/TPBi interface, which becomes comparable to the Forster radius in case of 6.4(b) and thus allows efficient Forster energy transfer from CBP excitons in the vicinity to the DCJTB layer, it is evident that reducing the lifetime of CBP excitons in the vicinity of the interface can indeed slow down the degradation process. That the DCJTB layer

does not produce the same effect when the layer is 5nm away from the interface further verifies that the degradation process is entirely interfacial. Furthermore, the fact that the DCJTB layers affect the V_d stability differently in 6.4(b) and 6.4(a) even though they (i.e. the DCJTB layers) fall on the conduction path of holes from the ITO/MoO₃ contact to the CBP/TPBi interface in both cases rules out that the effect may primarily be result of a change in the polaron concentration in the CBP layer or at the CBP/TPBi due to hole trapping on DCJTB. This is further verified from tests on the device where the DCJTB layer is located into the TPBi layer and therefore “down stream” on the hole conduction path relative to the CBP/TPBi interface. It can be clearly seen from figure 6.4(c) that in this case the DCJTB brings about almost the same effect on the V_d stability as that in case of figure 6.4(b). Since one can expect energy transfer from CBP excitons at the interface to the DCJTB layer via the Forster process to be similar in case of 6.4(b) and 4(c) (both have DCJTB located at the same distance from the interface) whereas polaron redistribution due to the presence of the DCJTB can be expected to be different in the two cases, the results convincingly prove that the primary role of DCJTB in enhancing the stability under the <I + L365nm > scenario stems from its role in reducing the lifetime of CBP excitons.

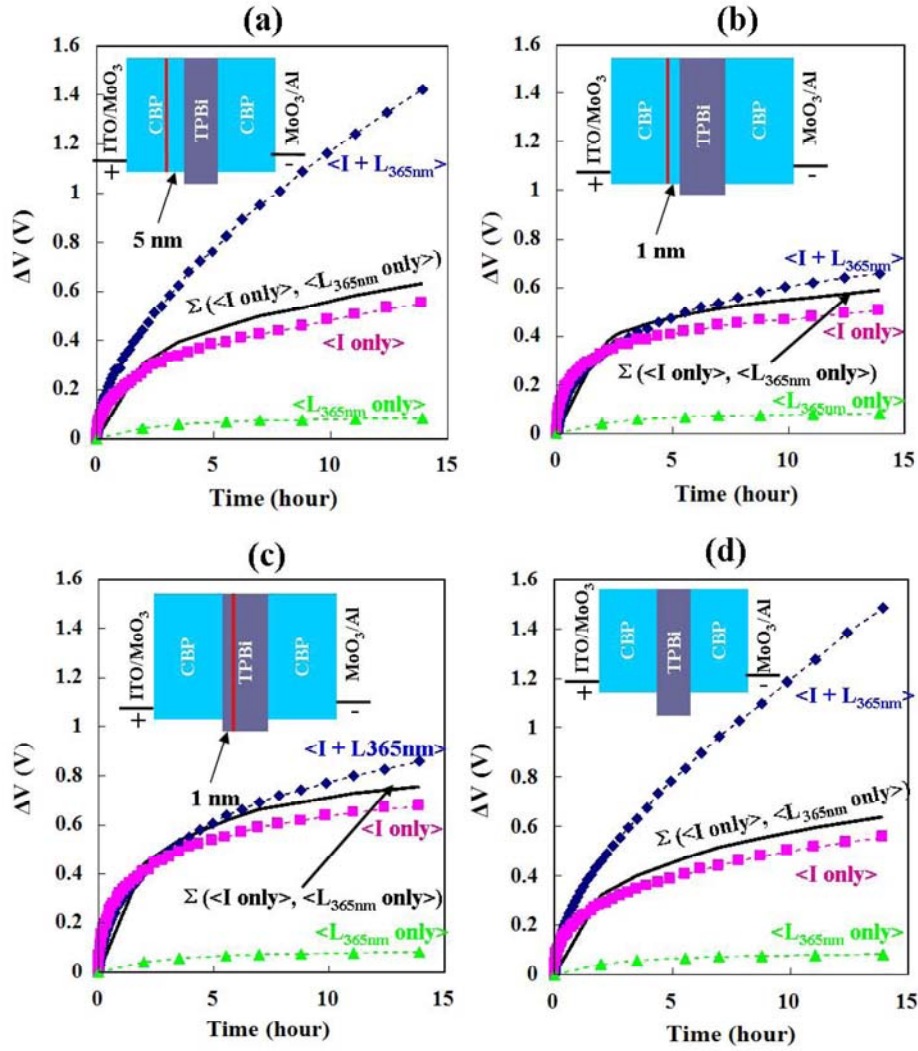


Figure 6.4: Changes in V_d at 20 mA/cm^2 in devices where (a) the DCJTB layer is in the CBP and 5 nm away from the CBP/TPBi interface, (b) the DCJTB layer is in the CBP and 1 nm away from the CBP/TPBi interface, (c) the DCJTB layer is in the TPBi and 1 nm away from the CBP/TPBi interface and (d) no DCJTB layer is present, versus time, during which the devices are subjected to scenarios: $\langle I \text{ only} \rangle$, $\langle L_{365\text{nm}} \text{ only} \rangle$ and $\langle I + L_{365\text{nm}} \rangle$. The curve $\Sigma(\langle I \text{ only} \rangle, \langle L_{365\text{nm}} \text{ only} \rangle)$ represents the algebraic sum of the ΔV in $\langle I \text{ only} \rangle$ and $\langle L_{365\text{nm}} \text{ only} \rangle$.

The above results clearly reveal that HTM/ETM interfaces degrade rapidly when both HTM positive polarons and HTM singlet excitons are present simultaneously in their vicinity, resulting in a deterioration in conduction across the interface. This degradation mechanism involves some

interaction between the two species (i.e. HTM positive polarons and HTM singlet excitons) and can be slowed down if exciton lifetime is made shorter. Although the observations are obtained from hole-only test devices, the close similarity between the interface conditions in these test devices and actual OLEDs suggests that the same phenomenon likely happens at interfaces of actual OLEDs. To further investigate this, the V_d stability of archetypical OLEDs containing CBP/TPBi and NPB/AIQ₃ interfaces were studied. In some of these devices, a small amount of 3,4,9,10-perylenetetracarboxylic-bis-benzimidazole (PTCBI) was introduced, to serve as an exciton quencher, in a portion of the ETM, thereby test the effect of reducing exciton lifetime (and concentration) on the device performance. Changes in V_d versus time of continuous electrical driving at 20 mA/cm² in two CBP/TPBi based OLEDs of structures ITO(120nm)/MoO₃(5nm)/CBP(40nm)/TPBi(30nm)/LiF(1nm)/Al(100nm) and ITO(120nm)/MoO₃(5nm)/CBP(40nm)/TPBi(5nm)/TPBi:PTCBI(2%)(20nm)/TPBi(5nm)/LiF(1nm)/Al(100nm) were first monitored. The PTCBI is doped only in the middle region of the TPBi layer to avoid altering the chemical composition of the CBP/TPBi interface. The initial V_d of the devices with and without PTCBI is 10.2 V and 9.1 V, respectively. Under this electrical driving, the device without the PTCBI produces blue EL from CBP of brightness 50 cd/m², whereas, as expected, the device with the PTCBI shows no detectable EL due to the efficient quenching of CBP excitons by the PTCBI. the concentration of positive polarons in the CBP layer in the vicinity of the CBP/TPBi interface can be expected to be comparable in both devices (or slightly higher in case of the device with the PTCBI doped region due to a possible decrease in electron transport across the TPBi layer due to some electron trapping on PTCBI as the somewhat higher V_d suggests). At the same time, the lifetime of CBP excitons can be expected to be much shorter in case of the device with the PTCBI due to the quenching effect by the PTCBI. The interfacial degradation process would be therefore expected to be slower in case of the device with the PTCBI due to a reduction in exciton-polaron interactions and thus expect to see higher voltage stability in comparison to the control device (i.e. without PTCBI). Figure 6.5(a) shows the changes in V_d versus time of continuous electrical driving at 20 mA/cm² of these devices. As the figure shows, the device without the PTCBI shows an increase in voltage of 3.3 V, whereas the device with the PTCBI shows an increase in voltage of only 0.8 V, confirming the occurrence of CBP/TPBi interfacial degradation in OLEDs due to polaron-exciton interactions. It should be noted that tests on CBP/TPBi based OLEDs that contain phosphorescent dopants such as Ir(ppy)₃ show the same results. Similar studies on NPB/AIQ₃ based OLEDs were also carried out. Figure 6.5(b) shows the changes in V_d versus time of continuous electrical driving at

20 mA/cm² of these devices. The initial V_d of the devices with and without the PTCBI is 7.2 V and 5.4 V, respectively. The device without PTCBI produces green EL from AlQ₃ of a brightness of 450 cd/m², whereas the device with PTCBI produces only very weak EL (brightness of ~ 4 cd/m²). Again, as the figure shows, the device with the PTCBI shows a smaller ΔV than that without the PTCBI, indicating a slower interfacial degradation at the NPB/AlQ₃ interface. These results show that the degradation of HTM/ETM interfaces indeed occurs in OLEDs and is behind the fast increase in V_d in these devices with time; the latter being a behavior that is widely observed in OLEDs in general.

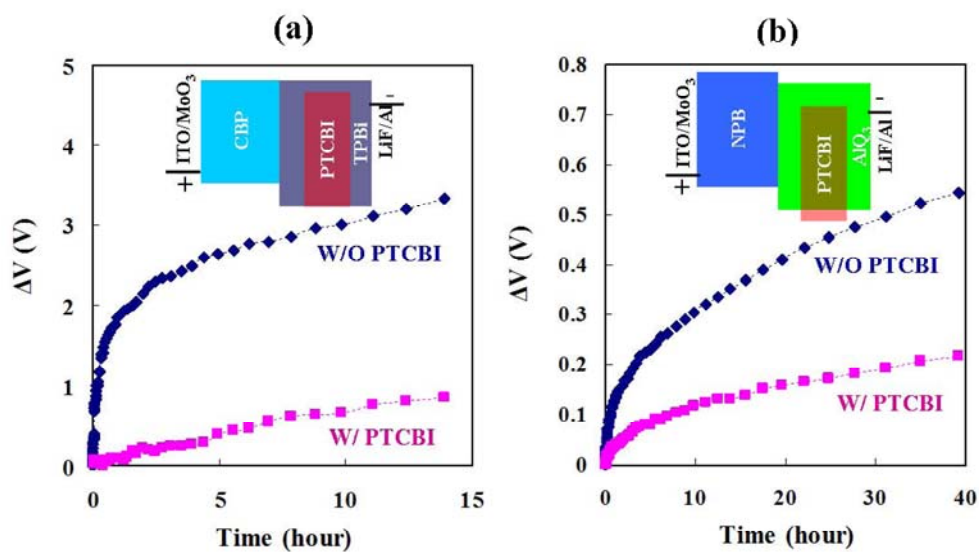


Figure 6.5: Change in driving voltage at a current density of 20 mA/cm² in (a) CBP/TPBi based and (b) NPB/AlQ₃ based OLEDs versus time of continuous electrical driving.

Although this study has focused on HTM/ETM interfaces, it is reasonable to expect that this interfacial degradation phenomenon will not be limited to these specific interfaces, but rather affect all organic/organic interfaces in general whenever both positive polarons and excitons are present in their vicinity. For example, in case of multi-layered OLEDs, build-up of positive polarons can occur at other device interfaces such as at interfaces between hole transport layers with different highest occupied molecular orbital energy levels. In addition, excitons may also be present at these interfaces due to diffusion from the electron-hole recombination zone. Therefore, such interfaces may be similarly susceptible to interfacial degradation as a result of polaron-exciton interactions.

In conclusion, it is found out that HTM/ETM interfaces commonly used in OLEDs degrade rapidly due to an interaction between HTM positive polarons and HTM singlet excitons. The phenomenon results in a deterioration in conduction across the interface, and contributes to the commonly observed increase in OLED driving voltage with electrical driving time. This interfacial degradation can be slowed down if exciton lifetime becomes shorter. The findings uncover a new degradation mechanism that is interfacial in nature, which affects organic/organic interfaces in OLEDs and contributes to their limited EL stability, and shed light on approaches for reducing it. Although this study has focused on OLEDs, the same degradation mechanism can be expected to affect organic/organic interfaces in other organic optoelectronic devices where both excitons and polarons are present in high concentrations, such as in organic solar cells or photodetectors.

6.2 Degradation of Host Materials

The material presented in this section was published in *Adv. Funct. Mater.* **24**, 2975-2985 (2014) and *Org. Electron.* DOI:10.1016/j.orgel.2015.08.019 (2015). It is reproduced here with the permission from the publishers.

6.2.1 Exciton-Polaron-Induced Aggregation (EPIA)

The degradation behavior of CBP/TPBi-based PhOLEDs, in which Ir(ppy)₃ is used as the phosphorescent emitter material doped into the CBP host in various concentrations, were first studied. The general structure of the devices is ITO/MoO₃(5nm)/CBP(30nm)/CBP:Ir(ppy)₃(10nm)/TPBi(30nm)/LiF(0.5nm)/Al(100nm), as shown in figure 6.6(a). The Ir(ppy)₃ concentration in these devices is 0, 0.1%, 1% or 4%. Figure 6.6(b) shows the changes in V_d (ΔV , defined as the V_d at any given time minus the initial V_d) and EL intensity (normalized to initial values) of the devices versus time during which the devices are continuously driven by a current of density 20 mA cm⁻². The initial brightness values of the devices with 0, 0.1%, 1% and 4% Ir(ppy)₃ are 50, 2000, 7800 and 7500 cd m⁻², respectively. The initial V_d values of these devices are 6.8, 7.3, 7.6 and 7.7 V, respectively. As the figure shows, an increase in Ir(ppy)₃ concentration leads to more stable EL and V_d with time. For example, the lifetime (defined as the time elapsed before the EL decreases to 50 % of its initial value) of the devices with 0, 0.1%, 1% and 4% Ir(ppy)₃ is ~0.2, 0.5, 8 and 19 hours, respectively. Such trend cannot be explained by the previously proposed mechanisms that attribute degradation primarily to excitons on guest molecules (i.e., Ir(ppy)₃ triplets in this case),³¹ since clearly the device with 0.1% Ir(ppy)₃ degrades much faster

than those with 1% and 4% Ir(ppy)₃, despite the lower concentration of Ir(ppy)₃ triplets. The trend also contradicts the commonly accepted notion that the lifetime of a PhOLED is inversely proportional to its initial brightness.⁸² Figure 6.6(c) shows normalized EL spectra of these devices. As expected, the devices with higher Ir(ppy)₃ concentration show less EL from CBP (i.e., the band at ~ 400 nm), an observation that can be attributed to the more efficient energy transfer from the host to guest molecules via Forster process as the guest concentration increases. A comparison of the results in figure 6.6(b) and (c) suggests there may be a correlation between the lower device stability of the devices with lower Ir(ppy)₃ concentrations and the higher ratio of CBP to Ir(ppy)₃ excitons in them.

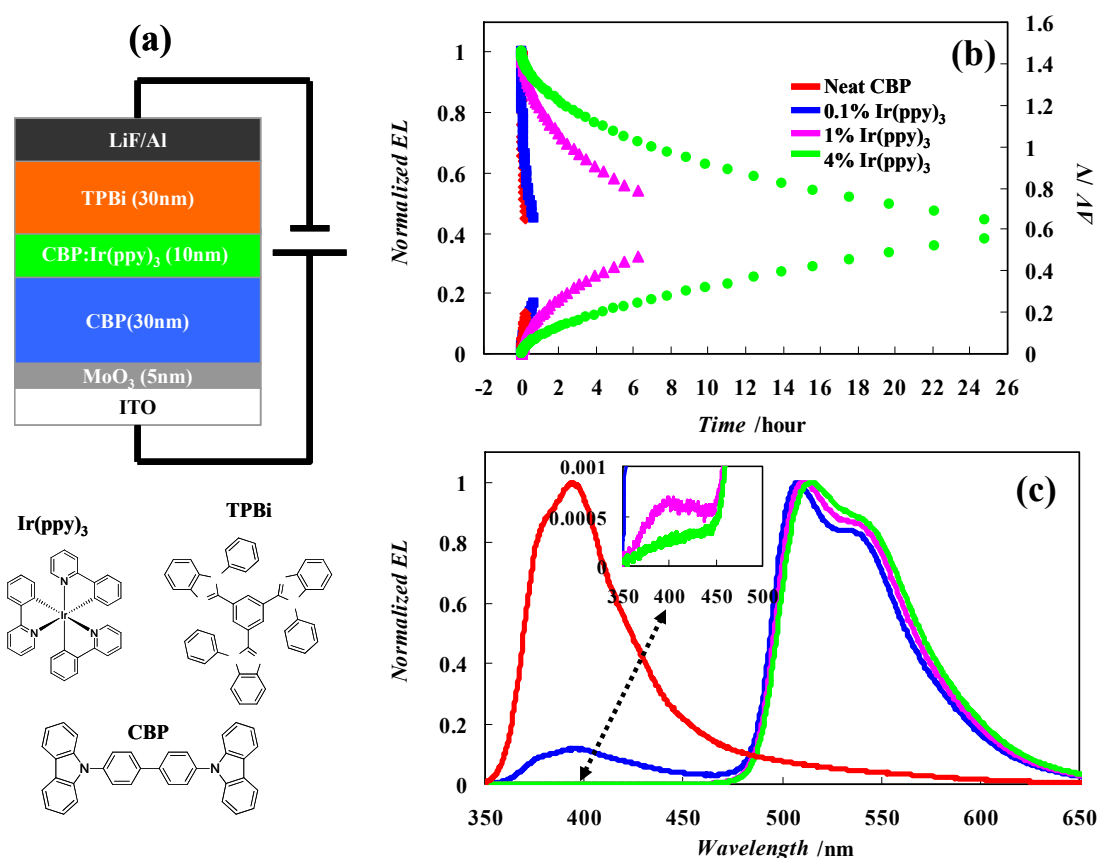


Figure 6.6: (a) Structure of PhOLEDs and molecular structures of the materials used. (b) Changes in normalized EL and V_d of the devices with different Ir(ppy)₃ concentrations versus time during which the devices are continuously driven by a current of density 20 mA cm⁻². (c) Normalized EL spectra of the devices. The inset of (c) shows a detailed view of the spectra in the short-wavelength region.

To verify this, the time-resolved photoluminescence (PL) of both CBP and Ir(ppy)₃ in CBP:Ir(ppy)₃ films with different Ir(ppy)₃ concentrations were studied. Figure 6.7(a) and (b) show luminescence decay in time at 400 nm and 520 nm (i.e., from the relaxation of CBP singlet excitons and Ir(ppy)₃ triplet excitons), respectively, collected from CBP:Ir(ppy)₃ films (~30 nm thick, deposited on a quartz substrate) with 0%, 0.1%, 1% and 4% Ir(ppy)₃ following excitation at 379 nm using a laser pulse (pulse width ~ 71 ps, average power ~ 5 mW). As figure 6.7(a) shows, the decay rate of CBP fluorescence becomes faster as Ir(ppy)₃ concentration increases. That the CBP fluorescence decay rates in the samples with 1% and 4% Ir(ppy)₃ are similar in figure 6.7(a) can be attributed to the very fast decay rate in both cases, which makes the rate approach the fall time of the laser excitation pulse itself as seen from the overlap in the curves. On the other hand, as can be seen in figure 6.7(b), the decay rate of Ir(ppy)₃ phosphorescence remains almost the same for the various Ir(ppy)₃ concentrations. The increase in CBP fluorescence decay as Ir(ppy)₃ concentration increases is indicative of a more efficient quenching of CBP excitons by Ir(ppy)₃ via Forster process. It follows that in PhOLEDs with higher Ir(ppy)₃ concentration the CBP excitons produced by electron-hole (e-h) recombination during device operation will also have shorter lifetime in comparison to in devices with lower Ir(ppy)₃ concentration. Therefore, in these devices, the number of CBP excitons present at any point in time will be smaller, which is also consistent with the observation that the EL from CBP in these devices is negligible. Such CBP-exciton dependence of PhOLEDs degradation, however, does not necessarily mean that the degradation process is simply caused by the presence of CBP excitons. It has been in fact determined that the presence of CBP excitons alone leads to very little degradation in bulk organic materials. On the other hand, the simultaneous presence of both CBP excitons and CBP positive polarons can cause significant degradation of the CBP/TPBi interface via exciton-polaron interactions, as already shown in section 6.1 of the thesis. Since the concentration of CBP positive polarons at the CBP/TPBi interface can be expected to be comparable in all devices in figure 6.6, whereas the lifetime of CBP excitons is much shorter in the devices with higher Ir(ppy)₃ concentration, the degradation process will be slower in the devices with higher Ir(ppy)₃ concentration due to the shorter CBP exciton lifetime, and thus a lower probability for exciton-polaron interactions. This is precisely the trend shown in figure 6.6. Therefore, the results in figure 6.6 and 6.7 are consistent with our recent findings in section 6.1 of the thesis that CBP excitons contribute to device degradation through their interactions with CBP positive polarons at the CBP/TPBi interface.

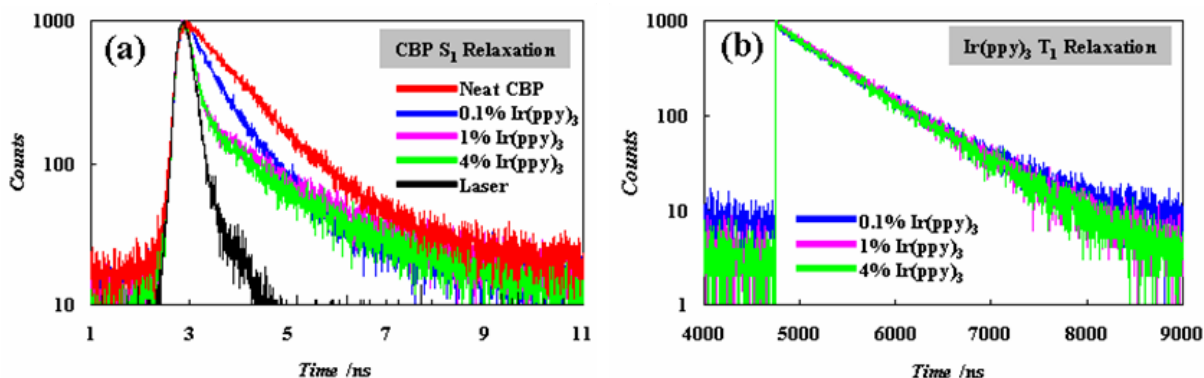


Figure 6.7: Luminescence decay in time (a) at 400 nm (i.e., from the relaxation of CBP singlet excitons) and (b) at 520 nm (i.e., from the relaxation of Ir(ppy)₃ triplet excitons) collected from CBP:Ir(ppy)₃ films with different Ir(ppy)₃ concentrations.

In order to obtain more insights into the mechanism by which interactions between excitons and polarons on CBP lead to device degradation, a device with a neat CBP emitting layer was studied. Figure 6.8(a) and (b) show EL spectra (with and without normalization, respectively) with continuous electrical driving at 20 mA cm^{-2} in a CBP/TPBi-based test-device of structure ITO/MoO₃(5nm)/CBP(40nm)/TPBi(30nm)/LiF(0.5nm)/Al(100nm). As the figures show, the device initially (at $t = 0$) produces blue EL from CBP with a band at $\sim 400 \text{ nm}$. With time, the EL spectrum gradually broadens and a new band with a peak at $\sim 500 \text{ nm}$ appears. The photographs in figure 6.8(b) depict the emission colors and corresponding CIE coordinates of the device before and after the electrical driving. Since the 500 nm band in the EL spectrum does not correspond to emission from either CBP or TPBi singlets (whose emission bands are at $\sim 400 \text{ nm}$), its appearance is indicative of the formation of some new luminescent species as a result of the prolonged electrical driving. Figure 6.8(c) shows normalized PL spectra of the same device before and after the electrical stress. The spectra are collected under excitation by a 365 nm illumination with a power density of $\sim 0.5 \text{ mW cm}^{-2}$. As TPBi absorbs negligibly little at this wavelength, the spectra represent PL from the CBP layer. As can be seen in the figure, the PL spectra show no changes due to the electrical stress, except for a very small spectral broadening at $\sim 500 \text{ nm}$. Since the EL originates primarily from the e-h recombination zone (i.e., the vicinity of the CBP/TPBi interface) whereas the PL originates from the entire CBP layer, the stark difference between the extent of changes in the EL and PL spectra suggests that the formation of the new luminescent species is limited mainly to the vicinity of the CBP/TPBi interface, where the density of both excitons and polarons is typically much higher. As

TPBi can diffuse easily into HMs during device electrical driving, the EL spectral shift may be due to emission from certain CBP-TPBi exciplex species, resulting from the intermixing of the two materials. To investigate this possibility, a device containing a mixed layer of CBP and TPBi was fabricated in order to test if simply mixing the two materials could result in a similar red-shift. The EL spectrum from the device does not however show any new long-wavelength band and is generally identical to that of the one without the mixed layer before the stress, ruling out the possibility that the new luminescent species may arise from CBP-TPBi exciplex.

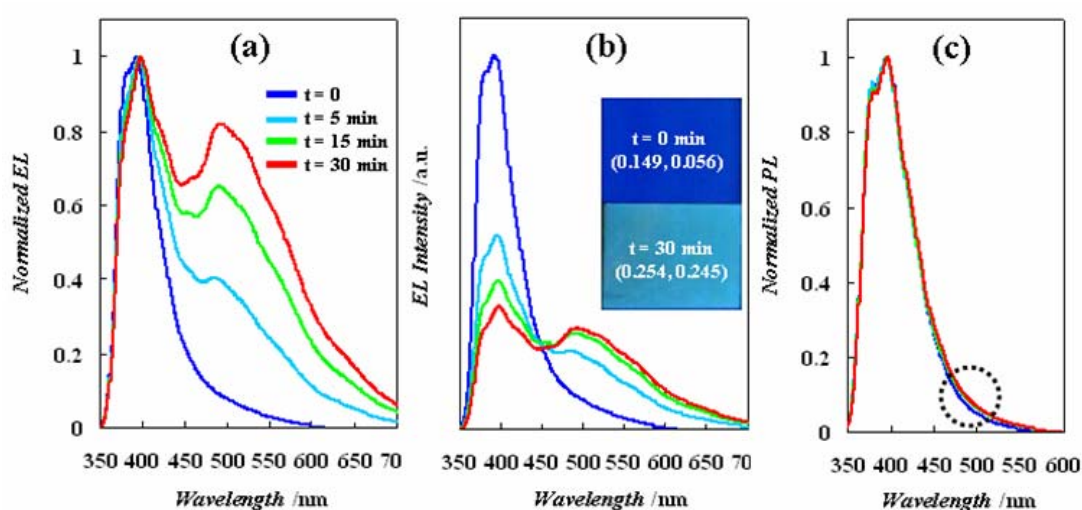


Figure 6.8: (a) EL (with normalization), (b) EL (without normalization) and (c) PL (with normalization) spectra with continuous electrical driving at 20 mA cm^{-2} in a device of structure ITO/MoO₃(5nm)/CBP(30nm)/TPBi(20nm)/LiF(0.5nm)/Al(100nm). Two photographs depicting the emission colors and corresponding CIE coordinates of the device before and after electrical driving are included in (b).

It is important to point out that the changes in EL spectra with electrical stress can be observed not only in devices with neat CBP, but also in regular devices where CBP is doped with a phosphorescent guest. Although obviously they will be difficult to detect in devices containing green-emitting dopants due to the spectral overlap between the dopants emission and this new band, they can be detected in devices with dopants emitting in the red range. Figure 6.9 shows normalized EL spectra with continuous electrical driving at 20 mA cm^{-2} in a PhOLED containing the red phosphorescent emitter platinum octaethylporphine (PtOEP) of structure ITO/MoO₃(5nm)/CBP(20nm)/CBP:PtOEP(2%)(20nm)/TPBi(30nm)/LiF(0.5nm)/Al(100nm). As the

figure shows, the device initially (at $t = 0$) produces a predominant amount of red EL from PtOEP triplets at ~ 650 nm, a small amount of blue EL from CBP singlets at ~ 400 nm and an extremely small amount of EL from a hot (or higher) level of thermally populated PtOEP triplet states with the little spike at ~ 545 nm.⁸³ After 10 hours of electrical driving, a new band at ~ 500 nm which precisely coincides with that in figure 6.8 appears, pointing to the formation of the same new luminescent species.

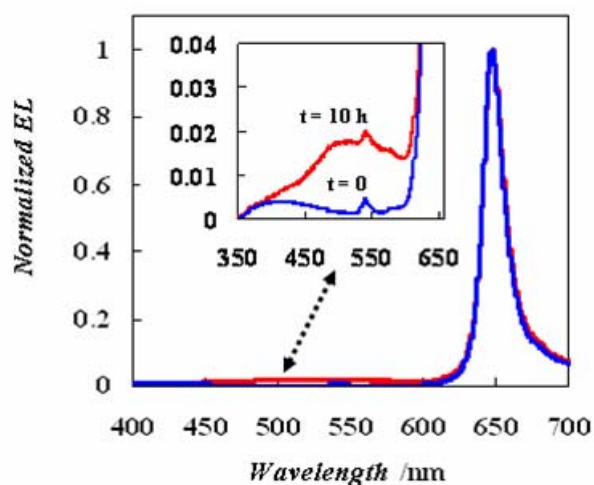


Figure 6.9: Normalized EL spectra of a device of structure ITO/MoO₃(5nm)/CBP(20nm)/CBP:PtOEP(2%)(20nm)/TPBi(30nm)/LiF(0.5nm)/Al(100nm) before and after 10 hours of electrical driving at 20 mA cm⁻². The inset shows a detailed view of the spectra in the short-wavelength region.

From the above results, the conclusion can be drawn that electrical driving results in EL spectral changes in CBP/TPBi based PhOLEDs, associated with the emergence of a new band at ~ 500 nm and independent of the guest materials. The reason that this phenomenon was never specifically reported in the past may be due to the difficulty in isolating this band in PhOLEDs containing green and blue emitters, due to the significant overlap in the EL spectra of these emitters and the new luminescent species. Since in these devices the majority of e-h recombination and exciton formation occurs on CBP molecules, rather than on TPBi or Ir(ppy)₃ molecules directly,⁸⁴ and takes place in the vicinity of the CBP/TPBi interface, it is entirely possible that the new luminescent species may be associated with or resulting from degraded CBP molecules near the interface.

The changes in EL spectra with electrical driving time, as a phenomenon, is known to occur in blue fluorescent OLEDs, and causes the loss in color purity in these devices with electrical aging in general. Our previous studies on anthracene-based blue fluorescent OLEDs uncovered that the effect is due to the formation of anthracene aggregates, which have a lower bandgap than the monomers and hence a longer wavelength.⁸⁵ Seeing a similar effect in CBP-based devices, it is wondered if a similar aggregation process, induced by electrical driving, occurs.

To test for this, changes in EL spectra of CBP/TPBi-based devices due to thermal annealing were first investigated. Figure 6.10(a) shows normalized EL spectra of a device of structure ITO/MoO₃(5nm)/CBP(40nm)/TPBi(30nm)/LiF(0.5nm)/Al(100nm) before and after annealing at 120 °C for 20 and 60 minutes in a N₂ atmosphere. As the figure shows, the initial (before annealing) EL spectrum corresponds to the typical CBP emission and is identical to that in figure 6.8(a). After 20 minutes of annealing, the spectrum shows slight broadening in the long-wavelength tail. This broadening becomes significant after 60 minutes of annealing. To better illustrate the changes, the differences between the EL spectra after 20 minutes and 60 minutes of annealing relative to the initial one are shown in the inset of the figure. The differences clearly correspond to a new band with a peak at ~ 500 nm. Quite remarkably, the changes in the EL spectra here induced by annealing are very similar to those induced by electrical driving in figure 6.8 (i.e., both correspond to a new band at ~ 500 nm), suggesting that the new luminescent species in both cases is likely the same. Since organic molecules in general tend to aggregate under thermal annealing to increase molecular ordering, it is possible that the new emission band may be due to CBP and/or TPBi aggregates.

To understand the origin of the new luminescent species, the effect of thermal annealing on the changes in PL spectra of CBP and TPBi films were further studied independently. Figure 6.10(b) shows normalized PL spectra under a 365 nm excitation of the CBP sample before and after annealing at 120 °C for 20, 60 and 100 minutes in a N₂ atmosphere. As the figure shows, the sample initially produces a PL spectrum of an amorphous CBP film. As the CBP sample is annealed over a period of 100 minutes, the PL spectrum starts to show increasingly distinguishable bands in the region of 350-450 nm. These bands can be attributed to the vibrational modes of CBP molecules, becoming increasingly resolvable as the film morphology changes gradually, by the annealing process, from an amorphous to a more crystalline one.⁸⁶ What is also shown in figure 6.10(b) is the PL spectral broadening in the 450-650 nm region after 60 and 100 minutes of annealing. The differences between the PL spectra after 60 minutes and 100 minutes of annealing relative to the initial one are

shown in the inset, again showing the emergence of a band with a peak at ~ 500 nm. Since the 500 nm band can be induced by just annealing, it is very likely that the new luminescent species is simply CBP aggregates. This is further verified by comparing the absorption spectra of the CBP film before and after the thermal annealing shown in figure 6.10(c). As the figure shows, the absorption spectrum of the annealed film shows a significant red-shift in the 300-400 nm region in comparison to that before annealing, which is consistent with the increased crystallinity (i.e., aggregation) in the bulk CBP film. Figure 6.10(d), on the other hand, shows normalized PL spectra under a 312 nm excitation of the TPBi sample due to thermal annealing at 150 °C in a N₂ atmosphere. Unlike CBP, TPBi shows no detectable changes in the PL spectra upon annealing for the same period of time, suggesting that TPBi is not as easily susceptible to aggregation.

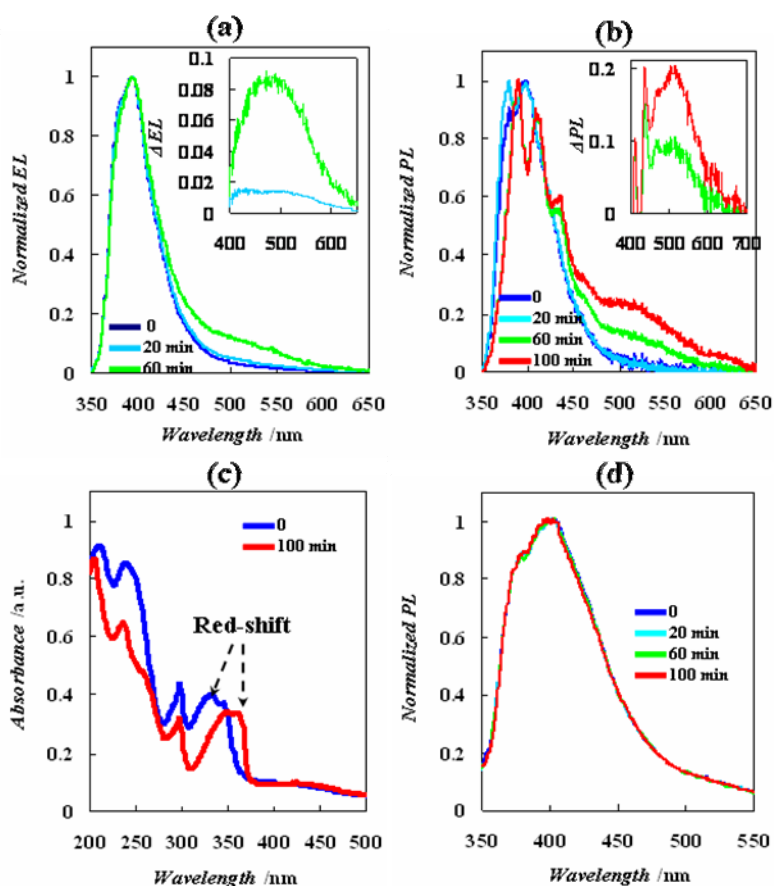


Figure 6.10: (a) Normalized EL spectra of a device of structure ITO(120nm)/MoO₃(5nm)/CBP(40nm)/TPBi(30nm)/LiF(0.5nm)/Al(100nm) before and after

annealing at 120 °C for 20 and 60 minutes in a N₂ atmosphere. The inset shows the differences between the EL spectra after 20 minutes and 60 minutes of annealing relative to the initial one. (b) Normalized PL spectra under a 365 nm excitation of a CBP film before and after annealing at 120 °C for 20, 60 and 100 minutes in a N₂ atmosphere. The inset shows the differences between the PL spectra after 60 minutes and 100 minutes of annealing relative to the initial one. (c) Absorption spectra of a CBP film before and after 100 min of annealing at 120 °C. (d) Normalized PL under a 312 nm excitation of a TPBi film before and after thermal annealing at 150 °C.

The results convincingly prove that the emergence of the new 500 nm band in the EL spectra due to electrical driving arise essentially from CBP aggregation. It is worthwhile to point out that such aggregation process occurs primarily in the e-h recombination zone (i.e., near the CBP/TPBi interface), and not in the entire CBP layer, since the EL spectrum changes significantly whereas the PL spectrum changes negligibly as noted earlier in figure 6.8.

Although the results above show the occurrence of CBP aggregation in PhOLEDs with time when under electrical driving, they do not reveal its underlying process. Considering that a similar aggregation phenomenon can be induced by thermal annealing alone, it is natural to wonder if PhOLEDs degradation is simply due to CBP aggregation induced by Joule heating arising from the current flow during device operation.⁸⁷ Therefore, to uncover the exact mechanism, the degradation behavior of the CBP/TPBi interface was studied under various stress scenarios utilizing hole-only (h-only) devices. The structure of the devices is ITO/MoO₃(5nm)/CBP(30nm)/TPBi(10nm)/MoO₃(10nm)/Al(100nm), as shown in **figure 6.11(a)**. When under a forward bias (i.e., the ITO is positively biased relative to the Al), the injection of electrons from the Al is blocked by the top MoO₃, and therefore the flow of current occurs exclusively by holes injected from the ITO. As a result, these devices show h-only transport characteristics. Figure 6.11(b) shows the changes in V_d (ΔV) driven by a current of density 20 mA cm⁻² in these devices versus time, during which the devices are subjected to one of three stress scenarios: (1) Current flow only (denoted by <I only>), under a forward bias to sustain a current flow of density ~20 mA cm⁻²; (2) Irradiation by light only (denoted by <L only>), at 365 nm of power density ~0.5 mW cm⁻²; (3) Current flow and irradiation together (denoted by <I + L>), subjected to scenarios (1) and (2) simultaneously. Also, a control device was kept in the dark to be used as a reference (denoted by <C>). The temperature of these devices is maintained at ~ 22 °C. For

comparison, traces representing the algebraic sum of the ΔV values caused by the scenarios $\langle I \text{ only} \rangle$ and $\langle L \text{ only} \rangle$ (denoted by $\Sigma(\langle I \text{ only} \rangle, \langle L \text{ only} \rangle)$) were also included. As figure 6(b) shows, the flow of current alone or irradiation alone brings about an increase in the V_d with time, reflected in the ΔV values in the figure, which can be attributed to the hole accumulation at the CBP/TPBi interface and the photo-degradation of the ITO/MoO₃/CBP contact, respectively. What is most significant in the figure, however, is that the measured ΔV values due to the scenario $\langle I + L \rangle$ are not only much higher than those due to the scenarios $\langle I \text{ only} \rangle$ or $\langle L \text{ only} \rangle$, but are also much higher than the corresponding computed $\Sigma(\langle I \text{ only} \rangle, \langle L \text{ only} \rangle)$ values (i.e., the sum of the ΔV values due to the scenarios $\langle I \text{ only} \rangle$ and $\langle L \text{ only} \rangle$). Such additional increase in V_d exhibited in the scenario $\langle I + L \rangle$ is essentially indicative of the degradation of the CBP/TPBi interface, and is determined to be due to interactions between CBP excitons and CBP positive polarons in its vicinity.

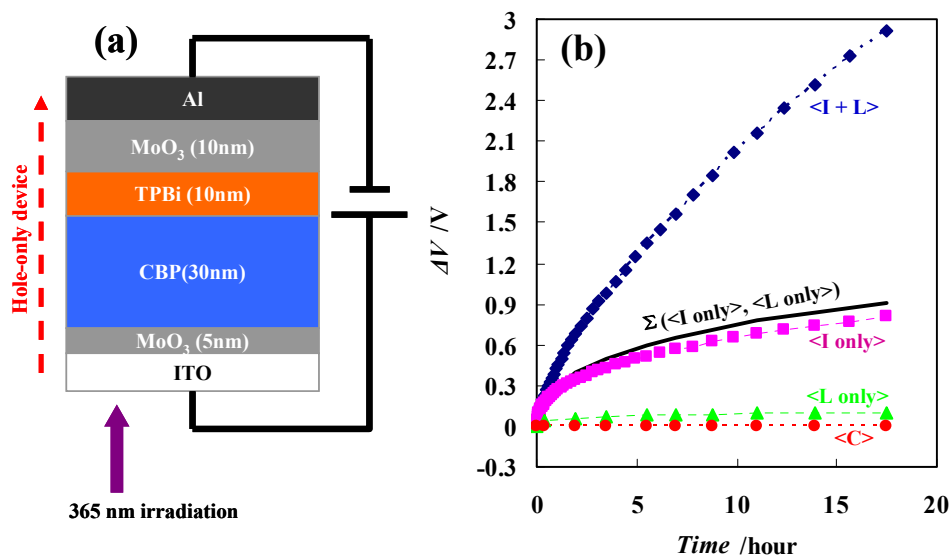


Figure 6.11: (a) H-only devices of structure ITO/MoO₃(5nm)/CBP(30nm)/TPBi(10nm)/MoO₃(10nm)/Al(100nm). (b) Changes in V_d (ΔV) driven by a current of density 20 mA cm^{-2} in the devices versus time, during which these devices are subjected to scenarios $\langle I \text{ only} \rangle$, $\langle L \text{ only} \rangle$ and $\langle I + L \rangle$ and kept in the dark (i.e., $\langle C \rangle$). Traces representing the algebraic sum of the ΔV values caused by the scenarios $\langle I \text{ only} \rangle$ and $\langle L \text{ only} \rangle$ (denoted by $\Sigma(\langle I \text{ only} \rangle, \langle L \text{ only} \rangle)$) is also included.

After ~ 18 hours under the above conditions, the Al cathodes of the four devices were peeled off using a scotch tape in a N₂ atmosphere. Since the adhesion of inorganic/inorganic interfaces is much stronger than that of organic/inorganic interfaces,⁵⁴ the 10 nm MoO₃ layer would also be peeled off with the Al cathode. LiF(1nm)/Al(100nm) cathodes were then deposited on these devices. As now, electron injection from the Al cathode becomes possible, and hence bipolar transport and EL become possible. The process is illustrated in **figure 6.12(a)**, in which these h-only devices are converted to light-emitting devices by cathode replacement. Figure 6.12(b) presents the normalized EL spectra of these devices, showing blue EL from CBP. Remarkably, as the inset more clearly illustrates, the device subjected to the scenario <I + L> shows a broader EL spectrum than the devices subjected to the scenarios <I only> and <L only> and kept in the dark. Figure 6.12(c) displays the “spectral shift” observed in the devices subjected to the scenarios <I + L>, <I only> and <L only>, obtained from the mathematical difference in the EL spectra of the three devices after the aging relative to the control one. As figure 6.12(c) shows, only the device subjected to the scenario <I + L> shows a significant change in the EL spectrum relative to the control one, and the difference corresponds to a band with peak at ~ 500 nm. Given the obvious similarity between this band and the corresponding one in figure 6.8 to 6.10, it can be ascribed to the formation of CBP aggregates. The difference in the spectra of the device subjected to the scenario <I + L> and those subjected to <I only> or <L only> rules out the possibility that the aggregation may be due to Joule heating, and indicate that it must be due to the co-existence of both CBP excitons and CBP positive polarons (i.e., due to exciton-polaron interactions). This shows that exciton-polaron interactions can induce aggregation in CBP, similar to that induced by thermal annealing. Given the fact that both CBP excitons and CBP positive polarons are present simultaneously in high concentrations in the e-h recombination zone (i.e., the vicinity of the CBP/TPBi interface) in PhOLEDs during normal operation, the same effect can take place. Thus, it may be concluded that the changes in the EL spectra of PhOLEDs with electrical driving time observed in figure 6.8 and 6.9 are the result of CBP aggregation in the recombination zone due to exciton-polaron interactions. Since this aggregation process is triggered by the co-existence of both excitons and positive polarons, but not by the presence of excitons or polarons separately, it is exciton-polaron-induced aggregation (EPIA) in nature. It should be pointed out that the co-existence of excitons and negative polarons on CBP does not lead to a similar EPIA effect, since only positive polarons were found to interact with excitons and lead to the observed degradation whereas negative polarons were not. This exactly corresponds to the scenario in PhOLEDs during operation where the CBP polarons that accumulate in the vicinity of the CBP/TPBi interface are mostly positive.

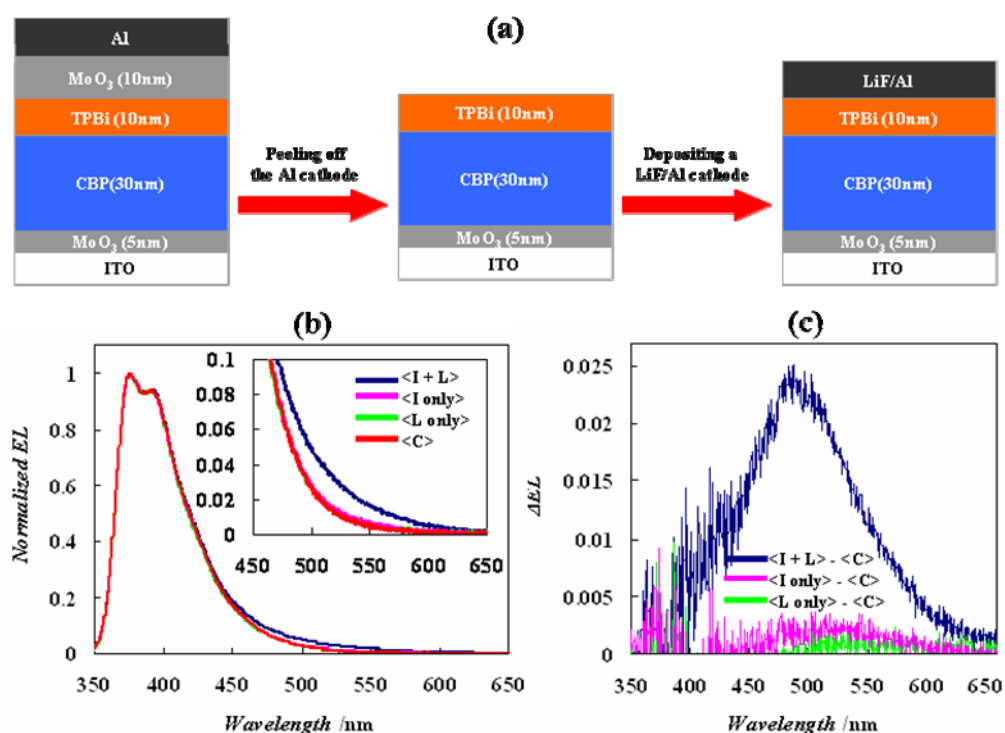
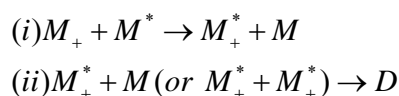


Figure 6.12: (a) Illustration of the cathode replacing process, in which h-only devices are converted to light-emitting devices. (b) Normalized EL spectra of the four light-emitting devices. The inset shows a detailed view of the spectra at ~500 nm. (c) Differences between the EL spectra of the devices subjected to the scenarios <I + L>, <I only> and <L only> relative to that of the control device.

Finding CBP aggregation due to exciton-polaron interactions, the underlying mechanism can be described by the following two-step general scheme:



where M_+ represents positive polarons on CBP monomers, M^* represents excitons of CBP monomers, M_+^* represents excited positive polarons on CBP monomers (i.e., excited CBP cations), M represents CBP monomers in the ground state and D represents CBP aggregate species (e.g., a dimer) in the ground state. When a PhOLED is driven by a current, both CBP positive polarons and CBP excitons will co-exist in high concentrations in the vicinity of the CBP/TPBi interface. An energy transfer between these two species can lead to the formation of a CBP excited positive polaron

state, described in step (i). Since this state has an electron in a high energy level (i.e., the LUMO) and at the same time has an unoccupied HOMO, it can be expected to be particularly prone to intermolecular aggregation in order to reach a more energetically favorable state, described in step (ii). These CBP aggregates will have narrower bandgap than their monomer precursors and produce EL at longer wavelength. They will also be capable of trapping charges and quenching excitons, and thus lead to an increase in V_d and a decrease in EL efficiency, which are all common observations associated with PhOLEDs degradation. As the EPIA process takes place mainly in the vicinity of the CBP/TPBi interface (where most e-h recombination and EL originates in PhOLEDs), this degradation mechanism occurs primarily at the interface.

In order to verify that these changes are morphological in nature, and to rule out chemical degradation, NMR spectroscopy was used to analyze the molecular structure of CBP aggregates. The experimental details and data are provided in detail in the supplementary material section. The NMR results show no detectable changes in the chemical fingerprint of CBP when subjected to electrical driving, verifying that the degradation mechanism is exclusively morphological (i.e., aggregation) in nature.

Uncovering EPIA in CBP, it becomes interesting to see if the same phenomenon occurs in other materials. Similar studies were therefore conducted on a range of materials, some of which are commonly used as hosts in PhOLEDs. These materials are Spiro-CBP, TAPC, mCP, TCTA, TBADN, NPB and Spiro-NPB, and their molecular structures are shown in **figure 6.13** (CBP is also included for comparison). **Figure 6.14(a)-(e)** show EL spectra (without normalization) with continuous electrical driving at 20 mA cm⁻² in devices of general structure ITO/MoO₃(5nm)/X(30nm)/TPBi(30nm)/LiF(0.5nm)/Al(100nm), where X is CBP, Spiro-CBP, TAPC, mCP or TCTA. As can be seen from the figures, the EL spectra of all devices change gradually upon electrical driving, all displaying a decrease in intensity of the monomer emission peak, and the emergence of a new band at longer wavelength which can be attributed to the formation of aggregate species of these materials. Clearly, all materials are susceptible to aggregation by exciton-polaron interactions, similar to CBP, but in various extents. As all these materials have wide bandgap (> 3.3 eV), a typical request of HMs in PhOLEDs, materials with relatively narrower bandgap were also tested for comparison. **Figure 6.14(f)-(h)** show EL spectra (without normalization) with continuous electrical driving of devices with the same structure but with TBADN, NPB and Spiro-NPB, respectively. The normalized EL spectra are illustrated in the insets. Clearly, the extent of

aggregation even after much longer periods of electrical driving time is much less in comparison to that in the wide-bandgap materials.

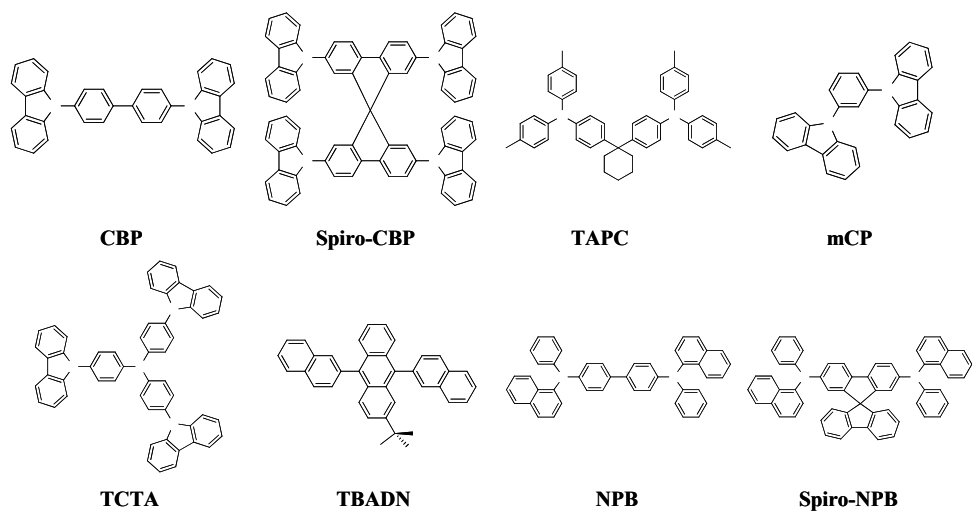


Figure 6.13: Molecular structures of a range of wide-bandgap organic materials.

N

N

N

N

N

N

N

N

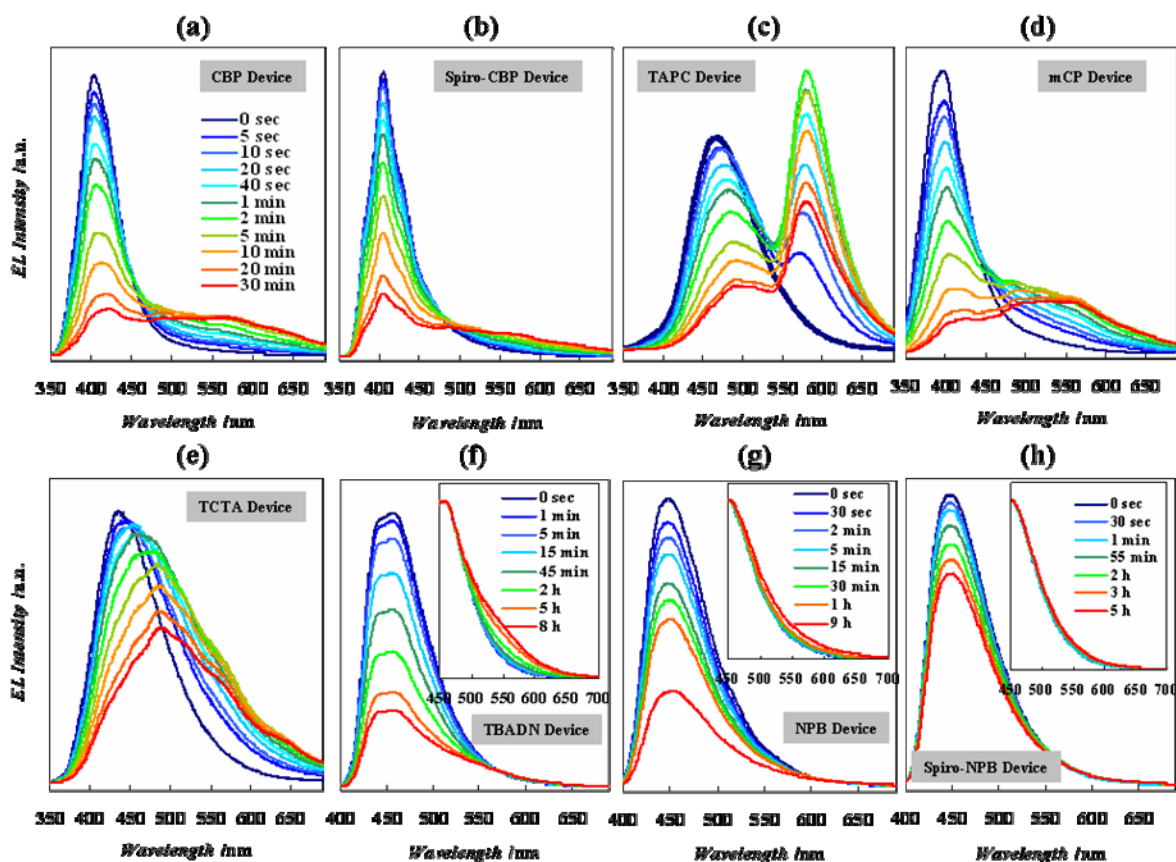


Figure 6.14: EL spectra (without normalization) with continuous electrical driving at 20 mA cm^{-2} in devices of general structure ITO/MoO₃(5nm)/X(30nm)/TPBi(30nm)/LiF(0.5nm)/Al(100nm), where X is CBP, Spiro-CBP, TAPC, mCP, TCTA, TBAND, NPB or Spiro-NPB.

Figure 6.15(a) depicts the extent of EPIA in the above materials (defined as the ratio of aggregate emission band intensity to monomer emission band intensity in the EL spectra after 30 minutes of electrical driving) versus their bandgap (i.e., E_g) (taken from refs [88,89,90]). As the figure shows, there is a clear correlation between the extent of aggregation and E_g , where the wide-bandgap materials (such as TAPC, mCP TCTA, CBP and Spiro-CBP) tend to aggregate more significantly in comparison to the narrow-bandgap ones (such as TBADN, NPB and Spiro-NPB). This can be attributed to the fact that in wide-bandgap materials excitations involved in exciton-polaron interactions have higher energy, and thus can induce aggregation more efficiently (e.g., excited polaron species will be more energetic). Quite interestingly, there seems to be a threshold E_g value of

~ 3.1 eV. When below the threshold, the materials aggregation occurs slowly, whereas when above it, the materials aggregation occurs significantly (with the aggregate to monomer EL bands ratio at least one order of magnitude higher). Surprisingly, there seems to be no correlation between the ease of aggregation and the materials glass-transition (T_g) temperatures (taken from refs [91,92,93,94,95,96,97]), as shown in figure 6.15(b). This again points to the fact that the root cause of this aggregation in PhOLEDs during electrical driving is fundamentally different and is not simply Joule heating.

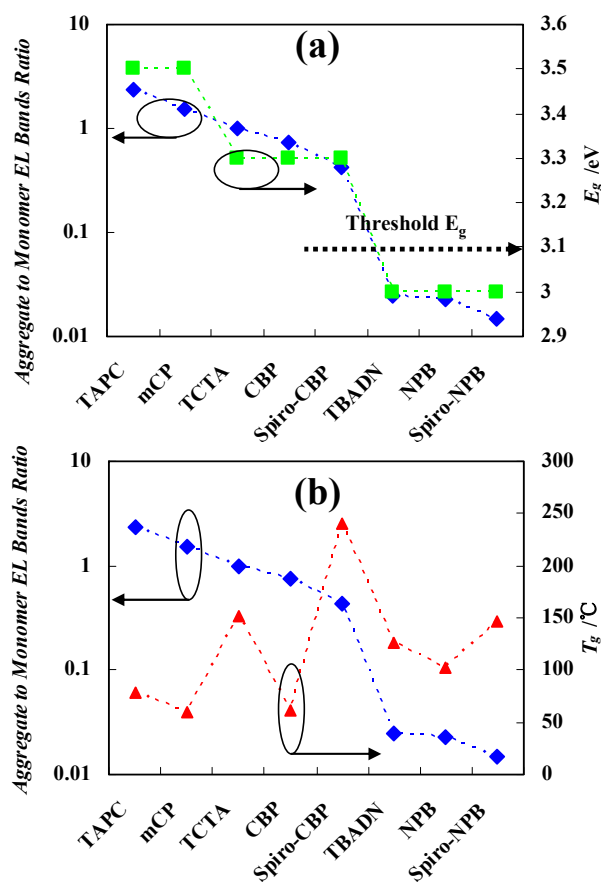


Figure 6.15: Ratio of aggregate/monomer EL bands versus the materials (a) E_g and (b) T_g temperatures.

These findings uncover a new degradation mechanism based on EPIA of organic materials that severely affects wide-bandgap materials. As PhOLEDs generally use wide-bandgap hosts, this may explain the generally lower stability of PhOLEDs relative to their fluorescent counterparts.

In conclusion, the degradation mechanisms of PhOLEDs were studied. Contrary to expectations, it is found that PhOLEDs degradation is not induced by guest excitons, but is related to the presence of host excitons that causes device degradation via exciton-polaron interactions. It is determined that the degradation arises from HMs aggregation in the vicinity of EML/ETL interfaces. Further study reveals that such aggregation process is induced by the co-existence of both excitons and positive polarons on HMs. Such aggregation process is found to occur in a variety of wide-bandgap materials commonly used as hosts in PhOLEDs and is correlated with device degradation. Quite notably, the extent of aggregation appears to correlate with the materials bandgap rather than with their T_g temperatures. The findings uncover a significant degradation mechanism in PhOLEDs that is exciton-polaron-induced and interfacial in nature. Although this study has focused on PhOLEDs, the same degradation mechanism can be expected to affect other organic optoelectronic devices such as organic solar cells and organic photodetectors.

6.2.2 Different Influence of Singlet and Triplet Excitons in EPIA

This previously unknown molecular aggregation behavior, EPIA, is induced by interactions between excitons and positive polarons that reside on host molecules during electrical driving and affects wider bandgap (E_g) materials more significantly. However, whether the excitons involved in driving this aggregation mechanism are mostly singlets or triplets has remained unclear.

The degradation behavior of PhOLEDs with various concentrations of Ir(piq)₃ or PtOEP as guest materials was first studied. The general structure of the devices is ITO(120 nm)/MoO₃(5 nm)/CBP(20 nm)/CBP:Guest(1.5 or 5% by volume, 20 nm)/TPBi(30 nm)/LiF(0.5 nm)/Al(100 nm). **Figure 6.16** shows EL intensity (normalized to the initial values) and ΔV (defined as the driving voltage, V_d , at the given time minus the initial value) versus time during which these devices are driven by a constant current of density 20 mA/cm². The initial brightness values of the devices containing 1.5% PtOEP, 5% PtOEP, 1.5% Ir(piq)₃ and 5% Ir(piq)₃ are 170, 260, 2200 and 1800 cd/m², respectively. The initial V_d values of these devices are 7.8, 8.4, 8.1 and 8.0 V, respectively. As the figure shows, the Ir(piq)₃ devices exhibit much higher EL stability (longer device lifetime) relative to the PtOEP devices, despite the fact that the devices utilize the same host and charge transport materials, reflecting the strong dependence of device stability on the guest material species. Although the initial brightness of the Ir(piq)₃ devices is significantly higher than that of the PtOEP devices, their stability is also higher, contradicting the commonly accepted notion that the rate of device degradation is proportional to its initial brightness. Considering that Ir(piq)₃ and PtOEP are both red emitters with

very similar energy gap,^{13,98} the significant difference in device stability is somewhat surprising, especially that red phosphorescent guests are perceived to be very stable in general.³³ Moreover, as shown in the figure, for the devices with the same guest, an increase in guest concentration (e.g. from 1.5% to 5%) leads to an increase in device lifetime. This also cannot be explained by previous suggestions that the EL loss is mainly due to molecular decomposition/dissociation of the guest materials.³¹

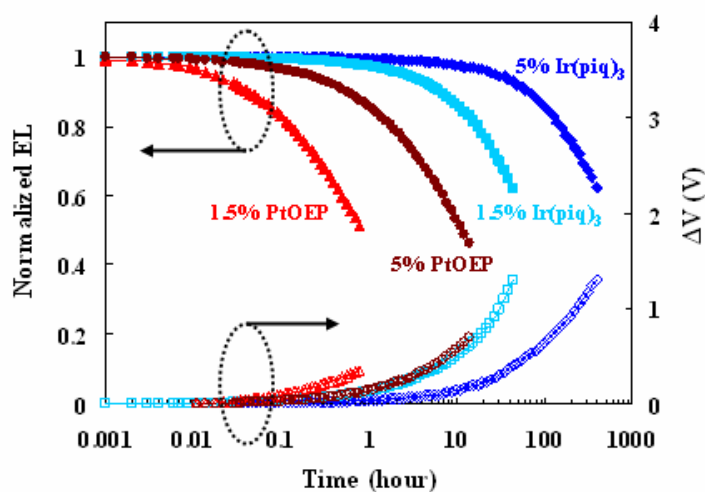


Figure 6.16: EL intensity (normalized to initial values) and ΔV versus time during which PhOLEDs containing $\text{Ir}(\text{piq})_3$ and PtOEP as guests are driven by a constant current of density 20 mA/cm^2 .

The observations are however consistent with our recent findings that PhOLED degradation is primarily caused by the EPIA of the wide-Eg hosts (i.e. the CBP host in this case). **Figure 6.17** shows EL spectra (normalized to the peak EL intensities of the guests) of the devices in figure 6.16 collected before (i.e. from the fresh devices) and after the electrical stress (i.e. after the device EL has decreased to 70 % of its initial value). Clearly, the spectra correspond to the characteristic luminescence spectra of the guest materials $\text{Ir}(\text{piq})_3$ (i.e. figure 2(a)-(b)) and PtOEP (i.e. figure 2(c)-(d)). A closer examination of the spectra (the enlarged spectra in the insets) however reveals a small amount of blue EL from CBP singlets with a peak at $\sim 400 \text{ nm}$ in all devices and, in case of the PtOEP devices, an additional smaller band at $\sim 545 \text{ nm}$ which can be attributed to EL from higher level of thermally populated PtOEP triplet states. What is however more remarkable is that all the devices show some spectral change after the electrical stress (can be seen in the differences between the red

and black traces in the insets). For example, the 5% Ir(piq)₃ device exhibits very small (but detectable) spectral changes after 260 hours of aging, whereas the 1.5% Ir(piq)₃, 5% PtOEP and 1.5% PtOEP devices show more significant spectral changes after only 31, 3.4 and 0.25 hours of aging, respectively. As the insets show, the spectral changes mainly occur in the 400-600 nm region, and correspond to the emergence of a new band with a peak at ~ 500 nm, which can be attributed to emission from CBP aggregates as a result of the EPIA process. It should be pointed out that the CBP aggregation also occurs in PhOLEDs containing green and blue emitters. Detecting them is however more difficult in this case because of the overlap of the aggregate luminescence with luminescence from the green/blue emitters. This is the main reason for using red emitters as the guest materials in this study. **Figure 6.18** shows a plot of device lifetime (defined here as the time elapsed until the EL decreases to 70 % of its initial value) versus the host aggregation rate (defined as the intensity of the host aggregate emission band in the EL spectra divided by the time of electrical driving elapsed, which approximately reflects how fast the host EPIA takes place in the devices). As the figure shows, there is a clear correlation between the two attributes where devices with shorter lifetimes have higher host aggregation rates, indicating that device EL degradation is indeed closely linked with the host EPIA rate. In this regard, the differences in the lifetimes in figure 6.16 can be attributed to different host EPIA rates in the different devices. Therefore, the device degradation behavior exhibited in figures 6.16 and 6.17 can be primarily attributed to host EPIA.

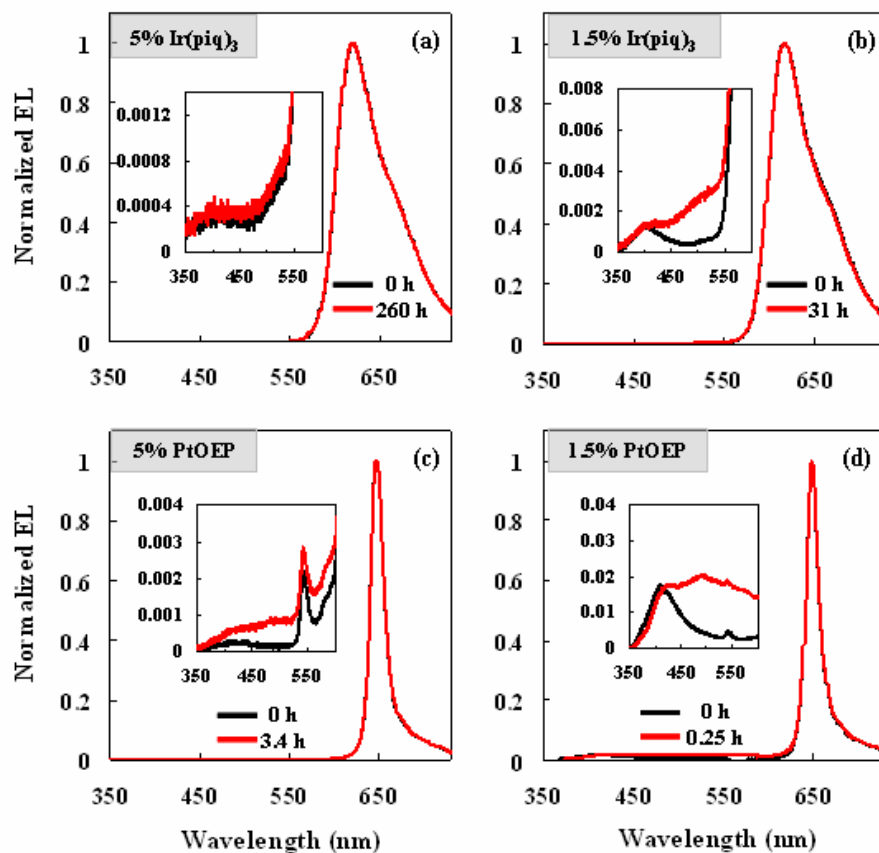


Figure 6.17: EL spectra of the devices containing (a) 5% Ir(piq)₃, (b) 1.5% Ir(piq)₃, (c) 5% PtOEP, (d) 1.5% PtOEP collected before (i.e. from the fresh devices) and after the electrical stress. The insets show amplified EL spectra in the shorter-wavelength region, showing emission from CBP monomers at ~ 400 nm, CBP aggregates at ~ 500 nm and a higher level of thermally populated PtOEP triplet states with the little spike at ~ 545 nm (in the PtOEP devices only).

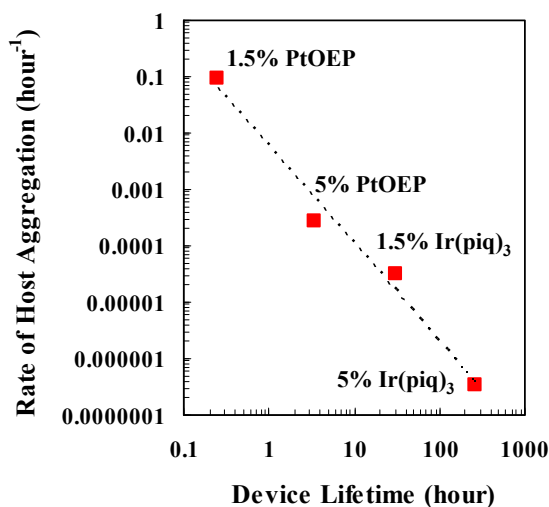


Figure 6.18: A plot of device lifetime versus rate of host aggregation.

In general, both singlet and triplet excitons are present in high concentrations in the devices during operation. In order to determine if one of the two types of excitons plays a more significant role in the observed EPIA and PhOLED degradation, the effect of singlet excitons was first studied. As host singlets dissipate their energy radiatively in general, EL from the host was first studied to estimate the relative amounts of host singlets present in the various devices when under electrical driving and see if they may correlate with device stability. **Figures 6.19(a)-(d)** show EL spectra (normalized to the peak EL intensities of the guests) collected from the fresh devices in figure 6.16 driven at current densities of 20, 2 and 0.2 mA/cm². All these spectra correspond to EL from the guest materials. A closer examination of these spectra however reveals that some emission from the CBP host is present, as can be seen from the enlarged spectra in the insets of these figures, showing CBP EL bands with peaks at ~ 400 nm. As the current density increases, the emission from the CBP host relative to that from the guests increases, indicating that host to guest energy transfer is not complete, hence a population of residual CBP host singlets (i.e. unquenched by the guest) is present in the devices when driving currents typical of those used in normal device operation are used.

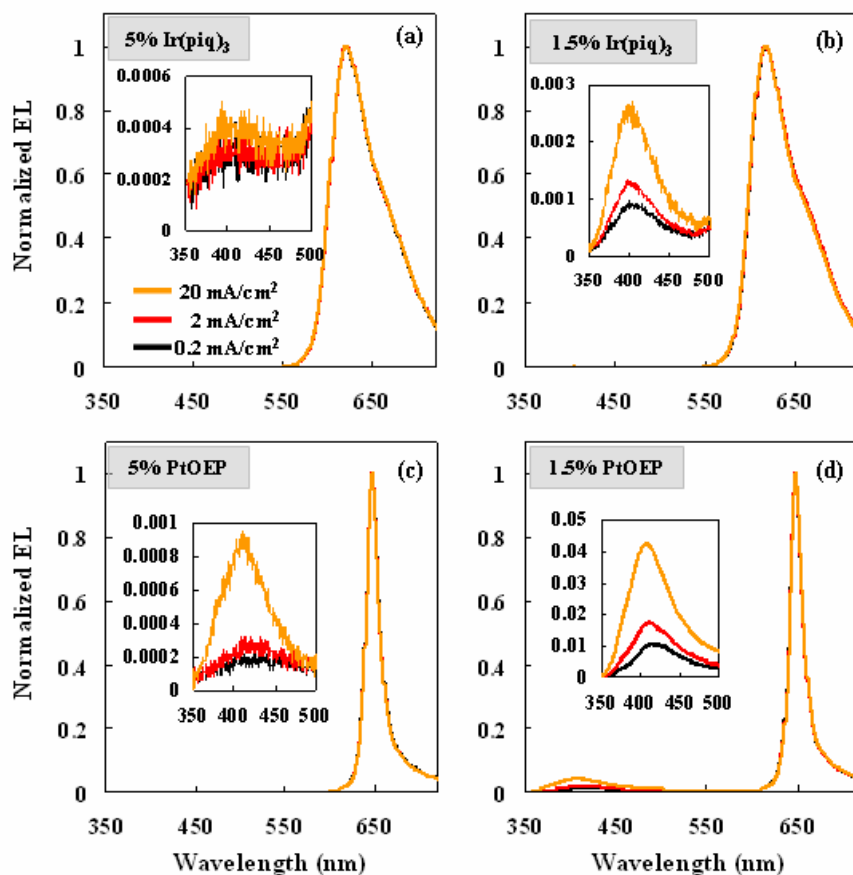


Figure 6.19: EL spectra (normalized to peak intensities) collected from the fresh devices containing (a) 5% Ir(piq)₃, (b) 1.5% Ir(piq)₃, (c) 5% PtOEP, (d) 1.5% PtOEP driven at current densities of 20, 2 and 0.2 mA/cm². The insets show amplified spectra in the short-wavelength region.

Figures 6.20(a) and (b) depict device lifetime and V_d stability (defined as the time elapsed before the V_d increases by 0.3 V relative to its initial value), respectively, versus host to guest EL bands ratio (i.e. the ratio of the product of integrating the host emission band intensity to the product of integrating the guest emission band intensity in the EL spectra, which approximately mirrors the relative populations of host singlet excitons to guest excitons in the devices). The device lifetime and V_d stability values are based on the data in figure 6.16, whereas the host to guest EL bands ratio is obtained from the EL spectra (at 20 mA/cm²) in figure 6.19. As figures 6.20(a) and (b) show, there is a clear correlation between the extent of device degradation (i.e. changes in EL and V_d) and the

relative population size of host singlets in the devices, where the devices containing more residual host singlets tend to degrade more rapidly under the same electrical stress. The results therefore suggest that singlet excitons can be inducing the EPIA process that leads to device degradation.

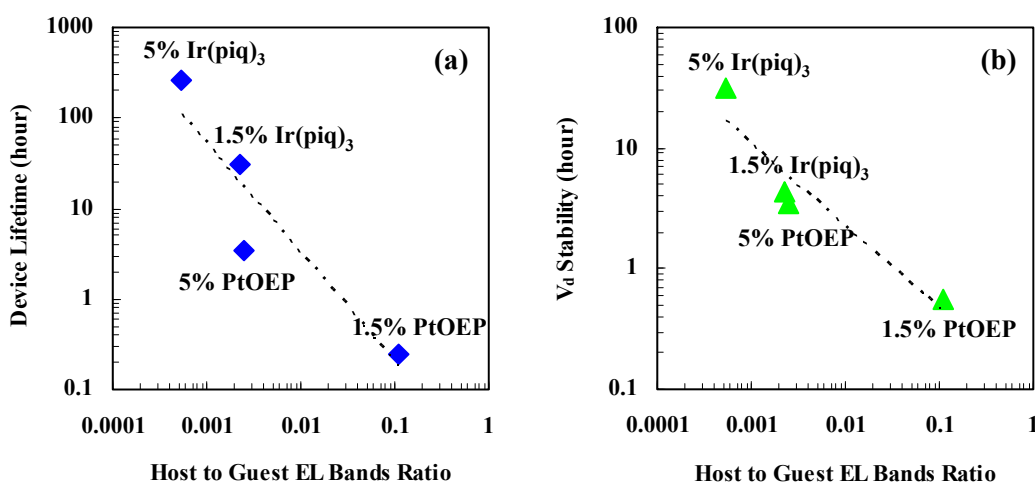


Figure 6.20: A plot of (a) Device lifetime and (b) V_d stability versus host to guest EL bands ratio.

Seeing that a clear correlation exists between device degradation rate and the number of host singlet excitons, the differences in device stability when using Ir(piq)₃ versus PtOEP can be attributed to the different phosphorescence lifetimes of these two guest materials. **Figures 6.21(a)** and (b) show phosphorescence versus time at 620 nm and 650 nm (i.e. from the radiative relaxation of Ir(piq)₃ and PtOEP triplet states, respectively) collected from the fresh devices shown in figure 6.16 excited by a 379 nm laser pulse (pulse width ~ 71 ps, average power ~ 5 mW). Clearly, the triplet lifetime of Ir(piq)₃ (defined as the time elapsed before the phosphorescence decays to 1/e or 36.8% of its initial value) is ~ 1 μs, whereas that of PtOEP is ~ 100 μs, approximately two orders of magnitude higher. As energy transfer from a donor to an acceptor requires that the acceptor molecule must initially (i.e. prior to the energy transfer step) be in the ground state, materials with shorter-lived excited states will be more efficient in accepting energy from donors in conditions where there is a continuous supply of excitation energy to the system (i.e. as in OLEDs). Therefore, when the CBP singlets are present in high concentration in the electron-hole recombination zone in the operating devices, the Ir(piq)₃ guest molecules can be expected to be capable of quenching the CBP singlets, via host-to-guest Forster energy transfer, more efficiently than PtOEP guest molecules. As a result, the population of CBP singlets will be smaller in case of the Ir(piq)₃ devices. This conclusion is also consistent with the

observations (in figure 6.19) that EL from CBP singlets is relatively less in case of the Ir(piq)₃ devices.

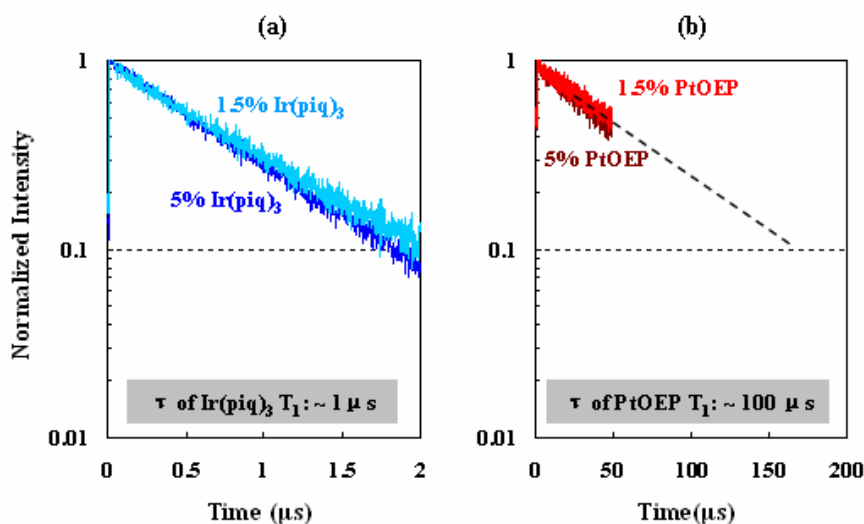


Figure 6.21: Phosphorescence versus time at (a) 620 nm (i.e. from the relaxation of Ir(piq)₃ triplet states) and (b) 650 nm (i.e. from the relaxation of PtOEP triplet states) collected from the fresh devices shown in figure 1 excited by a 379 nm laser pulse.

Based on the results above, a correlation was found between the device lifetimes and the relative population size of host singlets present in the devices. Given our recent findings that EL degradation in devices utilizing wide E_g hosts, including CBP, is caused primarily by EPIA of the host material, it may be concluded that singlet excited states on the host have a major influence in host EPIA that leads to device degradation.

The attention is now turned to triplet excitons to see if, like in the case of singlet excitons, there may be a correlation between their concentration on one hand and the EPIA rate and device degradation on the other. Unlike host singlets whose relaxation are radiative and can be detected directly, for example, in device prompt EL (despite that the majority is quenched by energy transfer to the guest molecules), host triplet excited states are typically non-radiative and hence their presence in devices is more difficult to detect directly. A technique based on measuring the delayed EL of the devices is therefore utilized as a way to estimate the relative concentration of host triplets in the devices. Delayed EL measurements are extensively used and clearly described in detail in our previous works.^{37,99,100} In this technique, the devices are subjected to a forward bias pulse (i.e., the

anode is positively biased relative to the cathode) of 8 V in magnitude and 0.5 ms in width, which is sufficiently long for prompt EL to reach its steady-state intensity. When the forward bias is removed, delayed EL will be collected after a time delay of 0.5 ms, much longer than the lifetime of singlet states. In addition, as such 0.5 ms time delay is much longer than the triplet lifetimes of the phosphorescent guests, the only species present in the emitter layer of devices that can lead to delayed EL will be the long lived host triplets and/or any un-recombined (i.e. residual) trapped charges. These two species (i.e. host triplets and trapped charges) can produce delayed EL via one or several of the following processes: (1) delayed recombination of these de-trapped charges, (2) slow migration of the host triplets to the vicinity of guest molecules via Dexter energy transfer, and (3) triplet-triplet annihilation (TTA), in which two host triplets interact upon collision to produce one host singlet that can transfer its energy to an adjacent guest molecule by Forster process. All these processes can subsequently contribute to delayed EL from guest molecules. It should be noted that delayed EL from the relaxation of host singlets produced by process (3) will generally be insignificant in case of host:guest systems as the majority of the produced host excitons will be transferred to the narrower- E_g guest material.

Figures 6.22(a)-(d) show delayed EL signals (black curves) collected from the devices with 5% Ir(piq)₃, 1.5% Ir(piq)₃, 5% PtOEP and 1.5% PtOEP, respectively, versus time elapsed, where time 0 on the x-axis corresponds to 0.5 ms after the end of the forward bias pulse. The insets of figures 6.22(a) and (c) present delayed EL spectra of the devices, confirming that the delayed EL corresponds to emission from emitter guests primarily. As can be seen from the figures, the four devices produce detectable delayed EL with an intensity that decreases with time. To identify the origin of the delayed EL signals, a 200 μ s reverse bias pulse (with a magnitude of 2, 5 or 8 V) is applied to the devices during the signal collection. The subsequent changes in the delayed EL signals observed upon the application of such reverse bias are recorded, as presented by the colored traces in figure 6.22. As the figures show, the application of a reverse bias causes a sudden increase (i.e. a spike) in the delayed EL. These spikes arise from sudden recombination of residual charges, which were earlier possibly trapped on the guest molecules, then get quickly de-trapped and re-distributed by the reverse bias, giving them the opportunity to recombine and produce EL. What is more notable however is the different delayed EL features observed at the end of the reverse bias pulse. In case of the Ir(piq)₃ devices (figures 6.22(a) and (b)), the delayed EL intensity recovers, at least partially, at the end of the reverse bias. This behavior is indicative of the presence of significant TTA (i.e. process (3)), as the collision/fusion of two host triplets leads to the formation of a singlet intermediate that can be easily

dissociated (and hence quenched) by the reverse bias electric field.³⁷ Since this electric field-quenching mechanism stops when the field vanishes, the delayed EL intensity increases again when the reverse bias pulse ends. (Note: triplets cannot be easily dissociated by the electric field due to their relatively larger binding energy, and hence are much less susceptible to this quenching mechanism. The dissociation of triplets via charge transfer to other molecules is also limited due to the absence of significant offsets in highest occupied molecular orbital and/or lowest unoccupied molecular orbital levels.) The unrecoverable part at the end of the reverse bias is however indicative of delayed EL arising from the recombination of de-trapped charges (i.e. process (1)), as the charges are swept out of the devices by the reverse bias. The results therefore suggest that the delayed EL in the Ir(piq)₃ devices arises from both TTA and the recombination of de-trapped charges. It should be pointed out that the recovery in the delayed EL of the 1.5% Ir(piq)₃ device when a reverse bias of 2V is used is almost complete, as shown in the inset of figure 6.22(b). The recovery however becomes increasingly incomplete as the magnitude of the reverse bias increases. This effect is attributed to the increasingly higher spikes at the beginning of the reverse pulse whose long-lasting effect may interfere with the recovery behavior.

In the case of the PtOEP device, on the other hand (figures 6.22(c) and (d)), the delayed EL intensity does not recover at all at the end of the reverse bias. Such behavior suggests that the delayed EL in the PtOEP devices arises almost exclusively from the recombination of residual trapped charges. The fact that the height of the delayed EL spike at the beginning of the reverse bias pulse is much lower suggests that the charges are more strongly trapped in case of the PtOEP devices and thus require higher reverse fields to become de-trapped. The PtOEP devices can be therefore expected to have a much larger population of trapped charges. Since trapped charges are very efficient in quenching triplet excitons, the population of host triplet excitons can be expected to be much smaller in case of the PtOEP devices. This argument is also fully supported by the absence of the host-host TTA fingerprint (i.e. the recovery in delayed EL intensity at the end of the pulse) in case of the PtOEP devices, in stark contrast with its clear presence in the Ir(piq)₃ devices. Since the occurrence of host-host TTA obviously necessitates the presence of host triplets in high concentrations, the differences between the delayed EL responses of the Ir(piq)₃ and PtOEP devices indicates that the population of host triplet excitons must be much higher in the Ir(piq)₃ devices. The results in figures 6.16 and 6.22 therefore indicate that there is no correlation between lower device stability and a larger population size of host triplets in the emitting layer. It is therefore possible that host triplets do not play a significant role in the EPIA process.

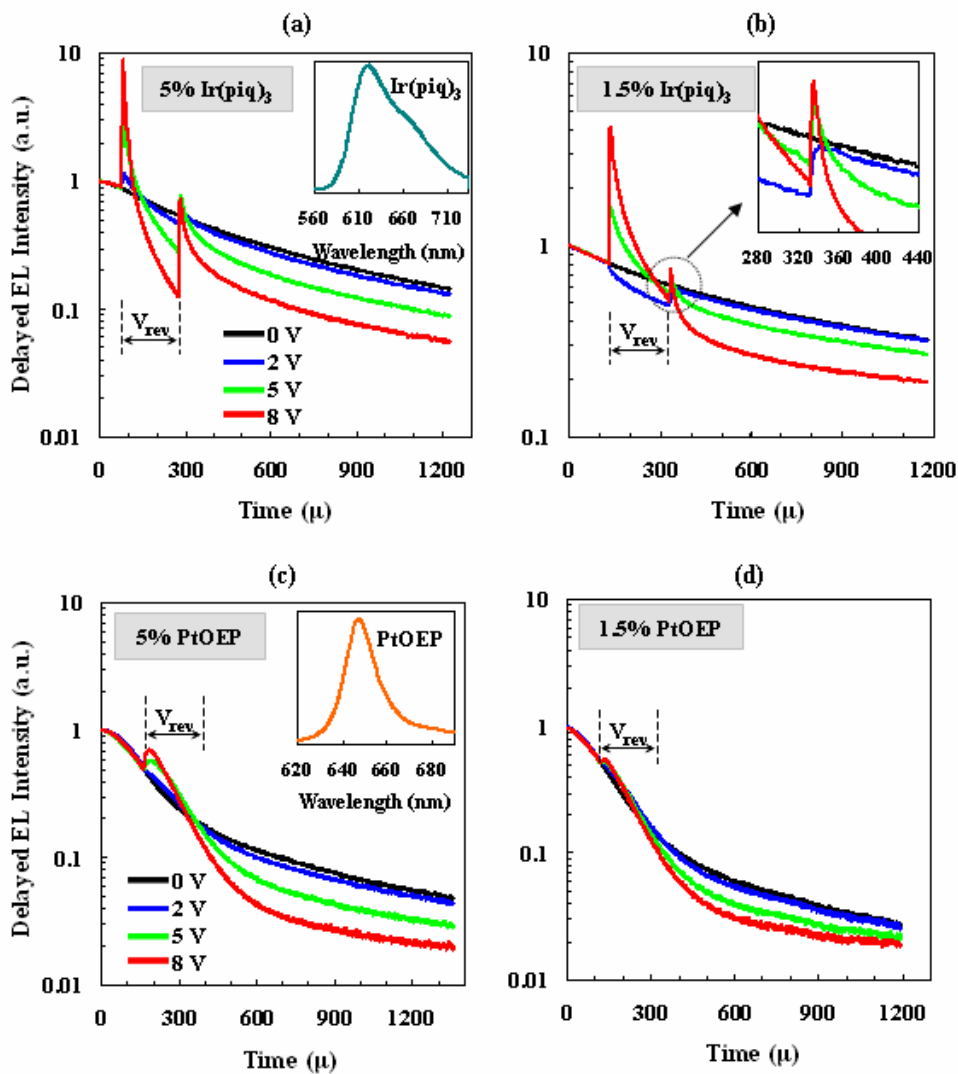


Figure 6.22: Delayed EL signals collected from the devices with (a) 5% Ir(piq)₃, (b) 1.5% Ir(piq)₃, (c) 5% PtOEP and (d) 1.5% PtOEP versus time elapsed from the end of the forward bias pulse. A 200 μs reverse bias pulse (with a magnitude of 2, 5 or 8 V) is applied to the devices during the signal collection. The insets of (a) and (c) show delayed EL spectra of the devices, whereas the inset of (b) shows amplified delayed EL upon the removal of the reverse bias.

Considering that the delayed EL characteristics reveal differences in the concentrations in trapped charges between the PtOEP and Ir(piq)₃ devices, it is possible to wonder if the differences in the device lifetimes in figure 6.16 could simply be due to differences in charge trapping effects. This

is based on the fact that the accumulation of polarons (i.e. charges) can also cause device degradation via polaron-triplet quenching effects. A close examination of the data in figure 6.22 however reveals that there is no correlation between a shorter device lifetime and a higher extent of charge trapping. For example, the 5% Ir(piq)₃ and 5% PtOEP devices have more trapped charges relative to the 1.5% Ir(piq)₃ and 1.5% PtOEP devices, respectively, as evident from the higher spikes at the beginning of the reverse bias pulse. Despite this, the devices exhibit longer lifetime (in figure 6.16) relative to their 1.5% guest counterparts. This suggests that the differences in device stabilities cannot be primarily due to charge trapping effects alone. The results therefore point to EPIA as the primary mode of degradation in PhOLEDs and to host singlet excitons - as opposed to triplet excitons - as the main exciton species involved in inducing this mechanism.

In conclusions, the influence of singlet versus triplet excitons in the EPIA of host materials and the degradation of PhOLEDs was investigated. The results show that variations in the lifetime of devices using the same host but different guests are primarily due to different rates of EPIA of the host material. Further investigations reveal that there is a correlation between a poorer device degradation and a larger concentration of singlet excitons on the host during electrical driving. In contrast, no particular correlation between device degradation rate and the concentration of triplet excitons is found to be evident by delayed EL measurements. The results therefore reveal that singlet excitons play the leading role causing the EPIA of host materials and device degradation by this mechanism.

6.3 Degradation of Guest Materials

The material presented in this section was published in *Adv. Opt. Mater.* DOI: 10.1002/adom.201400640 (2015). It is reproduced here with the permission from the publisher.

Seeing the EPIA of host materials, it is natural to wonder if emitter guest materials play a similar role to that of the host material in the EL degradation of OLEDs, and what underlying mechanisms may be involved in this case.

EL degradation behavior of OLEDs in which various phosphorescent materials are used as guest emitters, in different concentrations, in a host material was first studied. The phosphorescent materials are FIrpic, Ir(ppy)₂acac, Ir(ppy)₃, Ir(mppy)₃ and Ir(piq)₃. The general structure of the devices is ITO/MoO₃(5 nm)/CBP (20 nm)/CBP: Guest(20 nm)/TPBi (30 nm)/LiF(0.5 nm)/Al(100 nm). The phosphorescent materials are doped into the CBP, the latter functions as a common host material, at

1.5 to 10% by volume (in the case of Ir(piq)₃, the concentration reaches 20%). The devices are electrically driven at a constant current density of 20 mA cm⁻² and changes in their EL intensity and driving voltage are continuously monitored. **Figure 6.23** summarizes the results, presenting the half-life values of these devices (i.e. LT50, defined as the time elapsed before the EL decreases to 50 % of its initial value) for the various guest materials and their concentrations. As the figure shows, the device EL degradation rate varies significantly not only with the guest material but also with its concentration. An increase in guest concentration from 1.5% to 5% leads to a longer LT50 (i.e. more stable EL with time) for all guests. This can be attributed to the more efficient host-to-guest energy transfer via Forster process, as the guest concentration increases. This results in a shorter exciton lifetime on CBP, which, in turn, results in a decrease in exciton-polaron-induced aggregation of the host molecules, hence the increase in EL stability. Further increasing the guest concentration (e.g. from 5% to 10%) is however observed to lead to a decrease, rather than a further increase, in LT50 (except in the case of Ir(ppy)₂acac where LT50 increases marginally). As the further increase in guest concentrations can be expected to lead to further reductions in exciton lifetimes on the host (due to enhancements in host-to-guest energy transfer by the even shorter host-to-guest distances), the decrease in device stability cannot be explained by exciton-polaron-induced aggregation of the host material. The observation therefore suggests that another degradation mechanism must be present and becomes more dominant at the higher guest concentrations.

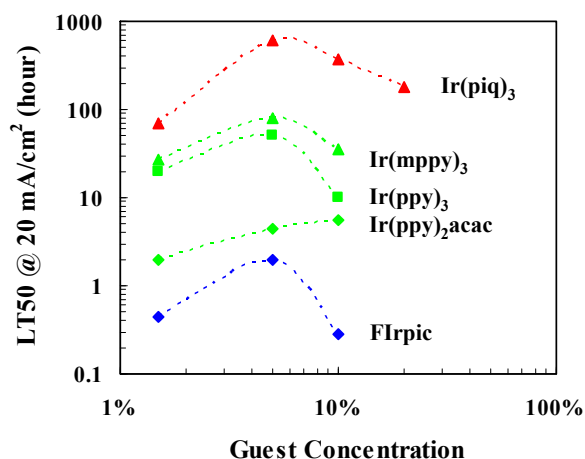


Figure 6.23: LT50 values at 20 mA cm⁻² for various phosphorescent guest materials and their concentrations.

In order to obtain more insights into the role that guests play in EL degradation, the emission characteristics of these devices with electrical driving time were first studied. **Figure 6.24(a)-(c)** show the EL spectra (normalized to the peak intensities) of devices with 5% FIrpic, 10% Ir(ppy)₂acac and 10% Ir(ppy)₃, respectively, collected before (i.e. from the fresh devices) and after electrical driving at 20 mA cm⁻² for certain periods of time (as shown). Clearly, the device with FIrpic (figure 6.24(a)) displays significant spectral changes after electrical driving. A close examination of figures 6.24 (b) and (c) also reveals detectable, yet smaller, spectral changes. To better visualize the spectral changes, the differences between the EL spectra collected after the electrical driving relative to the initial ones are calculated (by subtracting the initial spectrum from the spectrum of the aged device) and presented in the insets of the figures. The differences clearly correspond to the emergence of new well defined bands at longer wavelengths. For example, in the case of the FIrpic device, two new bands with peaks at 530 nm and 580 nm appear, and the second band becomes stronger after 90 minutes. In the cases of the Ir(ppy)₂acac and Ir(ppy)₃ devices, changes after 22 hours and 62 hours of electrical driving, respectively, correspond to new bands with peaks at ~ 550 nm and ~ 600 nm. The appearance of new longer-wavelength bands suggests that they may be the result of molecular aggregation in these materials, similar to that observed in several other OLED material systems,⁸⁵ in this case induced by the electrical driving.

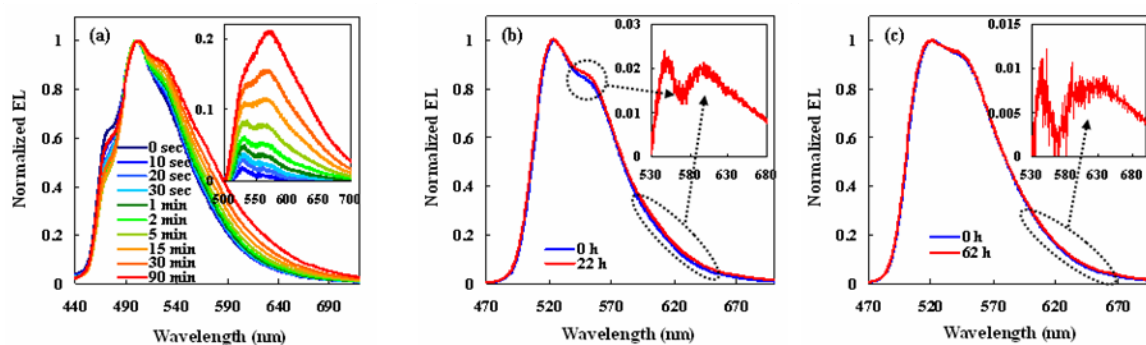


Figure 6.24: EL spectra (normalized to the peak intensities) of devices with (a) 5% FIrpic, (b) 10% Ir(ppy)₂acac and (c) 10% Ir(ppy)₃, collected before and after electrical driving at 20 mA cm⁻² for certain periods of time. Insets: differences between the EL spectra collected after the electrical driving relative to the initial ones.

In general, it is possible that the changes in the EL spectra with the electrical stress are due to the aggregation of the host material, since wide-E_g hosts like CBP are generally susceptible to electrical-

driving-induced aggregation which leads to similar EL spectral broadening with aging. The peak wavelengths of the new bands in the insets of figure 6.24 do not however correspond to CBP aggregate band (i.e. at ~ 500 nm). Moreover, the fact that the peak wavelengths of the new bands in figure 6.24 insets vary with the different guest materials (i.e. despite CBP being the host material in the three cases) further rules out this possibility. The results therefore suggest that the new bands must originate from the aggregation of the guest emitters rather than the host material.

To investigate the origin of these bands, the effect of varying the guest concentration was also studied. **Figure 6.25(a)-(c)** show normalized EL spectra collected from fresh devices containing FIrpic, Ir(ppy)₂acac and Ir(ppy)₃, respectively, with concentrations of 1.5, 5 and 10%. As the figures show, an increase in guest concentration leads to a red-shift in the EL spectra, which can be attributed to the decrease in the intermolecular separation between the guest molecules and thus a higher probability of their aggregation. The differences between the EL spectra collected from the devices with 5 and 10% guests relative to that from the device with 1.5% guest are shown in the insets of the figures (showing differences at longer-wavelength regions only). The differences clearly correspond to new bands at longer wavelengths. A comparison between the bands in the insets of figure 6.25 and those in figure 6.24 reveals a clear parallelism between the two observations, suggesting that the spectral changes caused by the prolonged electrical driving are not dissimilar from those obtained by means of increasing the guest concentration and thereby its aggregation, suggesting that the spectral broadening and the underlying emergence of longer-wavelength bands observed after the electrical driving in figure 6.24 may indeed be due to the aggregation of the phosphorescent guest materials. It is noted that there is ~ 20 - 30 nm difference between the peak positions of the bands in the insets of figure 6.25 and those in the insets of figure 6.24. This difference may perhaps be due to possible shifts in the location of the e-h recombination zone in the devices upon changing the guest concentration. This is supported by the fact that increasing guest concentration brings about a decrease in the device driving voltage, indicative of easier hole transport, which makes a shift in the recombination zone towards the cathode (yet still within the CBP:Guest layer) likely. As a result, optical interference effects may be different in case of the scenario of figure 6.25 (i.e. different guest concentrations) versus that of figure 6.24 (same guest concentration but different stress times).

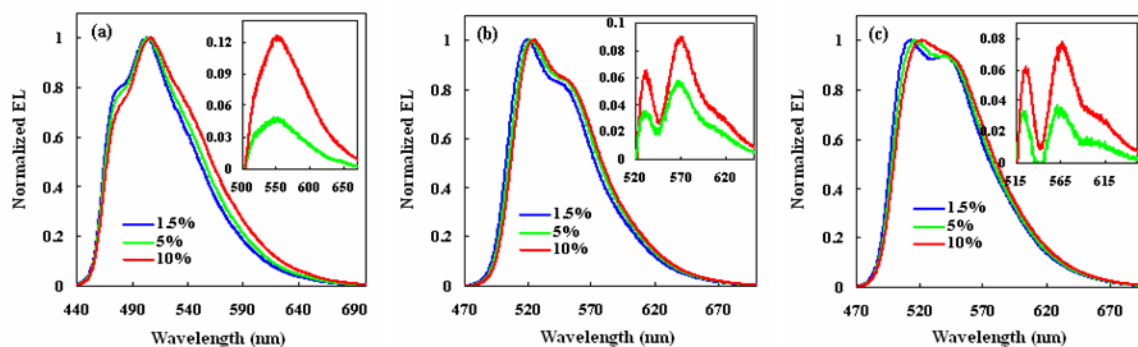


Figure 6.25: Normalized EL spectra collected from fresh devices containing (a) FIrpic, (b) Ir(ppy)₂acac and (c) Ir(ppy)₃, with concentrations of 1.5, 5 and 10%.

To further verify the above hypothesis that guest aggregation occurs during device electrical aging, and is behind the observed spectral changes, Ir(ppy)₂acac was selected as a representative phosphorescent guest because of its widespread use in highly efficient phosphorescent OLEDs, and study its EL spectral changes with electrical stress when used in the form of a neat layer in devices. **Figure 6.26(a)-(c)** show EL spectra collected from devices of the structure ITO/MoO₃(5 nm)/CBP(30 nm)/Ir(ppy)₂acac(x nm)/TPBi(30 nm)/LiF(0.5 nm)/Al(100 nm), where x is equal to 2, 1 and 0.5, respectively, before and after 14 hours of electrical driving at 20 mA cm⁻¹. As the figures illustrate, all three devices show broadening in their EL spectra relative to the initial ones after 14 hours of electrical stress. The differences between the spectra after the stress relative to the initial ones are presented in figure 6.26(d). Again here, the spectral differences correspond to new bands at longer wavelengths, and are quite similar to those seen in figure 6.24(b), suggesting that the bands in figures 6.26(d) and 6.24(b) are essentially from the same luminescent species, i.e., Ir(ppy)₂acac aggregate species. Perhaps even more remarkably however, the devices with thicker neat Ir(ppy)₂acac layers show more spectral broadening after the electrical stress when compared to those with thinner ones. This confirms that the new bands seen in figure 6.26 are indeed due to Ir(ppy)₂acac aggregate species, since the larger number of Ir(ppy)₂acac molecules in the thicker neat layers can be expected to allow for easier, hence more, aggregation. The results in figure 6.26 also suggest that the EL spectral changes with electrical stress are not a result of changes in microcavity effects due to possible e-h recombination zone shift, as the use of a very thin neat layer of Ir(ppy)₂acac pins the recombination zone due to the strong confinement of both charges and excitons on the narrower E_g material (i.e., Ir(ppy)₂acac).

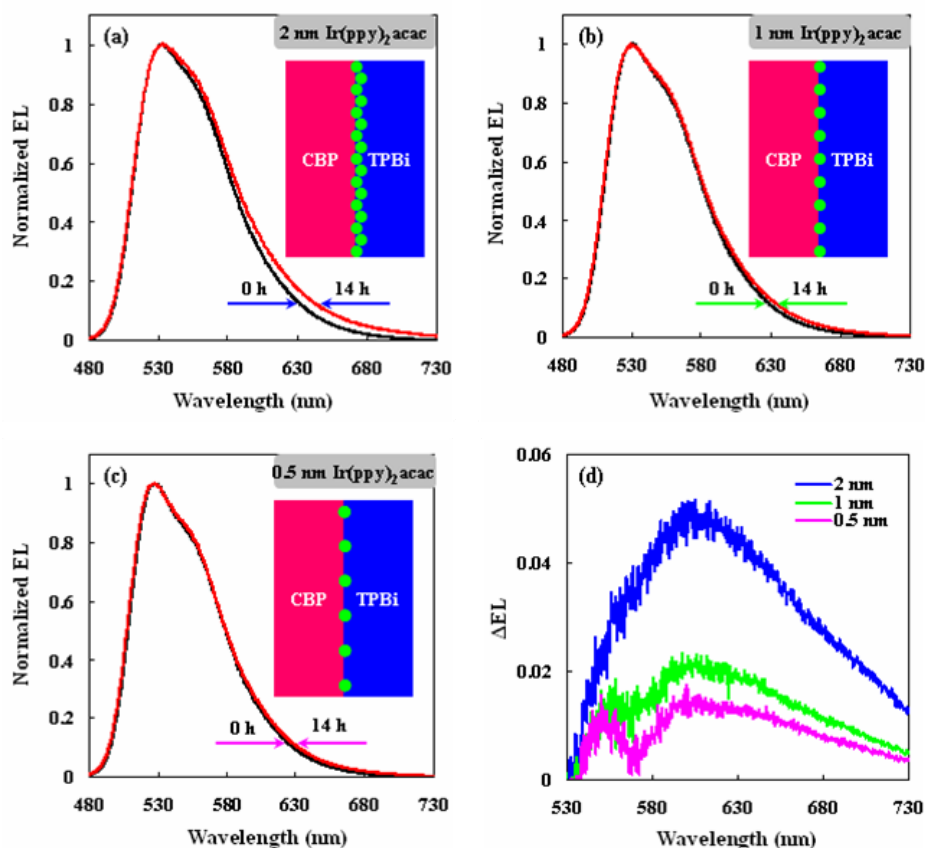


Figure 6.26: EL spectra collected from devices of the structure ITO/MoO₃(5 nm)/CBP(30 nm)/Ir(ppy)₂acac(x nm)/TPBi(30 nm)/LiF(0.5 nm)/Al(100 nm), where x is equal to (a) 2, (b) 1 and (c) 0.5, before and after 14 hours of electrical driving at 20 mA cm⁻¹. (d) Differences between the spectra after the stress relative to the initial ones.

From the above results, the conclusion can be drawn that electrical driving results in EL spectral changes of phosphorescent guests such as FIrpic, Ir(ppy)₂acac and Ir(ppy)₃, associated with the emergence of new bands at longer wavelengths which can be attributed to the aggregation of these materials. It is important to point out that the spectral changes in Ir(mppy)₃ and Ir(piq)₃ were also studied. Ir(mppy)₃ shows very little spectral changes with electrical stress, whereas Ir(piq)₃ shows almost no detectable spectral changes at all, suggesting that Ir(piq)₃ may not aggregate easily. It is also noticed that the guest materials that aggregate more easily with aging (i.e., showing bigger spectral changes after the same electrical driving time), such as FIrpic and Ir(ppy)₂acac, correspond to much shorter device LT50, indicating that the aggregation of these guest materials is associated with

EL degradation in the OLEDs, and is fastest in case of FIrpic (the blue emitter). **Figure 6.27** presents a plot of EL stability of the devices (i.e. LT50 values) against the time for onset of aggregation (i.e. defined as the time of electrical driving elapsed until the aggregate EL band intensity reaches 1% of the monomer EL band intensity, the latter is used as an indicator of the susceptibility of the guest materials to aggregation). As the figure shows, there is a clear correlation between device EL stability and the susceptibility of the guest materials to aggregation, suggesting that a lower guest aggregation tendency with electrical stress is a prerequisite for a higher device stability.

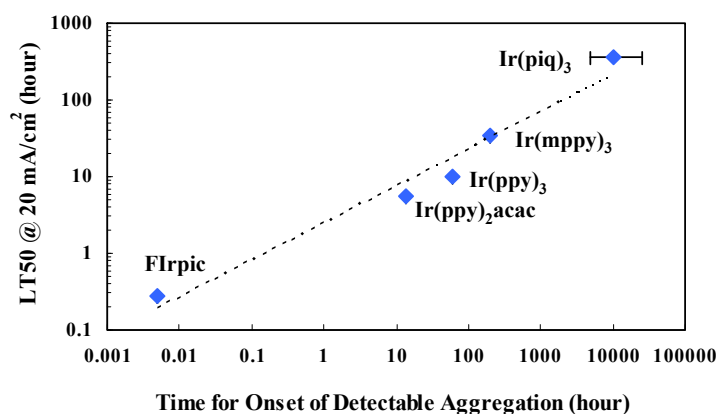


Figure 6.27: EL stability of the devices (i.e. LT50 values) versus time for onset of detectable aggregation in the devices by electrical aging (i.e. defined as the time of electrical driving elapsed until the aggregate EL band intensity reaches 1% of the monomer EL band intensity).

An examination of the aggregation trends of the guest materials tested above suggests the presence of a close correlation between the extent of aggregation due to electrical driving and the magnitude of the energy gap of the material, where the wider the energy gap the higher the susceptibility to aggregation. A molecule in an excited electronic state will have an excess amount of energy (due to excitation) of the same order of energy of a high vibrational mode of the ground state (i.e. equivalent to high thermal energy).¹⁰¹ a molecule in an excited state can be therefore expected to be more mobile and hence more able to reorient itself and/or undergo aggregation. As the reorganization of electrons in a molecule when it becomes excited also generally leads to an increase in its dipole moment, the presence of polarons (charges) can be expected to be able to influence excited molecules more strongly, possibly providing a driving force for the molecules to attain certain preferential molecular orientations, and thus to move and reorient themselves in certain preferential direction. In this context, the dependence of aggregation on the E_g of the guests may be attributed to

the fact that molecules of wider- E_g materials have more energy when in their excited states relative to molecules of narrower- E_g materials, and therefore are offered a better opportunity for molecular mobility and thus to be more prone to morphological instabilities and aggregation.

It should be noted that guests of the same (or similar) E_g still show quite different extents of aggregation under the same electrical driving condition. For instance, $\text{Ir}(\text{ppy})_2\text{acac}$ shows significant aggregation, whereas $\text{Ir}(\text{ppy})_3$ and $\text{Ir}(\text{mppy})_3$ only show moderate and little aggregations, respectively, despite the fact that the three phosphorescent guests have very similar E_g .^{102,103} Based on such comparison, it is clear that the molecular structure also plays an important role in the electrical-driving-induced aggregation process which, like for any other molecular aggregation process, is not surprising. The molecular structures of these Ir-based compounds are shown in **figure 6.28**. Although these three Ir-based molecules have bulky three dimensional structures, and thus can in general be expected to be less prone to aggregation, especially when used in relatively low concentrations, it is possible that polar considerations play an important role in their susceptibility to this special mode of aggregation, i.e. by polaron-exciton interactions. For example, the higher susceptibility of $\text{Ir}(\text{ppy})_2\text{acac}$ relative to $\text{Ir}(\text{ppy})_3$ or $\text{Ir}(\text{mppy})_3$ to this aggregation mode may be due to the fact that it is not as spatially symmetric and thus may have more polar characteristics (i.e. larger dipole moment), and thus can be more strongly influenced by polarons especially when in the excited state (due to the fact that molecules in an excited electronic state generally have a larger dipole moment relative to that in the ground states).¹⁰¹

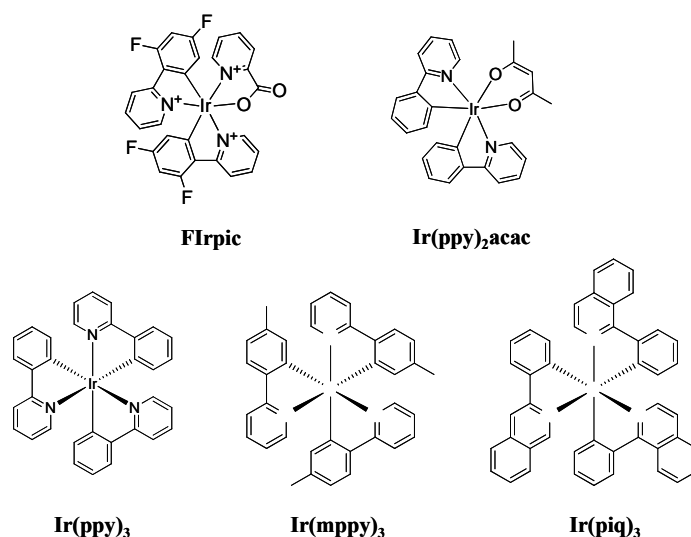


Figure 6.28: Molecular structures of Ir-based compounds used as phosphorescent emitters.

Finding that degradation in phosphorescent OLEDs is associated with electric stress-induced molecular aggregation of the guest emitter molecules, the question about the main driving force behind this phenomenon and whether, for example, it is caused primarily by the electrical stress (i.e. the flow of current) itself or, rather, by the excitons that get produced by e-h recombination, arises. The degradation behavior of these materials was therefore studied in unipolar (hole-only) devices utilizing various stress scenarios that allow investigating the effects of polarons and excitons independently. Since FIrpic has shown the most significant aggregation with the electrical stress so far, it is selected as a representative guest for this investigation. The structure of the devices is ITO/MoO₃(5 nm)/CBP(30 nm)/FIrpic(2 nm)/TPBi(5 nm)/MoO₃(10 nm)/Al(100 nm), as shown in the left part of **figure 6.29(a)**. When under a forward bias (i.e., the ITO is positively biased relative to the Al), the injection of electrons from the Al is blocked by the top MoO₃, and therefore the flow of current occurs exclusively by holes injected from the ITO. As a result, these devices have unipolar h-only transport characteristics. The devices are subjected to one of three stress scenarios: (1) Current flow only (denoted by <I only>), under a forward bias to sustain a current flow of density ~20 mA cm⁻²; (2) Irradiation by light only (denoted by <L only>), at 365 nm of power density ~0.5 mW cm⁻²; (3) Current flow and irradiation together (denoted by <I + L>), subjected to scenarios (1) and (2) simultaneously. Also, a control device was kept in the dark to be used as a reference (denoted by <C>). After ~ 4 hours under the above conditions, the Al electrode of all four devices was peeled off using scotch tape in a N₂ atmosphere. (Since the adhesion of inorganic/inorganic interfaces is much stronger than that of organic/inorganic interfaces, the 10 nm MoO₃ layer would also be peeled off with the Al layer.) After that, LiF(1nm)/Al(100nm) cathodes were deposited on these devices. As such, electron injection from the Al cathode now becomes possible, allowing bipolar transport and EL to occur. The process is illustrated in figure 6.29(a), in which these h-only devices are converted into bipolar devices, capable of EL, by replacing the top electrode with an electron-injecting cathode.

Figure 6.29(b) presents the normalized EL spectra of these devices, showing EL from the FIrpic monolayer. Remarkably, as the figure illustrates, the device subjected to the scenario <I + L> shows a broader EL spectrum than the control device or those subjected to the scenarios <I only> or <L only>. The inset of figure 6.29(b) displays the “spectral shift” observed in the devices subjected to the scenarios <I + L>, <I only> and <L only>, obtained from the mathematical difference in the EL spectra of the three devices after the aging relative to the control one (i.e. the one kept in the dark). Clearly, the device subjected to the scenario <I + L> shows a significant change in the EL spectrum relative to the control one, and the difference corresponds to a band at ~ 550 nm which is similar to

that shown in figure 6.24(a). In contrast, the device subjected to the scenario <L only> just shows a small spectral change, which corresponds to a much weaker band at ~ 550 nm, whereas the device subjected to the scenario <I only> shows almost no detectable changes at all.

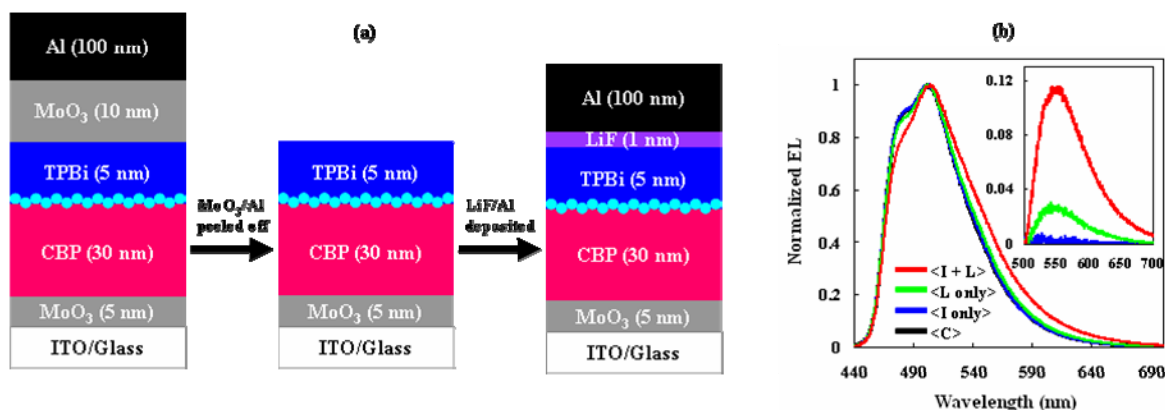


Figure 6.29: (a) Illustration of replacing the top electrode with an electron-injecting cathode, in which h-only devices are converted into bipolar devices. (b) Normalized EL spectra of FIrpic collected from the four bipolar devices. The inset shows differences between the EL spectra of the devices subjected to the scenarios <I + L>, <I only> and <L only> relative to that of the control one.

Given the obvious similarity between this band and those in figures 6.24(a) to 6.25(a), it can be ascribed to the formation of FIrpic aggregates. The differences in the spectra of the device subjected to the scenario <I + L> and those subjected to <I only> or <L only> indicate that it must be due to the co-existence of both FIrpic excitons and FIrpic positive polarons (i.e. due to exciton-polaron interactions). It is important to note that the device subjected to the scenario <L only>, where, in principle, only excitons are created and concentration of polarons should be negligible, also shows a small aggregation band. This can be ascribed to the fact that the LUMO level of FIrpic is close to that of TPBi,¹⁰⁴ and therefore a small number of polarons can be generated via the dissociation of FIrpic excitons by the FIrpic/TPBi interface. These polarons may interact with excitons leading to FIrpic aggregation, hence giving rise to the small spectral broadening in the scenario <L only>.

As the CBP host is also susceptible to aggregation when subjected to the scenario <I + L>, it is necessary to rule out the possibility that the spectral broadening observed in figure 6.29(b) is due to the aggregation of CBP. a parallel study was therefore conducted on the degradation behavior of h-only devices without the FIrpic monolayer under the same stress scenarios. After four hours, the top

electrodes were replaced, again converting the h-only devices into bipolar devices capable of EL, as shown in **figure 6.30(a)**. Figure 6.30(b) shows the normalized EL spectra of CBP collected from these devices. The inset of figure 8(b) displays spectral differences observed in the devices subjected to the scenarios $\langle I + L \rangle$, $\langle I \text{ only} \rangle$ and $\langle L \text{ only} \rangle$ relative to the control one. Clearly, only the device subjected to the scenario $\langle I + L \rangle$ shows a very small EL spectral broadening relative to the control one, and the difference corresponds to a band at ~ 500 nm, which corresponds to CBP aggregation band, and thus obviously differs from that in figure 6.29. These results convincingly prove that the spectral changes in figure 6.29 indeed arise from FIrpic aggregates due to exciton-polaron interactions. That this aggregation occurs only when both excitons and positive polarons are present simultaneously, but not when either of them is present alone indicates that it must be driven by interactions between the two species. Since both guest excitons and guest positive polarons are present simultaneously in high concentrations in the e-h recombination zone (i.e., in the vicinity of the CBP/TPBi interface) during device normal operation, the same effect can take place. Thus, it may be concluded that the changes in the EL spectra with the electrical stress observed in figure 6.24 are the result of guest aggregation due to exciton-polaron-induced aggregation (EPIA).

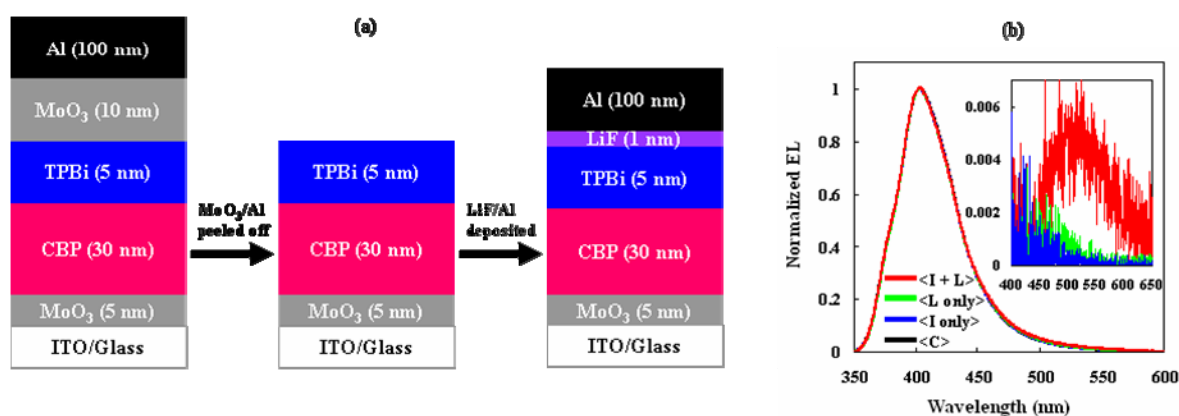


Figure 6.30: (a) Illustration of replacing the top electrode with an electron-injecting cathode, in which h-only devices are converted into bipolar devices. (b) Normalized EL spectra of CBP collected from the four bipolar devices. The inset shows differences between the EL spectra of the devices subjected to the scenarios $\langle I + L \rangle$, $\langle I \text{ only} \rangle$ and $\langle L \text{ only} \rangle$ relative to that of the control one.

In this interaction, the excitons role could be providing sufficient energy for assisting molecular movement or reorientation of the guest molecules, whereas the polarons role could be increasing the

dipolar characteristics (i.e. dipole moment) of the molecules, hence provides a driving force to attain certain preferential molecular orientations, and thus to move and reorient themselves, stronger. Therefore, when subjected to conditions where both excitons and polarons are present in high concentrations, the guest material molecules undergo morphological reorganization or reorientation in order to reach more energetically favorable states. This could explain why molecules of wider- E_g materials are more susceptible to EPIA relative to molecules of narrower- E_g materials, as wider- E_g materials could produce excitons that are more energetic. This may also explain why Ir(ppy)₂acac shows the most significant EPIA among the three green emitters (i.e. Ir(ppy)₂acac, Ir(ppy)₃ and Ir(mppy)₃) despite their similar E_g , as the molecular structure of Ir(ppy)₂acac is less symmetric, and thus could be expected to have more polar characteristics that can help induce molecular movement/reorientation, relative to the other more symmetric materials, in the presence of polarons.

The decrease in EL efficiency as a result of this EPIA can be ascribed to increased quenching by bimolecular processes such as concentration quenching and bi-exciton annihilation processes, which become more efficient as intermolecular distances decrease, and also to changes in E_g of the material (narrower E_g of the aggregate species, as evident from their EL at longer wavelengths).

It should be pointed out that this electrical-driving-induced aggregation is not limited to phosphorescent guest materials. Preliminary studies on fluorescent materials show they are susceptible to the same phenomenon. **Figure 6.31**(a) and (b) show EL spectra (normalized to the peak intensities) with an electrical driving at 20 mA cm⁻² collected from devices containing C545T a widely used green fluorescent guest at the concentrations of 10% and 5%, respectively. The structure of the devices is ITO/MoO₃(5 nm)/NPB(40 nm)/Alq₃:C545T(10 nm)/Alq₃(20 nm)/LiF(0.5 nm)/Al(100 nm). As can be seen from the figure, the device containing 10% C545T exhibits clear spectral broadening after electrical stress, which corresponds to new bands with peaks at ~ 560 and 630 nm, whereas the device containing only 5% C545T shows negligible spectral changes. Neat bi-layer NPB/Alq₃ devices without the C545T were also tested. Figure 9(c) shows EL spectra with the same electrical driving collected from one such device. The device shows no detectable changes in the EL spectra with time at all, suggesting that the new bands in figure 6.31(a) essentially arise from C545T aggregates species. Our previous studies on blue fluorescent materials (e.g. TBADN and ADN) showed that they are similarly susceptible to electric-driving-induced aggregation.⁸⁵ Yellow/red fluorescent guests such as Rubrene and DCJTb were also tested. They however show no detectable changes in their EL spectra with electrical driving, indicating that these fluorescent guests

are less prone to electrical-driving-induced aggregation, possibly due to their relatively narrower E_g . Based on these observations, it can be concluded that the electrical-driving-induced aggregation occurs in wide E_g fluorescent guests as well, and is a widely existing phenomenon in OLEDs.

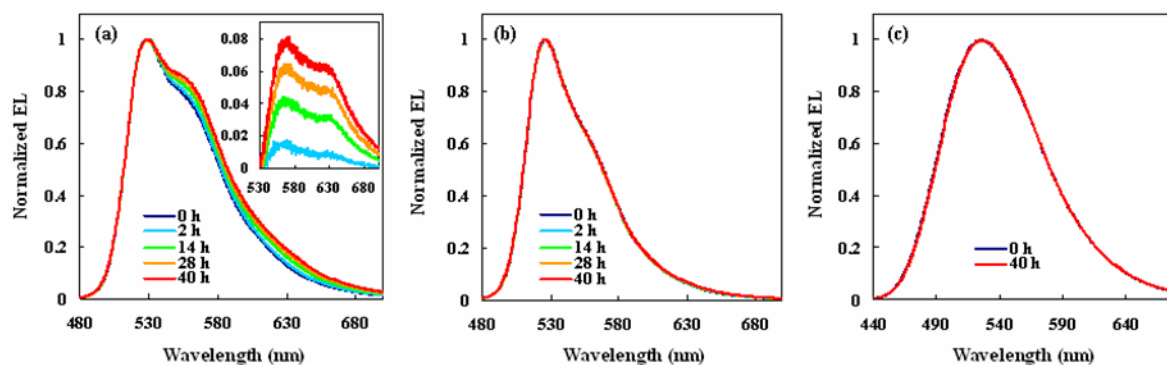


Figure 6.31: EL spectra (after normalization) with continuous electrical driving at 20 mA cm^{-2} collected from devices of the structure ITO/MoO₃(5 nm)/NPB(40 nm)/Alq₃:C545T(10 nm)/Alq₃(20 nm)/LiF(0.5 nm)/Al(100 nm), in which the fluorescent emitter C545T is doped into the Alq₃ host with the concentration of (a) 10%, (b) 5% and (c) 0%.

The above findings uncover a previously unknown OLED degradation mechanism based on the aggregation of guest materials that is caused by exciton-polaron interactions. It affects guest materials with wider E_g and flatter molecular structures more severely. This degradation mechanism explains the generally much lower EL stability of blue devices relative to their green and red counterparts, especially in case of phosphorescent emitters, which, due to their generally wider E_g 's, are more susceptible to this aggregation mode.

In conclusion, the EL degradation mechanisms of various phosphorescent and fluorescent guests widely used in OLEDs were studied. Contrary to expectations, it is found that OLEDs with higher guest concentrations can have much lower EL stability. It is determined that guest emitters, especially when used in high concentrations in OLEDs, are generally susceptible to electrical-driving-induced aggregation. Further study reveals that such aggregation process occurs only when both excitons and positive polarons are present in high concentrations, suggesting that the phenomenon is driven by exciton-polaron interactions. Such aggregation process is found to occur in a wide range of wide- E_g guests commonly used as emitters in OLEDs and is closely associated with EL degradation in OLEDs. Quite notably, the extent of aggregation appears to correlate with the guests E_g , and is influenced by molecular structure. The findings uncover a previously unknown degradation mechanism that

appears to be responsible for the generally much lower EL stability of blue devices relative to their green and red counterparts, especially in case of phosphorescent emitters.

6.4 Summary

In this chapter, degradation of organic/organic interfaces due to exciton-polaron interactions is studied. Results show that organic/organic interfaces commonly used in OLEDs degrade rapidly due to the aggregation of wide-bandgap materials (commonly used as hosts in PhOLEDs) induced by the co-existence of both excitons and positive polarons on the molecules of the materials. It is found that the extent of aggregation appears to correlate with the materials E_g rather than with their T_g temperatures.

The studies further show that guest emitters (both phosphorescent and fluorescent emitters) in the vicinity of organic/organic interfaces are also generally susceptible to aggregation driven by exciton-polaron interactions. Such aggregation process is determined to occur in a wide range of wide- E_g guests emitters and is closely associated with EL degradation in OLEDs. The extent of aggregation correlates with the guests E_g , and is influenced by molecular structure.

Chapter 7

Summary and Future Work

7.1 Summary

In this thesis, exciton-induced degradation of interfaces in OLEDs, including organic/electrode and organic/organic interfaces, is studied. The investigations uncover that excitons can affect and degrade device interfaces much more severely than they can affect bulk material.

In the case of organic/electrode interfaces:

1. The degradation is caused by the presence of excitons in the vicinity of the interfaces.
 - Leading to a deterioration in charge transport across the interfaces
 - Including both charge injection and charge extraction
2. XPS measurements reveal that the degradation is photo-chemical in nature.
 - Associated with a reduction in chemical bonds between metal atoms and organic molecules
3. Such degradation can occur during device normal operation by means of
 - Electron-hole recombination near the interfaces
 - Diffusion of excitons to the interfaces
 - Re-absorption of emitted photons
4. The degradation can be greatly suppressed by the use of inorganic interfacial layers.
 - low-workfunction alkali metals for organic/metal interfaces
 - high-workfunction metal oxides for ITO/organic interfaces
5. Similar degradation mechanism is expected to play a role in limiting the stability of other organic optoelectronic such as organic photo-detectors and organic solar cells.

In the case of organic/organic interface:

1. The degradation arises from aggregation of both host and guest materials in the vicinity of the e-h recombination zone.
 - Such aggregation is induced by the co-existence of both excitons and positive polarons on host or guest molecules.
 - The extent of aggregation correlates with the materials E_g rather than with their T_g temperatures.

- The aggregation process is not simply a result of Joule heating effects by the flow of electric current.
2. The degradation mechanism could provide the first explanation for
- The generally lower stability of phosphorescent OLEDs relative to their fluorescent counterparts, considering that the former generally utilize wider- E_g host materials relative to those used with the latter.
 - The generally much lower EL stability of blue devices relative to their green and red counterparts, especially in case of phosphorescent emitters.

7.2 Future Work

Now with the knowledge on device degradation mechanisms, it becomes possible to develop OLEDs of improved stability. The approaches of enhancing the stability of organic/electrode interfaces are already well explored in this work and widely utilized in the OLED community, i.e. the use of interfacial layers between organic layers and electrodes.

Improving the stability of organic/organic interfaces, i.e. preventing organic materials (including host and guest materials) from aggregation due to exciton-polaron interactions, is however far more difficult. The main reason is that the location where polarons accumulate is also where excitons are formed. As a result, it becomes extremely difficult, if not impossible, to suppress exciton-polaron interactions by separating polarons and excitons from each other in devices. One solution to this problem might be developing materials of novel molecular structures (e.g. more bulky structures) that are intrinsically less prone to exciton-polaron-induced aggregation but meanwhile maintain decent hole/electron mobility.

Since separating polarons and excitons may not be realistic, another approach to suppress exciton-polaron interactions could be reducing the density of excitons and polarons in the recombination zone, thus reducing the probability of having an exciton and polaron simultaneously on a molecule that triggers aggregation. To this end, new device structures can be explored, such as the utilization of n-type doping ETLs and tandem-structure OLEDs.

For devices with n-type doping ETLs, the transport of electrons is greatly enhanced due to the generation of free electrons by doped metal atoms (e.g. Cs or Li). The electron-hole balance therefore becomes much better, given the fact that the hole mobility of HTLs is typically several orders of magnitude higher than the electron mobility of ETLs. As a result, the electron-hole recombination

zone is significantly widened to the anode side, which naturally leads to a lower density of excitons and polarons in organic layers, and thus a lower possibility of the occurrence of exciton-polaron-induced aggregation.

For tandem-structure OLEDs, typically two (or more) OLED cells are stacked together, each of the two cells contributing $\sim 50\%$ of the total emitting photons. In this scenario, the current needed in tandem OLEDs is only half of that in single-cell OLEDs, in order to produce the same brightness. This is equivalent to reducing the exciton and polarons densities in the recombination zone by $\sim 50\%$ in the case of tandem OLEDs in comparison to that of single-cell OLEDs. The aggregation process due to exciton-polaron interactions could be therefore suppressed.

Appendix A

List of Publications Derived from the Thesis Research

Following is the list of publications included in this thesis:

- [1] **Q. Wang**, G. Williams, T. Tsui, H. Aziz, “Photochemical deterioration of the organic/metal contacts in organic optoelectronic devices”, *J. Appl. Phys.* **112**, 064502 (2012).
- [2] **Q. Wang**, H. Aziz, “Role of the cathode interfacial layers in improving the stability of organic optoelectronic devices”, *SPIE Organic Photonics+ Electronics*, 84760D-84760D-5 (2012).
- [3] **Q. Wang**, H. Aziz, “Correlation between exciton-induced degradation of organic/metal interfaces and energy barrier for electron injection at organic/metal interfaces in organic optoelectronic devices”, *SPIE Organic Photonics+ Electronics*, 882920-882920-9 (2013).
- [4] **Q. Wang**, G. Williams, H. Aziz, “Photo-degradation of the indium tin oxide (ITO)/organic interface in organic optoelectronic devices and a new outlook on the role of ITO surface treatments and interfacial layers in improving device stability”, *Org. Electron.* **13**, 2075-2082 (2012).
- [5] **Q. Wang**, H. Aziz, “Degradation of organic/organic interfaces in organic light-emitting devices due to polaron–exciton interactions”, *ACS Appl. Mater. Interfaces* **5**, 8733–8739 (2013).
- [6] **Q. Wang**, B. Sun, H. Aziz, “Exciton-polaron-induced aggregation of wide-bandgap materials and its implication on the electroluminescence stability of phosphorescent organic light-emitting devices”, *Adv. Funct. Mater.* **24**, 2975-2985 (2014).
- [7] **Q. Wang**, H. Aziz, “Exciton–polaron-induced aggregation of organic electroluminescent materials: a major degradation mechanism in wide-bandgap phosphorescent and fluorescent organic light-emitting devices”, *Adv. Opt. Mater.* DOI: 10.1002/adom.201400640 (2015).
- [8] **Q. Wang**, H. Aziz, “The different influence of singlet and triplet excitons in the degradation of phosphorescent organic light-emitting devices due to exciton-polaron-induced aggregation of host materials”, *Org. Electron.* DOI:10.1016/j.orgel.2015.08.019 (2015).

Bibliography

-
- ¹ H. Shirakawa, E. J. Louis, A. G. MacDiarmid, C. K. Chiang and A. J. Heeger, "Synthesis of electrically conducting organic polymers: halogen derivatives of polyacetylene, (CH)_x", *J. Chem. Soc. Chem. Commun.* **16**, 578-580 (1977).
- ² C. W. Tang and S. A. VanSlyke, "Organic electroluminescent diodes", *Appl. Phys. Lett.* **51**, 913 (1987).
- ³ C. D. Dimitrakopoulos and P. R. L. Malenfant, "Organic thin film transistors for large area electronics", *Adv. Mater.* **14**, 99 (2002).
- ⁴ P. Peumans, S. Uchida and S. R. Forrest, "Efficient bulk heterojunction photovoltaic cells using small-molecular-weight organic thin films", *Nature* **425**, 158-162 (2003).
- ⁵ D. Ray and K. L. Narasimhan, "High response organic visible-blind ultraviolet detector", *Appl. Phys. Lett.* **91**, 093516 (2007).
- ⁶ S. Moller, C. Perlov, W. Jackson, C. Taussig and S. R. Forrest, "A polymer/semiconductor write-once read-many-times memory", *Nature* **426**, 166-169 (2003).
- ⁷ Adapted from <http://en.wikipedia.org>.
- ⁸ J. H. Burroughes, D. D. C. Bradley, A. R. Brown, R. N. Marks, K. MacKay, R. H. Friend, P. L. Burns, and A. B. Holmes, "Light-emitting diodes based on conjugated polymers", *Nature* **347**, 539-541 (1990).
- ⁹ W. Schottky, "Deviations from Ohm's law in semiconductors", *Phys. Z.* **41**, 570 (1940).
- ¹⁰ H. Ishii, K. Sugiyama, E. Ito, and K. Seki, "Energy level alignment and interfacial electronic structures at organic/metal and organic/organic interfaces", *Adv. Mater.* **11**, 605 (1999).
- ¹¹ W. Brutting, ICCEL2 Tutorial on OLEDs.
- ¹² M. A. Baldo, D. F. O'Brien, M. E. Thompson, and S. R. Forrest, "Excitonic singlet-triplet ratio in a semiconducting organic thin film", *Phys. Rev. B* **60**, 14422 (1999).
- ¹³ M. A. Baldo, D. F. O'Brien, Y. You, A. Shoustikov, S. Sibley, M. E. Thompson and S. R. Forrest, "Highly efficient phosphorescent emission from organic electroluminescent devices", *Nature* **395**, 151-154 (1998).
- ¹⁴ C. Adachi, M. A. Baldo, M. E. Thompson, and S. R. Forrest, "Nearly 100% internal phosphorescence efficiency in an organic light-emitting device", *J. Appl. Phys.* **90**, 5048 (2001).
- ¹⁵ Adapted from <http://www.udcoled.com/>.
- ¹⁶ H. Aziz, Z. Popovic, S. Xie, A.-M. Hor, N.-X. Hu, C. Tripp and G. Xu, "Humidity-induced crystallization of tris (8-hydroxyquinoline) aluminum layers in organic light-emitting devices", *Appl. Phys. Lett.* **72**, 756 (1998).
- ¹⁷ H. Aziz, Z. Popovic, C. P. Tripp, N.-X. Hu, A.-M. Hor and G. Xu, "Degradation processes at the cathode/organic interface in organic light emitting devices with Mg: Ag cathodes", *Appl. Phys. Lett.* **72**, 2642 (1998).

-
- ¹⁸ H. Aziz, Z. D. Popovic, N.-X. Hu, A.-M. Hor and G. Xu, “Degradation mechanism of small molecule-based organic light-emitting devices”, *Science* **283**, 1900 (1999).
- ¹⁹ Y. Luo, H. Aziz, G. Xu and Z. D. Popovic, “Improving the stability of organic light-emitting devices by using a hole-injection-tunable-anode-buffer-layer”, *J. Appl. Phys.* **101**, 054512 (2007).
- ²⁰ H. Aziz, Y. Luo, G. Xu, and Z. D. Popovic, “Improving the stability of organic light-emitting devices by using a thin Mg anode buffer layer”, *Appl. Phys. Lett.* **89**, 103515 (2006).
- ²¹ D. Y. Kondakov, J. R. Sandifer, and C. W. Tang, “Nonradiative recombination centers and electrical aging of organic light-emitting diodes: Direct connection between accumulation of trapped charge and luminance loss”, *J. Appl. Phys.* **93**, 1108-1119 (2003).
- ²² D. Y. Kondakov, “Direct observation of deep electron traps in aged organic light emitting diodes”, *J Appl. Phys.* **97**, 024503 (2005).
- ²³ Y. Luo and H. Aziz, “Space charge effects on the electroluminescence efficiency and stability of organic light-emitting devices with mixed emitting layers”, *Appl. Phys. Lett.* **95**, 073304 (2009).
- ²⁴ D. Y. Kondakov, C. T. Brown, T. D. Pawlik, and V. V. Jarikov, “Chemical reactivity of aromatic hydrocarbons and operational degradation of organic light-emitting diodes”, *J. Appl. Phys.* **107**, 024507 (2010).
- ²⁵ D. Y. Kondakov, W. C. Lenhart, and W. F. Nichols, “Operational degradation of organic light-emitting diodes: mechanism and identification of chemical products”, *J. Appl. Phys.* **101**, 024512 (2007).
- ²⁶ D. Y. Kondakov, “Role of chemical reactions of arylamine hole transport materials in operational degradation of organic light-emitting diodes”, *J. Appl. Phys.* **104**, 084520 (2008).
- ²⁷ D. Y. Kondakov and R. H. Young, “Variable sensitivity of organic light-emitting diodes to operation-induced chemical degradation: Nature of the antagonistic relationship between lifetime and efficiency”, *J. Appl. Phys.* **108**, 074513 (2010).
- ²⁸ I. Moraes, S. Scholz, B. Lüssem, and Karl Leo, “Analysis of chemical degradation mechanism within sky blue phosphorescent organic light emitting diodes by laser-desorption/ionization time-of-flight mass spectrometry”, *Org. Electron.* **12**, 341–347 (2011).
- ²⁹ S. Scholz, K. Walzer, and K. Leo, “Analysis of complete organic semiconductor devices by laser desorption/ionization time-of-flight mass spectrometry”, *Adv. Funct. Mater.* **18**, 2541–2547 (2008).
- ³⁰ S. Scholz, C. Corten, K. Walzer, D. Kuckling, and K. Leo, “Chemical degradation mechanisms of highly efficient blue phosphorescent emitters used for organic light emitting diodes”, *Org. Electron.* **8**, 709–717 (2007).
- ³¹ N. C. Giebink, B. W. D’Andrade, M. S. Weaver, J. J. Brown, and S. R. Forrest, “Direct evidence for degradation of polaron excited states in organic light emitting diodes”, *J. Appl. Phys.* **105**, 124514 (2009).
- ³² N. C. Giebink, B. W. D’Andrade, M. S. Weaver, P. B. Mackenzie, J. J. Brown, M. E. Thompson, and S. R. Forrest, “Intrinsic luminance loss in phosphorescent small-molecule organic light emitting devices due to bimolecular annihilation reactions”, *J. Appl. Phys.* **103**, 044509 (2008).
- ³³ R. C. Kwong, M. S. Weaver, M.-H. Lu, Y.-J. Tung, A. B. Chwang, T. X. Zhou, M. Hack, and J. J. Brown, “Current status of electrophosphorescent device stability”, *Org. Electron.* **4**, 155–164 (2003).

-
- ³⁴ V. V. Jarikov and D. Y. Kondakov, "Studies of the degradation mechanism of organic light-emitting diodes based on tris(8-quinolinolate)aluminum Alq and 2-tert-butyl-9,10-di(2-naphthyl)anthracene TBADN", *J. Appl. Phys.* **105**, 034905 (2009).
- ³⁵ C.-H. Gao, S.-D. Cai, W. Gu, D.-Y. Zhou, Z.-K. Wang, L.-S. Liao, "Enhanced hole injection in phosphorescent organic light-emitting diodes by thermally evaporating a thin indium trichloride layer", *Appl. Mater. Interfaces* **4**, 5211-5216 (2012).
- ³⁶ M. G. Helander, Z. B. Wang, J. Qiu, M. T. Greiner, D. P. Puzzo, Z. W. Liu, and Z. H. Lu, "Chlorinated indium tin oxide electrodes with high work function for organic device compatibility", *Science* **332**, 944 (2011).
- ³⁷ Z. D. Popovic and H. Aziz, "Delayed electroluminescence in small-molecule-based organic light-emitting diodes: Evidence for triplet-triplet annihilation and recombination-center-mediated light-generation mechanism", *J. Appl. Phys.* **98**, 013510 (2005).
- ³⁸ N. Rappaport, O. Solomesch, N. Tessler, "The interplay between space charge and recombination in conjugated polymer/molecule photocells", *J. Appl. Phys.* **98**, 033714 (2005).
- ³⁹ N. Tessler, N. Rappaport, "Loss of photocurrent efficiency in low mobility semiconductors: analytic approach to space charge effects", *Appl. Phys. Lett.* **89**, 013504 (2006).
- ⁴⁰ M. A. Baldo, S. R. Forrest, "Interface-limited injection in amorphous organic semiconductors", *Phys. Rev. B* **64**, 085201 (2001).
- ⁴¹ Q. Wang, Y. Luo, H. Aziz, "Photodegradation of the organic/metal cathode interface in organic light-emitting devices", *Appl. Phys. Lett.* **97**, 063309 (2010).
- ⁴² S. Meloni, A. Palma, J. Schwartz, A. Kahn, R. Car, "Chemistry between magnesium and multiple molecules in tris (8-hydroxyquinoline) aluminum films", *J. Am. Chem. Soc.* **125**, 7808-7809 (2003).
- ⁴³ A. Curioni, W. Andreoni, "Metal-Alq₃ complexes: the nature of the chemical bonding", *J. Am. Chem. Soc.* **121**, 8216-8220 (1999).
- ⁴⁴ C. Shen, I. G. Hill, A. Kahn, J. Schwartz, "Organometallic chemistry at the magnesium-tris (8-hydroxyquinolino) aluminum interface", *J. Am. Chem. Soc.* **122**, 5391-5392 (2000).
- ⁴⁵ V. -E. Choong, M. G. Mason, C. W. Tang, Y. Gao, "Investigation of the interface formation between calcium and tris-(8-hydroxy quinoline) aluminum", *Appl. Phys. Lett.* **72**, 21 (1998).
- ⁴⁶ F.P. Rosselli, W.G. Quirino, C. Legnani, V.L. Calil, K.C. Teixeira, A.A. leitao, R.B. Capaz, M. Cremona, C.A. Achete, "Experimental and theoretical investigation of tris-(8-hydroxy-quinolate) aluminum (Alq₃) photo degradation", *Org. Electron.* **10**, 1417-1423 (2009).
- ⁴⁷ M.P. Seah, G.C. Smith, M.T. Anthony, "AES: Energy calibration of electron spectrometers. I—an absolute, traceable energy calibration and the provision of atomic reference line energies", *Surf. Interface Anal.* **15**, 293 (1990).
- ⁴⁸ J.S. Hammond, J.W. Holubka, J.E. Devries, R.A. Duckie, *Corros. Sci.* **21**, 239 (1981).
- ⁴⁹ L.J. Gerenser, "Photoemission investigation of silver/poly (ethylene terephthalate) interfacial chemistry: The effect of oxygen - plasma treatment", *J. Vac. Sci. Technol. A* **8**, 3682 (1990).
- ⁵⁰ L.H. Tjeng, M.B.J. Meinders, J. van Elp, J. Ghijsen, G.A. Sawatzky, R.L. Johnson, "Electronic structure of Ag₂O", *Phys. Rev. B* **41**, 3190 (1990).

-
- ⁵¹ M. G. Mason, C. W. Tang, L.-S. Hung, P. Raychaudhuri, J. Madathil, D. J. Giesen, L. Yan, Q. T. Le, Y. Gao, S.-T. Lee, L. S. Liao, L. F. Cheng, W. R. Salaneck, D. A. dos Santos, J. L. Bredas, “Interfacial chemistry of Alq₃ and LiF with reactive metals”, *J. Appl. Phys.* **89**, 5 (2001).
- ⁵² S. Scholz, Q. Huang, M. Thomschke, S. Olthof, P. Sebastian, Karsten Walzer, K. Leo, S. Oswald, C. Corten, D. Kuckling, “Self-doping and partial oxidation of metal-on-organic interfaces for organic semiconductor devices studied by chemical analysis techniques”, *J. Appl. Phys.* **104**, 104502 (2008).
- ⁵³ S. Barakat, P. Lee-Sullivan, S.A. Vitale, T.Y. Tsui, “The effects of low temperature and pressure on the fracture behaviors of organosilicate thin films”, *J. Mater. Res.* **26**, 2524-2532 (2011).
- ⁵⁴ T. Tong, B. Babatope, S. Admassie, J. Meng, O. Akwogu, W. Akande, W. O. Soboyejo, “Adhesion in organic electronic structures”, *J. Appl. Phys.* **106**, 083708 (2009).
- ⁵⁵ P.G. Charalambides, J. Lund, A.G. Evans, R.M. McMeeking, “A test specimen for determining the fracture resistance of bimaterial interfaces”, *J. Appl. Mech.* **56**, 77-82 (1989).
- ⁵⁶ P.G. Charalambides, H.C. Cao, J. Lund, A.G. Evans, “Development of a test method for measuring the mixed mode fracture resistance of bimaterial interfaces”, *Mech. Mater.* **8**, 269-283 (1990).
- ⁵⁷ H. B. Michaelson, “The work function of the elements and its periodicity”, *J. Appl. Phys.* **48**, 4729 (1977).
- ⁵⁸ C. F. Madigan, M. -H. Lu, J. C. Sturm, “Improvement of output coupling efficiency of organic light-emitting diodes by backside substrate modification”, *Appl. Phys. Lett.* **76**, 1650 (2000).
- ⁵⁹ P. Lennie, J. Pokorny, V. C. Smith, “Luminance”, *J. Opt. Soc. Am. A* **10**, 1283-1293 (1993).
- ⁶⁰ F. Nuesch, L. J. Rothberg, E. W. Forsythe, Q. T. Le, Y. Gao, “A photoelectron spectroscopy study on the indium tin oxide treatment by acids and bases”, *Appl. Phys. Lett.* **74**, 6 (1999).
- ⁶¹ J. Cui, Q. Huang, J. Veinot, H. Yan, Q. Wang, G. R. Hutchison, A. G. Richter, G. Evmenenko, P. Dutta, T. T. Marks, “Anode interfacial engineering approaches to enhancing anode/hole transport layer interfacial stability and charge injection efficiency in organic light-emitting diodes”, *Langmuir* **18**, 9958-9970 (2002).
- ⁶² L. S. Hung, L. R. Zheng, M. G. Mason, “Anode modification in organic light-emitting diodes by low-frequency plasma polymerization of CHF₃”, *Appl. Phys. Lett.* **78**, 673 (2001).
- ⁶³ J. S. Kim, R. H. Friend, F. Cacialli, “Improved operational stability of polyfluorene-based organic light-emitting diodes with plasma-treated indium-tin-oxide anodes”, *Appl. Phys. Lett.* **74**, 3084 (1999).
- ⁶⁴ C. C. Wu, C. I. Wu, J. C. Sturm, A. Kahn, “Surface modification of indium tin oxide by plasma treatment: An effective method to improve the efficiency, brightness, and reliability of organic light emitting devices”, *Appl. Phys. Lett.* **70**, 1348 (1997).
- ⁶⁵ B. Choi, H. Yoon, H. H. Lee, “Surface treatment of indium tin oxide by SF₆ plasma for organic light-emitting diodes”, *Appl. Phys. Lett.* **76**, 412 (2000).
- ⁶⁶ M. Ikagawa, I. Tohno, T. Shinmura, S. Takagi, Y. Kataoka, M. Fujihira, “Study on surface modification of indium tin oxide and resist surfaces using CF₄/O₂ plasma for manufacturing organic light-emitting diodes by inkjet printing”, *J. J. Appl. Phys.* **47**, 8935-8942 (2008).

-
- ⁶⁷ S. A. Van Slyke, C. H. Chen, C. W. Tang, "Organic electroluminescent devices with improved stability", *Appl. Phys. Lett.* **69**, 2160 (1996).
- ⁶⁸ Z. B. Deng, X. M. Ding, S. T. Lee, W. A. Gambling, "Enhanced brightness and efficiency in organic electroluminescent devices using SiO₂ buffer layers", *Appl. Phys. Lett.* **74**, 2227 (1999).
- ⁶⁹ Y. Shen, D. B. Jacobs, G. G. Malliaras, G. Koley, M. G. Spencer, A. Loannidis, "Modification of indium tin oxide for improved hole injection in organic light emitting diodes", *Adv. Mater.* **13**, 16 (2001).
- ⁷⁰ V. Shrotriya, G. Li, Y. Yan, C. Chu, Y. Yang, "Transition metal oxides as the buffer layer for polymer photovoltaic cells", *Appl. Phys. Lett.* **88**, 073508 (2006).
- ⁷¹ H. You, Y. Dai, Z. Zhang, D. Ma, "Improved performances of organic light-emitting diodes with metal oxide as anode buffer", *J. Appl. Phys.* **101**, 026105 (2007).
- ⁷² F. Wang, X. Qiao, T. Xiong, D. Ma, "The role of molybdenum oxide as anode interfacial modification in the improvement of efficiency and stability in organic light-emitting diodes", *Org. Electron.* **9**, 985-993 (2008).
- ⁷³ H. Heil, G. Andress, R. Schmechel, H. von Seggern, J. Steiger, K. Bonrad, R. Sprengard, "Sunlight stability of organic light-emitting diodes", *J. Appl. Phys.* **97**, 124501 (2005).
- ⁷⁴ J. S. Kim, P. K. H. Ho, D. S. Thomas, R. H. Friend, F. Cacialli, G. W. Bao, S. F. Y. Li, "X-ray photoelectron spectroscopy of surface-treated indium-tin oxide thin films", *Chem. Phys. Lett.* **315**, 307-312 (1999).
- ⁷⁵ D. J. Milliron, I. G. Hill, C. Shen, A. Kahn, J. Schwartz, "Surface oxidation activates indium tin oxide for hole injection", *J. Appl. Phys.* **87**, 572 (2000).
- ⁷⁶ S. N. Kumar, G. Bouyssoux, F. Gaillard, "Electronic and structural characterization of electrochemically synthesized conducting polyaniline from XPS studies", *Surf. Interface Anal.* **15**, 531 (1990).
- ⁷⁷ D. T. Clark, D. Kilcast, D. B. Adams, W. K. R. Musgrave, *J. Electron. Spectrosc. Relat. Phenom.* **1**, 232 (1972).
- ⁷⁸ M. C. Gwinner, R. Di Pietro, Y. Vaynzof, K. J. Greenberg, K. H. Ho, R. H. Friend, H. Sirringhaus, "Doping of organic semiconductors using molybdenum trioxide: a quantitative time - dependent electrical and spectroscopic study", *Adv. Funct. Mater.* **21**, 1432-1441 (2011).
- ⁷⁹ C. Wu, C. Lin, G. Lee, T. Cho, C. Wu, T. Pi, "Electronic and chemical properties of molybdenum oxide doped hole injection layers in organic light emitting diodes", *J. Appl. Phys.* **105**, 033717 (2009).
- ⁸⁰ H. Baek and C. Lee, "Electroluminescence characteristics of n-type matrix materials doped with iridium-based green and red phosphorescent emitters", *J. Appl. Phys.* **103**, 054510 (2008).
- ⁸¹ W. Holzer, A. Penzkofer, and T. Tsuboi, "Absorption and emission spectroscopic characterization of Ir(ppy)₃", *Chem. Phys.* **308**, 93-102(2005).
- ⁸² R.C. Kwong, M. R. Nugent, L. Michalski, T. Ngo, K. Rajan, Y.-J. Tung, M. S. Weaver, T. X. Zhou, M. Hack, M. E. Thompson, S. R. Forrest, J. J. Brown, "High operational stability of electrophosphorescent devices", *Appl. Phys. Lett.* **81**, 1 (2002).

-
- ⁸³ J. M. Lupton, "A molecular thermometer based on long-lived emission from platinum octaethyl porphyrin", *Appl. Phys. Lett.* **81**, 2478-2480 (2002).
- ⁸⁴ H. Siboni, H. Aziz, "Causes of driving voltage rise in phosphorescent organic light emitting devices during prolonged electrical driving", *Appl. Phys. Lett.* **101**, 173502 (2012).
- ⁸⁵ Q. Wang, Y. Luo, H. Aziz, "Evidence of intermolecular species formation with electrical aging in anthracene-based blue organic light-emitting devices", *J. Appl. Phys.* **107**, 084506 (2010).
- ⁸⁶ H. Bassler, "Localized states and electronic transport in single component organic solids with diagonal disorder", *Phys. Stat. Sol. B* **107**, 9 (1981).
- ⁸⁷ J.-R. Gong, L.-J. Wang, S.-B. Lei, C.-L. Bai, X.-H. Zhang, S.-T. Lee, "Direct evidence of molecular aggregation and degradation mechanism of organic light-emitting diodes under joule heating: an STM and photoluminescence study", *J. Phys. Chem.* **109**, 1675-1682 (2005).
- ⁸⁸ S. Yang, M. Jiang, "White light generation combining emissions from exciplex, excimer and electromer in TAPC-based organic light-emitting diodes", *Chem. Phys. Lett.* **484**, 54-58 (2009).
- ⁸⁹ H. Kanno, R. J. Holmes, Y. Sun, S. Kena-Cohen, S. R. Forrest, "White stacked electrophosphorescent organic light - emitting devices employing MoO₃ as a charge - generation layer", *Adv. Mater.* **18**, 339-342 (2006).
- ⁹⁰ S. H. Kim, J. Jang, J. Y. Lee, "Relationship between host energy levels and device performances of phosphorescent organic light-emitting diodes with triplet mixed host emitting structure", *Appl. Phys. Lett.* **91**, 083511 (2007).
- ⁹¹ X. Yang, H. Huang, B. Pan, M. P. Aldred, S. Zhuang, L. Wang, J. Chen, D. Ma, "Modified 4, 4' , 4 " -Tri (N-carbazolyl) triphenylamine as a versatile bipolar host for highly efficient blue, orange, and white organic light-emitting diodes", *J. Phys. Chem. C* **116**, 15041-15047 (2012).
- ⁹² M.-H. Tsai, Y.-H. Hong, C.-H. Chang, H.-C. Su, C.-C. Wu, A. Matoliukstyte, J. Simokaitiene, S. Grigalevicius, J. V. Grazulevicius, C.-P. Hsu, "3-(9-Carbazolyl) carbazoles and 3, 6-di (9-carbazolyl) carbazoles as effective host materials for efficient blue organic electrophosphorescence", *Adv. Mater.* **19**, 862-866 (2007).
- ⁹³ H.-C. Yeh, H.-F. Meng b, H.-W. Lin, T.-C. Chao, M.-R. Tseng, H.-W. Zan, "All-small-molecule efficient white organic light-emitting diodes by multi-layer blade coating", *Org. Electron.* **13**, 914-918 (2012).
- ⁹⁴ T. Saragi, T. Fuhrmann-Lieker, J. Salbeck, "Comparison of charge - carrier transport in thin films of spiro - linked compounds and their corresponding parent compounds", *Adv. Funct. Mater.* **16**, 966-974 (2006).
- ⁹⁵ T. Spehr, R. Pudzich, T. Fuhrmann, J. Salbeck, "Highly efficient light emitters based on the spiro concept", *Org. Electron.* **4**, 61-69 (2003).
- ⁹⁶ Y.-C. Tsai, J.-H. Jou, "Long-lifetime, high-efficiency white organic light-emitting diodes with mixed host composing double emission layers", *Appl. Phys. Lett.* **89**, 243521 (2006).
- ⁹⁷ J. Y. Shen, C. Y. Lee, T.-H. Huang, J. T. Lin, Y.-T. Tao, C.-H. Chien, C. Tsai, "High-T_g blue emitting materials for electroluminescent devices", *J. Mater. Chem.* **15**, 2455-2463 (2005).

-
- ⁹⁸ J. Huang, T. Watanabe, K. Ueno, Y. Yang, “Highly efficient red-emission polymer phosphorescent light-emitting diodes based on two novel tris(1-phenylisoquinolinato-C2,N)iridium(III) derivatives”, *Adv. Mater.* **19**, 739-743 (2007).
- ⁹⁹ Y. Luo, H. Aziz, “Correlation between triplet–triplet annihilation and electroluminescence efficiency in doped fluorescent organic light-emitting devices”, *Adv. Funct. Mater.* **20**, 1285–1293 (2010).
- ¹⁰⁰ Q. Wang, H. Aziz, “Detecting luminescence from triplet states of organic semiconductors at room temperatures using delayed electroluminescence spectroscopy”, *Appl. Phys. Lett.* **105**, 053304 (2014).
- ¹⁰¹ J. A. Barltrop, J. D. Coyle, Principles of Photochemistry, John Wiley & Sons, New York City, NY, USA 1975.
- ¹⁰² P. J. Hay, “Theoretical studies of the ground and excited electronic states in cyclometalated phenylpyridine Ir(III) complexes using density functional theory”, *J. Phys. Chem. A* **106**, 1634-1641 (2002).
- ¹⁰³ H. Wu, J. Zou, F. Liu, L. Wang, A. Mikhailovsky, G. C. Bazan, W. Yang, Yong Cao, “Efficient single active layer electrophosphorescent white polymer light - emitting diodes”, *Adv. Mater.* **20**, 696–702 (2008).
- ¹⁰⁴ S. Reineke, F. Lindner, G. Schwartz, N. Seidler, K. Walzer, B. Lussem, K. Leo, “White organic light-emitting diodes with fluorescent tube efficiency”, *Nature* **459**, 234-238 (2009).